Technical Physics Letters, Vol. 28, No. 4, 2002, pp. 261–262. Translated from Pis'ma v Zhurnal Tekhnicheskoĭ Fiziki, Vol. 28, No. 7, 2002, pp. 1–5.

Kinematics of Failure Waves in Glasses

A. A. Bogach, G. I. Kanel', and S. V. Razorenov

Institute for Problems in Chemical Physics, Russian Academy of Sciences, Chernogolovka, Moscow oblast, Russia
e-mail: kanel@icp.ac.ru

Received November 16, 2001

Abstract—A new method for observation of the failure waves in glasses is proposed which allows this phenomenon to be reliably and reproducibly monitored, the failure wave propagation velocity to be measured, and an increase in the longitudinal stress to be determined. Using this method, the stresses produced by an elastic shock compression pulse propagating from the entrance of a stack of glass plates to the exit from this stack were experimentally measured. The compression wave exhibits splitting at each interface between adjacent glass plates in the stack, which leads to the formation of transmitted and reflected failure waves and is accompanied by decreasing stress in the leading elastic wave. © *2002 MAIK "Nauka/Interperiodica"*.

As is known, the shock compression of glasses may give rise to a failure wave in the elastic deformation region [1–3]. The failure wave represents a network of cracks initiated at the surface, which propagate at a subsonic velocity inward the glass. A special feature of this process in glasses, distinguishing it from that in other solids, is the formation of numerous nucleating microcracks on the surface for a virtually defectless volume structure. Propagation of the failure wave is accompanied by a decrease in the deviator stresses and by the loss of tensile strength. For generating a failure wave, it is necessary that the acting stress would exceed a certain threshold: as the acting stress drops below this level, the failure wave stops. The kinematic laws of the failure wave propagation are still insufficiently studied. In particular, the available experimental data do not reveal variations in the longitudinal stresses in the wave. Thus, it is even unclear whether such waves can be described by the conventional equations of the compressible continuum mechanics.

Below we present some preliminary results of experiments with soda-lime silica glass samples comprising stacked glass plates. The glass density is 2.45 g/cm^3 and the longitudinal sound velocity in this material is 5.58 km/s. The glass exhibited no clearly manifested dynamic elastic limit: the transition to inelastic shock compression proceeded for stresses above 6–8 GPa [3]. In order to provide for reproducible fracture initiation conditions, the glass plates were ground with a SiC powder (particle size, 40 μm). The shock compression pulses were generated by impact with a 7-mm-thick aluminum plate accelerated to a velocity of 1.15 km/s with the aid of an explosion device.The shock wave was introduced into the glass sample through a 5.5-mm-thick copper base plate; it traveled through the sample and reflected from a copper plate of the same thickness. The profiles of compressive stresses were monitored with the aid of manganin pressure gauges [1] mounted at the entrance to and exit from the sample. The pressure gauges were insulated with 50- to 100-μm-thick Teflon films.

Figure 1 shows the results of two experiments with the samples comprising either four stacked glass plates (each with a thickness of 1.21 ± 0.06 mm) or two thicker plates (2.52 mm). Figure 2 shows the proposed scheme of wave interactions. The junctions between ground plates, representing essentially porous interfacial layers, generate reflected pulses of unloading. These pulses propagate backward and reach the first gauge, producing short negative spikes in the wave profile at the time instants corresponding to points *2* and *2'* in Fig. 2. The measured time interval between these points corresponds with a good precision to the periods

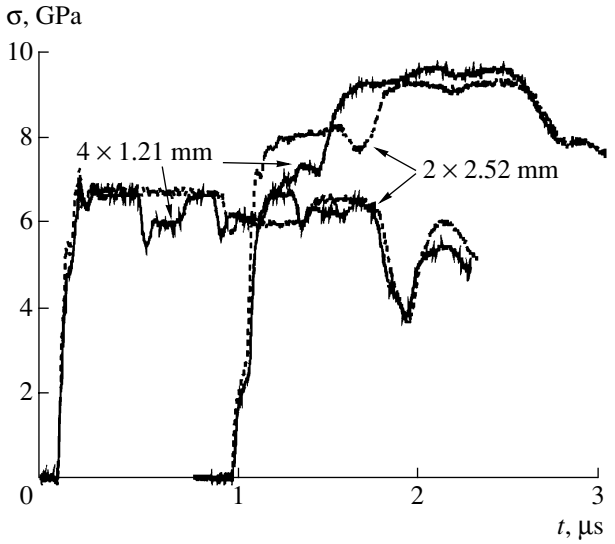

Fig. 1. Compression wave profiles measured in the samples comprising stacked glass plates with a thickness of 1.21 and 2.52 mm.

1063-7850/02/2804-0261$22.00 © 2002 MAIK "Nauka/Interperiodica"

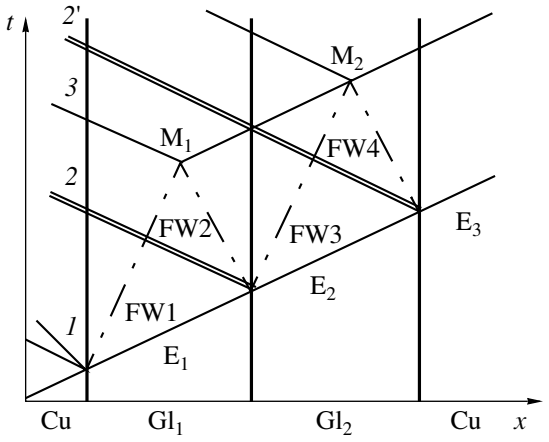

Fig. 2. A model diagram of wave interactions in the space–time coordinates: Gl_1 and Gl_2 are adjacent plates in the stack; E_1, E_2, and E_3 are points on the trajectory of a compressive elastic wave front; FW1, FW2, and FW3 are the failure wave trajectories.

of elastic wave circulating in the glass plates of the given thickness.

As can be seen from the experimental wave profiles, the compressive stress returns to a level determined by the initial impact conditions in a stepwise manner. The time interval between steps is proportional to the plate thickness, which suggests that this feature is related to the formation of two compression waves propagating one behind another at various velocities. Since the maximum stresses correspond to the region of elastic deformation, the second wave probably represents the failure wave. Taking into account that the failure wave cannot repeatedly pass through the same layer of a material, the second step in the reflected wave (point *3* in Fig. 2) corresponds to the time instant when the gauge detects the compression wave formed as a result of the interaction between two opposite failure waves at points M_1 and M_2 (Fig. 2). Assuming that the velocities of all waves (except for the failure wave) are equal to the longitudinal sound velocity, analyzing the space–time (wave interaction) diagram, and using the measured time intervals, the failure wave velocity in the first (counted in the direction of compression) plates of stacks was estimated at 1.56 km/s, which corresponds to a limiting velocity of crack propagation in glasses.

The pressure gauges arranged at the exit from the sample stack monitor clearly pronounced stepwise compression waves. The magnitude of the compressive stress behind the first wave front decreases with increasing number of plates (and, hence of interfaces on which the fracture is initiated) in the stack. The interval between waves increases with the plate thickness, whereas this interval would be unchanged for an elastic-plastic compression wave (provided equal thickness of the samples). On the other hand, there is no strict proportionality between the thickness of plates in the stack and the time interval between compression waves. A quantitative analysis of the wave profiles monitored by exit gauges is hindered by the fact that, for the shock wave propagating in the glass and reflected from the copper plate, the level of compressive stresses falls outside the range of elastic deformation.

Based on the experimental data obtained, the process of shock compression can be generally outlined as follows. The elastic compressive wave propagating in the sample initiates failure waves on the interfaces between glass plates. As a result, each interface produces splitting of the compression wave, which is accompanied by decreasing stress in the leading elastic wave. The stress increment in the failure wave is determined by a constant propagation velocity and by the degree of additional longitudinal fracture-induced compression. It is important to note that the failure wave velocity is determined by the crack propagation velocity, which is not immediately related to compressibility of the material. Our experimental results confirm that the failure wave is essentially a compression wave and, hence, can be described in terms of the conventional equations of the mechanics of compressible media.

At a sufficiently large number of plates in the stack, the stress in the leading elastic wave front must gradually decrease to a fracture initiation threshold. We may expect that, on approaching this stress level, the leading wave generates failure waves with decreasing velocity and eventually ceases to initiate the fracture. As a result, a wave configuration is formed that is typical of the shock compression of polycrystalline brittle materials: there is a leading elastic wave, the amplitude of which is determined by the fracture threshold, and the inelastic compression wave inducing fracture and compression of the material. The rise time of the second wave must correspond to the time of fracture propagation through individual plates, while the failure wave propagation velocity is determined by the volume compressibility of the solid. Thus, the proposed method opens new possibilities in studying the mechanisms of fracture of rocks, ceramics, and other polycrystalline brittle materials under compression conditions.

Acknowledgments. This study was supported by the Russian Foundation for Basic Research, project no. 01-01-00436.

REFERENCES

1. G. I. Kanel', S. V. Razorenov, A. V. Utkin, and V. E. Fortov, *Shock-Wave Phenomena in Condensed Media* (Yanus-K, Moscow, 1996).
2. G. I. Kanel', S. V. Razorenov, A. V. Utkin, *et al.*, High Press. Res. **16**, 27 (1998).
3. N. S. Brar, in *Shock Compression of Condensed Matter-1999*, Ed. by M. D. Furnish *et al.*; AIP Conf. Proc. **505**, 601 (2000).

Translated by P. Pozdeev

Technical Physics Letters, Vol. 28, No. 4, 2002, pp. 263–265. Translated from Pis'ma v Zhurnal Tekhnicheskoĭ Fiziki, Vol. 28, No. 7, 2002, pp. 6–11.

Effect of Mesoscopic Semiconductor Perturbations on the Electromagnetic Field Distribution in Near-Field Optical Microscopy

A. B. Evlyukhin

Vladimir State University, Vladimir, 600000 Russia

e-mail: evl@laser-2.vpti.vladimir.ru

Received September 28, 2001

Abstract—The effect of mesoscopic semiconductor perturbations in the volume of a dielectric sample on the electromagnetic field intensity distribution was theoretically studied for a scanning near-field optical microscope operating in the collecting mode for the surface structure investigation. A system of integral equations is constructed which takes into account for the first time the possibility that inhomogeneities are present simultaneously on the surface and in the bulk of the sample. It is shown that the near-field distortions introduced by the above perturbations significantly depend both on the location of a perturbation and on the properties of free charge carriers in this region. This effect must always be taken into account in near-field optical microscopy. © *2002 MAIK "Nauka/Interperiodica".*

The growing interest in micro- and nanotechnologies implies the need for developing adequate methods for the investigation of processes on the corresponding temporal and spatial scales. A new type of instruments providing for the possibility of studying the properties of individual mesoscopic objects is offered by the scanning near-field optical microscope (SNOM). To date, a rather large number of publications were devoted to near-field problems and, in particular, to near-field microscopy (see, e.g., reviews [1–3]). However, a number of basic problems are still not solved, including the task of determining the resolving power, the mechanisms of interactions between mesoscopic objects, the influence of random perturbations, etc.

The purpose of this study was to solve, at least partly, some of these problems. The main task was to elucidate the effects of bulk mesoscopic perturbations (with a characteristic size on the order of or smaller than the probing radiation wavelength) on the process of investigation of the sample surface structure. The calculations were performed within the framework of macroscopic electrodynamics with neglect of the spatial dispersion, therefore, it was assumed that the local fields vary negligibly over the longitudinal and transverse mean free path lengths of the charge carriers.

The paper essentially addresses the following physical model. A monochromatic light wave is incident from glass onto an ideal plane glass–air interface (the dielectric constants of glass and air are ε_1 and ε_2, respectively) under the condition of total internal reflection. As a result, a local electromagnetic field is generated at the interface, the intensity of which decays exponentially with distance from the glass surface. Relationships between the amplitudes of the incident, reflected, and refracted waves are determined by the Fresnel formulas. On both sides in the immediate vicinity of the interface (at distances much smaller than the light wavelength), there are nanoscopic bounded regions filled with a medium possessing a permittivity differing from that of both air and glass. The task is to calculate the resulting electric field strength (influenced by the nanoscopic objects) in the near-field zone on the air side (i.e., in the SNOM observation plane).

Let us formulate a mathematical model for the above problem. For a system comprising a homogeneous space and local mesoscopic objects, the problem of electromagnetic wave diffraction reduces to solving the following integral equation (all media are assumed to be nonmagnetic and the time dependence is described by the term $\exp(-i\omega t)$) [4]:

$$\mathbf{E}(\mathbf{r}) = \mathbf{E}_0(\mathbf{r}) + k_0^2 \int_V \hat{G}_0(\mathbf{r}, \mathbf{r}')(\varepsilon(\mathbf{r}') - \varepsilon)\mathbf{E}(\mathbf{r}')d\mathbf{r}'. \quad (1)$$

Here, $\mathbf{E}_0$ is the electric field in the homogeneous space corresponding to the region $V = V_1 + V_2$ being filled with a homogeneous medium possessing the permittivity ε; k_0 is the wavenumber in vacuum; and $\hat{G}_0$ is the basic solution of the stationary vector wave equation for a homogeneous space with a permittivity ε:

$$\hat{G}_0(\mathbf{r}, \mathbf{r}') = \left(\hat{1} + \frac{\nabla \cdot \nabla}{k^2}\right)\frac{\exp(ik|\mathbf{r} - \mathbf{r}'|)}{4\pi|\mathbf{r} - \mathbf{r}'|}, \quad (2)$$

where $k^2 = k_0^2\varepsilon$. If the vector $\mathbf{r}'$ belongs to region V, we obtain an integral equation for determining the compo-

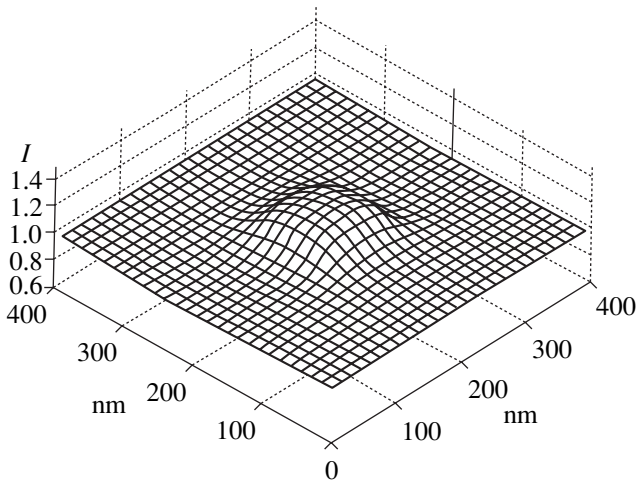

Fig. 1. A three-dimensional plot of normalized electric field intensity in the plane of observation for a physical system described in the text, with an object occurring at a depth of 15 nm below the surface. The calculation was performed for $\varepsilon_s = 2.25$ and $\varepsilon_p = 1$ (TM-polarized incident light).

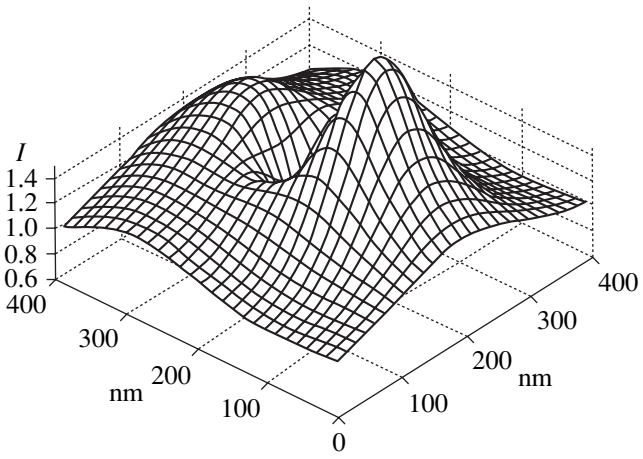

Fig. 2. A three-dimensional plot of normalized electric field intensity in the plane of observation for a physical system described in the text, with an object occurring at a depth of 15 nm below the surface. The calculation was performed for $\varepsilon_s = 2.25$ and ε_p determined for a Maxwell distribution with a free charge carrier concentration of 20×10^{17} cm^{-3} (TM-polarized incident light).

nents of **E**. Upon solving this equation, we can (in principle) determine the field strength at any point of the space.

For the physical system under consideration, the integral equation is of the same structure as (1), but the quantities have a somewhat different meaning. In particular, the dyadic Green function $\hat{G}(\mathbf{r}, \mathbf{r}')$ takes into account the glass–air interface. For constructing this function, we employ the method of mirror image, which is widely used for solving problems not involving retardation phenomena [5]. Assuming that the characteristic size of the domain of calculations is much smaller than the wavelength of the incident light, we can use this approximation for constructing the required Green's function. Within the framework of this approximation, the dyadic Green's function may acquire different forms, depending on the radius-vector position relative to the interface.

The integral equations describing the electric field in various regions of the space are as follows:

$$\mathbf{E}(\mathbf{r}) = \mathbf{E}_i(\mathbf{r}) + \mathbf{E}_r(\mathbf{r}) + \int_{V_p} \hat{G}_{11}(\mathbf{r}, \mathbf{r}')(\varepsilon_p - \varepsilon_1)E(\mathbf{r}')d\mathbf{r}' + \int_{V_s} \hat{G}_{12}(\mathbf{r}, \mathbf{r}')(\varepsilon_s - \varepsilon_2)\mathbf{E}(\mathbf{r}')d\mathbf{r}' \quad (3)$$

for $\mathbf{r} \in$ [space on the side of medium with ε_1] and

$$\mathbf{E}(\mathbf{r}) = \mathbf{E}_t(\mathbf{r}) + \int_{V_s} \hat{G}_{22}(\mathbf{r}, \mathbf{r}')(\varepsilon_s - \varepsilon_2)\mathbf{E}(\mathbf{r}')d\mathbf{r}' + \int_{V_p} \hat{G}_{21}(\mathbf{r}, \mathbf{r}')(\varepsilon_p - \varepsilon_1)E(\mathbf{r}')d\mathbf{r}' \quad (4)$$

for $\mathbf{r} \in$ [space on the side of medium with ε_2]. Here, V_s and V_p are the volumes of real local regions with dielectric permittivities ε_s and ε_p, situated above and below the surface, respectively (the subscripts of Green's functions correspond to the indices of permittivity in the semi-space regions in which **r** and **r**' occur); $\mathbf{E}_i$, $\mathbf{E}_r$, and $\mathbf{E}_t$ are the incident, reflected, and transmitted waves, respectively.

The above system of integral equations can be numerically solved as described in [6]. We have calculated the electric field intensities in the plane parallel to the interface (observation plane, situated on the air side at a distance of 70 nm from the interface) in the presence of rectangular local regions with dimensions of $100 \times 100 \times 50$ nm. These local regions are situated both on the surface (with total internal reflection) and under this surface (light wavelength, 620 nm). The objects possessed various permittivities. Inhomogeneities situated on the surface were considered as dielectric protrusions, while perturbations under the surface were characterized by the permittivities calculated using a kinetic equation. This approach allowed us to take into account various mechanisms of scattering of the charge carriers and various degrees of degeneracy of the symmetric part of their distribution functions.

The results of our calculations showed that information about the shape of the dielectric protrusion can be significantly distorted in the presence of the mesoscopic semiconductor region under the sample surface. The distortions depend both on the position and shape of the perturbation and on the internal properties of charge carriers in this object. As an example, Fig. 1 shows the results of calculations for the case when a

glass protrusion is present on the surface and an air bubble is situated below the interface. Figure 2 presents the results obtained for a semiconductor region possessing a complex permittivity situated under the glass protrusion. As can be seen from these examples, the pattern of the field intensity distribution significantly depends on the physical properties of local regions. Moreover, information about the shape of the dielectric protrusion can be fully distorted by inhomogeneities of a certain kind situated under the surface. Thus, the effect considered above should always be taken into account in applications of the near-field optical microscopy. A more detailed analysis of this problem will be published soon.

REFERENCES

1. D. Courjon and C. Bainier, Rep. Prog. Phys. **57**, 989 (1994).
2. C. Girard and A. Dereux, Rep. Prog. Phys. **59**, 657 (1996).
3. O. Keller, Phys. Rep. **268**, 85 (1996).
4. V. I. Dmitriev and E. V. Zakharov, *Integral Equations in Boundary-Value Problems of Electrodynamics* (Mosk. Gos. Univ., Moscow, 1987), p. 251.
5. Z. Li, B. Gu, and G. Yang, Phys. Rev. B **55**, 10883 (1997).
6. Ch. Girard, A. Dereux, O. J. F. Martin, *et al.*, Phys. Rev. B **52**, 2889 (1995).

Translated by P. Pozdeev

Technical Physics Letters, Vol. 28, No. 4, 2002, pp. 266–269. Translated from Pis'ma v Zhurnal Tekhnicheskoĭ Fiziki, Vol. 28, No. 7, 2002, pp. 12–18.

On the Possibility of Regular Self-Induced Pulsations in Injection Laser Radiation

V. A. Yurevich

Institute of Applied Optics, National Academy of Sciences of Belarus, Mogilev, Belarus

e-mail: ipo@physics.belpak.mogilev.by

Received October 31, 2001

Abstract—The regime of generation of a regular series of relatively short pulses in a cw-pumped semiconductor laser was numerically modeled. This regime is developed as a result of a phase self-modulation of the light field in the presence of a thin active layer on the laser diode edge, provided that the layer exhibits absorption in the frequency region close to the lasing frequency. © *2002 MAIK "Nauka/Interperiodica".*

A large variety of both regular and stochastic self-modulation structures observed in the radiation of solid-state lasers is attributed to the phase self-modulation (PSM) effect on the process of induced emission in laser cavities [1]. In the case of semiconductor injection lasers, an especially effective factor is the nonlinear refraction in the active layer, acquiring a "giant" character in the frequency region of the exciton resonance or interband absorption [2]. The consequences of PSM, related to the noninertial phase deviations with respect to the carrier concentration, were studied in sufficient detail in the case of systems with external feedback [3–5]. The time pattern of emission of an injection laser may exhibit qualitative variations depending on the feedback parameters and the pump current, even in the case when the external resonator contains only a reflector, rather than special dispersion or modulation devices.

It would be of interest to consider a dynamic model of the injection laser with a feedback system containing additional thin layers exhibiting active absorption at frequencies close to the lasing frequency. As is known, the presence of a thin, resonant, polarizable film with a thickness smaller than the radiation wavelength may strongly affect the optical properties of the interface [6–9]. The optical transmission of a thin resonant layer is sensitive to both intensity and phase of the external light field. Under these conditions, the feedback efficiency is related to the intrinsic nonlinearity of refraction of the active layer in the laser diode and the related frequency deviations of the generated mode field. Thin-film planar elements parallel to the exit faces of laser diodes may serve as nonlinear *Q*-modulators of a special kind. Therefore, it would be quite expedient to model the nontrivial dynamics of an injection laser emission, with an allowance for the self-modulation effects in the systems employing such elements.

Let us consider a nonlinear film deposited directly onto a laser diode edge. Under the resonance interaction conditions, the absorption in the layer depends on the differential population of levels involved in the transition, which is saturated due to a power supplied via the external field. The nonlinear refraction of the active medium of a laser diode or a planar layer in the frequency region near the optical resonance can be considered within the framework of the so-called two-level scheme. Using this assumption, we may relatively simply take into account a contribution to the total polarizability from the transitions adjacent to the main (resonance). The corresponding deviations of the refractive index are directly related to a resonance change in the aforementioned differential population, and can be observed in semiconductors and some dielectric active materials.

Using the approximation of noncoherent interaction between the field and atoms in a superthin film and following the conclusions derived in [10], the dynamics of optical transmission $T(t) = |E|^2/E_0^2$ of the surface film can be described by the following expression:

$$T(t) = \frac{\dfrac{4\eta}{(1+\eta)^2}}{\left\{\left(1+\dfrac{\kappa n}{1+\Delta\omega^2\tau_2^2}\right)^2+\kappa^2\left[\dfrac{n\Delta\omega\tau_2}{1+\Delta\omega^2\tau_2^2}+\beta_c(n-n_0)\right]^2\right\}}, \quad (1)$$

$$\frac{dn}{dt} = \frac{1}{\tau_c}\left(n_0 - n - \frac{\sigma_c n|E|^2}{1+\Delta\omega^2\tau_2^2}\right),$$

where E and E_0 are the fields of light waves incident onto the film from the external medium (with a refractive index η) and acting upon atoms in the film; n is the variable of the population difference probability; n_0 is the initial differential population ($0 < n_0 \le 1$); κ is the coefficient of absorption at the resonance frequency; σ_c is the transition cross section (i.e., the parameter of

nonlinear absorption); τ_c and τ_2 are the times of longitudinal and transverse relation of active atoms in the layer; $\Delta\omega$ is the field frequency detuning from the resonance; β_c is the nonlinear refraction parameter (for semiconductors, this quantity is usually assumed to be nonzero even for $\Delta\omega = 0$; see, e.g. [3]). In Eq. (1), the term proportional to variation of the differential population $n - n_0$ in the dispersion component of $T(t)$ reflects the contribution due to the phase shift caused by nonlinear refraction in the film.

In the simplest model of injection laser, the energy balance between radiation and pumped excited medium can be described by usual kinetic equations for the variables of intensity and population inversion (carrier concentration in the laser diode) averaged over the active layer thickness [10]. An allowance for the special physical situation related to the presence of thin layers with saturated absorption and nonlinear refraction on the laser diode edges leads to some modification of this model. The expression for the variable coefficient of radiative losses (averaged over the laser diode length) will include information about a change of the planar layer transmission depending on the generation power. Then, the laser radiation intensity is considered as the external field intensity in Eq. (1). A change in the film transmission under the action of this field must be also due to variation of the lasing frequency in a nonlinear-refractive medium of the laser diode. The dispersive variation of transmission in Eq. (1) is assumed to depend on the dimensionless variable of detuning $\Delta = \left(\delta\omega + \frac{d\varphi}{dt}\right)\tau_2$, where $\delta\omega$ is the distance (on the frequency scale) between resonances of the laser diode medium and the planar layer medium; the effective detuning Δ is normalized to the value of reciprocal optical resonance halfwidth for active atoms in the film. The phase derivative in the generation field representation $E_g(t) = E_0\exp(i\varphi)$ describes nonlinear frequency displacement.

In the case of constant pumping, the system of modified kinetic equations is as follows:

$$\frac{dI}{dt} = \frac{1}{\tau}\left[y - \frac{\ln\gamma(n)}{\ln\gamma_0}\right]I, \quad \frac{dy}{dt} = \frac{1}{\tau_1}(\alpha - y - yI),$$

$$\frac{dn}{dt} = \frac{1}{\tau_c}\left[n_0 - n - \frac{\sigma n I}{\gamma(n)(1+\Delta^2)}\right],$$

$$\Delta = \left[\delta\omega + \frac{\beta}{\tau}(y-1)\right]\tau_2, \qquad (2)$$

$$\gamma(n) = \left(1 + \frac{\kappa n}{1+\Delta^2}\right)^2 + \kappa^2\left[\frac{n\Delta}{1+\Delta^2} + \beta_c(n - n_0)\right]^2,$$

$$\gamma_0 = \gamma(n_0),$$

where $I = \sigma_d E_0^2$ is the normalized laser field intensity (σ_d is the working transition cross section in the laser diode medium), y is the probability characteristic of the carrier concentration in the active layer of the laser diode (relative to the threshold level), and $\ln\gamma(n)$ is the index of lasing power losses in the absorbing planar layer; $\tau = \frac{\eta l}{c}\left(\ln\frac{\gamma_0}{r}\right)^{-1}$ is the photon lifetime in the resonator, l is the length of the active layer, r is the energy reflection coefficient at the diode edge; α is the pumping current parameter, β is the nonlinear refraction parameter, and τ_1 is the spontaneous recombination time in the laser diode medium; and $\sigma = \sigma_c/\sigma_d$ is the ratio of transition cross sections.

The self-modulation effect described by Eqs. (2) is determined by a positive feedback existing in the system with planar layer on the laser diode edge. The model also takes into account that the absorption in the layer decreases with increasing generation power. In addition to a change in the absorption due to saturation, which is traditionally considered in the theory of laser dynamics, Eqs. (2) can be also used to consider the lasing process affected by the deviations in the planar layer absorption related to the frequency displacement, that is, the PSM effect.

The system of Eqs. (2) was numerically integrated by the Runge–Kutta method within the framework of the Cauchy problem with the initial conditions corresponding to the lasing threshold. Thus, it was assumed that $y(t = 0) = 1$, $n(t = 0) = n_0 = 1$; the initial intensity was assumed to be extremely small (but nonzero), $I(t = 0) \approx 10^{-5}\ldots10^{-4}$ ($I(t = 0) \ll \alpha - 1$), so that the calculations corresponded to the scheme of small signal amplification. The solutions for $I(t)$ were virtually independent of the $I(t = 0)$ value. On the whole, the set of the calculation coefficients for Eqs. (2), including the nonlinear refraction parameters for both media corresponded to characteristics of the GaAs-based materials employed in optics and laser physics.

In practice, of special interest are the self-modulation regimes corresponding to the generation of a series of contrast nondamping pulses. Indeed, the solutions of Eqs. (2) for $I(t)$, obtained by numerical modeling with a set of parameters corresponding to an injection laser, predict such regimes. Figure 1 shows typical examples of the numerically modeled generation process for a sufficiently wide range of parameters in Eqs. (2). As can be seen, the calculated curves describing the time pattern of generation with a regular structure are qualitatively similar. The period of amplitude buildup and an increase in the off-duty ratio of the field power outbursts corresponds to the stage of transition to a periodic regime in the calculated pulse train. This is followed by stabilization of the amplitude and shape of pulsations. In the plane of variables $[I(t), T(t)]$, this transition corresponds to attaining a limiting cycle on the projections of phase trajectories (Figs. 1a"–1d"). The pulse characteristics—including amplitude, duration,

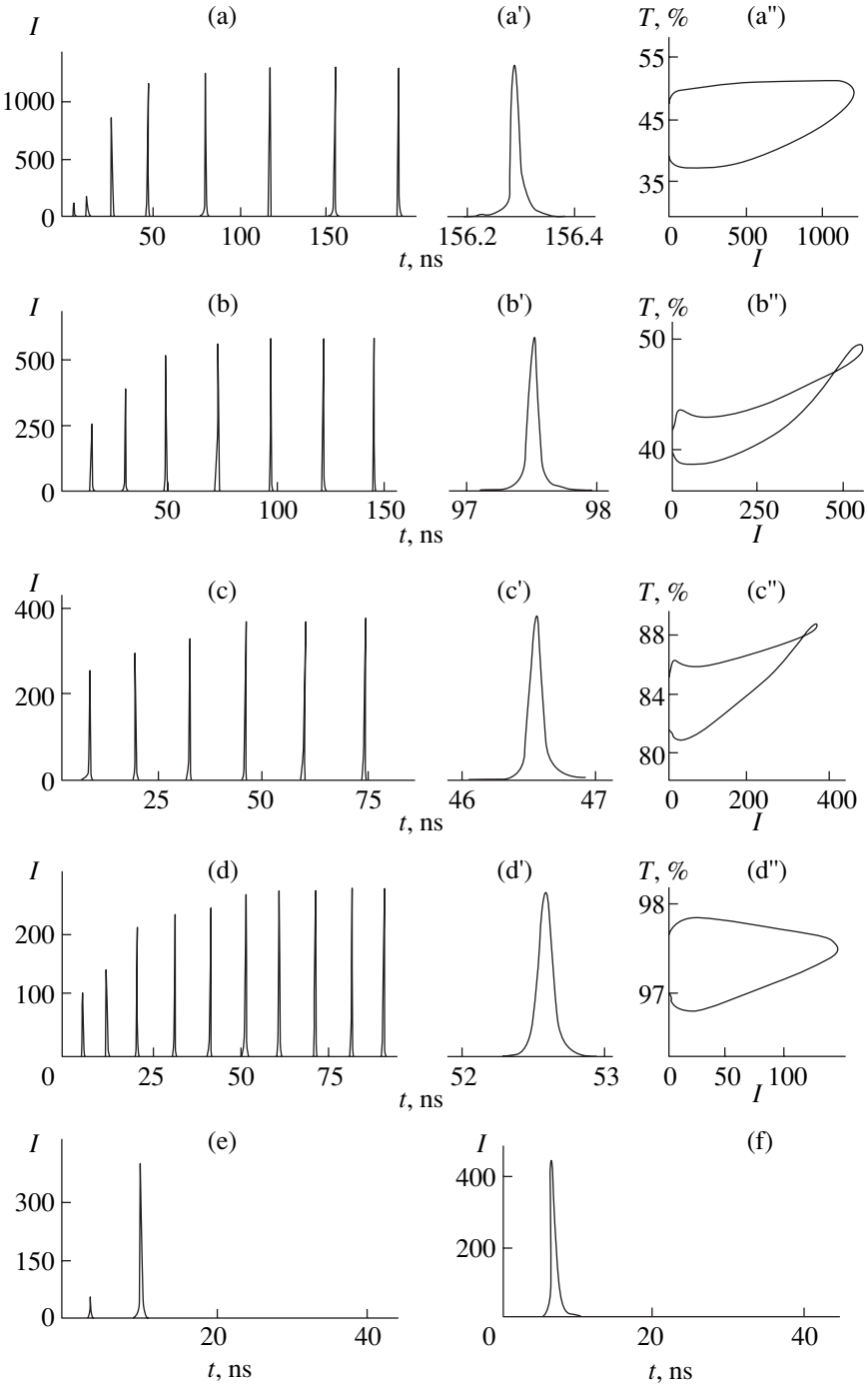

Fig. 1. The calculated time patterns: (a–f) the structure of radiation intensity variation in the injection laser; (a'–d') pulse shapes; (a"–d") projections of phase trajectories ($T_{\%} = 100/\gamma(n)$); $\alpha = 1.4$ (a, d), 1.33 (b, c, e, f); $\kappa = 1.85$ (a), 2,5 (b, e), 0.9 (c, f), 0.3 (d); $\delta\omega\tau_2 = 1.0$ (a), 2.0 (b, e), 3.0 (c, f), 4.0 (d); $\beta = 2.5$ (a–d), 0 (e, f); $\beta_c = 0.5$ (a–d), 0 (e, f); $\sigma = 2.0$, $r = 0.32$, $\eta = 3.6$, $\tau_1 = 5.0 \times 10^{-9}$ s, $\tau_c = 1.0 \times 10^{-9}$ s, $l = 3 \times 10^{-4}$ m.

repetition period (in this example, the time scale corresponds to subnanosecond and nanosecond intervals), off-duty ratio, and contrast—are determined by the ratio of rate parameters (the pumping current level, population relaxation times in the active layer and planar film, and induced transition probability). Therefore, a regular structure of the injection laser emission described by Eqs. (2), arising from oscillations of the feedback level, possesses a relaxation character.

The results of calculations showed that the probability of a transition to periodic self-modulation pulsation is especially critical with respect to the level of nonlin-

ear refraction in the active layer of the injection laser. If the corresponding equations in Eqs. (2) are equal to zero (i.e., the nonlinear refraction is ignored), no solutions corresponding to a regular time pattern variation can exist (see Figs. 1e and 1f). Accordingly, no limiting cycles are formed in this case on the phase plane of system (2). The appearance and stability of a regular time pattern in the injection laser radiation are determined to a considerable extent by the phase self-modulation effect. A high sensitivity of the thin film transmission with respect to the radiation phase is a decisive factor of stabilization of the periodic time pattern of the laser field. It should be also noted that calculations within the framework of model (2) predict the possibility of generation of a series of self-modulation pulses for the transmission varied within a relatively small interval (a few percent, see Figs. 1c and 1d). This regime is possible for a considerable mutual detuning $\delta\omega$ of absorption resonances in the planar layer and amplification in the lasing medium. For this reason, the effective level of absorption in the planar layer necessary for the transition to the required generation regime can be relatively low ($\sim 10^3$–10^4 cm^{-1}).

Acknowledgments. This study was supported by the Belarussian Foundation for Basic Research, project no. F99-346.

REFERENCES

1. N. B. Abraham, P. Mandel, and L. M. Narducci, Prog. Opt. **25**, 1 (1988).
2. P. G. Eliseev and Yu. M. Popov, Kvantovaya Élektron. (Moscow) **24** (12), 1067 (1997).
3. K. Pelermann, IEEE J. Sel. Top. Quantum Electron. **1** (2), 480 (1995).
4. V. A. Yurevich, Pis'ma Zh. Tekh. Fiz. **22** (19), 10 (1996) [Tech. Phys. Lett. **22**, 781 (1996)].
5. D. H. DeTienne, G. R. Gray, G. P. Agrawal, and D. Lenstra, IEEE J. Quantum Electron. **QE-33** (5), 838 (1997).
6. S. M. Zakharov, A. I. Maĭmistov, É. A. Manykin, *et al.*, Poverkhnost, No. 12, 60 (1989).
7. M. E. Grenshaw and C. M. Bowden, Phys. Rev. Lett. **69** (24), 3475 (1992).
8. V. A. Yurevich, Kvantovaya Élektron. (Moscow) **21** (10), 959 (1994).
9. C. V. Bowden and G. P. Agrawal, Phys. Rev. A **51** (5), 4132 (1995).
10. V. A. Yurevich, Zh. Prikl. Spektrosk. **66** (5), 661 (1999).

Translated by P. Pozdeev

Technical Physics Letters, Vol. 28, No. 4, 2002, pp. 270–271. Translated from Pis'ma v Zhurnal Tekhnicheskoĭ Fiziki, Vol. 28, No. 7, 2002, pp. 19–23.

The Absorption Spectra of Gallium Nitride Crystals Doped with Erbium Ions

V. V. Krivolapchuk, M. M. Mezdrogina, S. D. Raevskiĭ, A. P. Skvortsov, and Sh. A. Yusupova

Ioffe Physicotechnical Institute, Russian Academy of Sciences, St. Petersburg, 194021 Russia

e-mail: A.Skvortsov@pop.ioffe.rssi.ru

Received November 30, 2001

Abstract—We have measured the absorption spectra of Er^{3+} ions introduced by diffusion into bulk GaN crystals grown by vapor phase epitaxy in a chloride system. The wavelength interval of 518–527 nm corresponding to the region of the $^4I_{15/2} \longrightarrow {}^2H_{11/2}$ transition was studied in detail at 293, 77, and 2 K. At 2 K, the spectrum of this transition displays six lines, which correspond to the theoretically possible number of sublevels of the $^2H_{11/2}$ state of Er^{3+} ion occurring in a noncubic crystal field. The positions of levels in the $^2H_{11/2}$ multiplet correspond to 2.360, 2.361, 2.365, 2.369, 2.379, and 2.386 eV. Both the number and narrow width of lines observed at 2 K indicate that Er^{3+} ions predominantly occupy the same regular position in GaN crystals. Most probably, erbium ions occupy gallium sites in the crystal lattice. © *2002 MAIK "Nauka/Interperiodica".*

In recent years, extensive investigation was devoted to semiconductors doped with rare-earth ions (RE^{3+}) in connection with possible applications to light-emitting devices. The group of promising materials for lasers and LEDs operating in the visible and UV range includes gallium nitride (GaN). Of special interest is GaN doped with Er^{3+} ions, which is related to the fact that erbium luminescence (1.54 μm) falls within a spectral region corresponding to minimum losses of optical fibers most frequently employed in fiber optic communication lines. Until now, the spectra of electro-, cathodo-, and photoluminescence were only studied for crystalline and amorphous films of GaN doped with Er^{3+} ions. Below we present the results of investigation of the *f–f* absorption spectra of Er^{3+} in bulk GaN crystals.

The initial bulk (100- to 500-μm-thick) *n*-type GaN crystals were grown on (0001) sapphire substrates by vapor phase epitaxy in the chloride system. The dopant was introduced by diffusion from a metallic erbium film deposited in vacuum onto the GaN crystal surface. The diffusion annealing was performed for 60–120 min at 1000–1500°C in an NH_3 atmosphere, after which the GaN:Er^{3+} crystals were etched in an HNO_3–HCl acid mixture (1 : 3) in order to remove nondiffused erbium from the surface.

The optical absorption spectra of GaN:Er^{3+} samples were measured at 293, 77, and 2 K. The measurements were performed in the wavelength interval from 0.35 to 1.7 μm using a polarized light beam with $\mathbf{E} \perp C_6$, where C_6 is the hexagonal axis of the crystal. It was found that the region near 0.52 μm contains a group of lines related to the transitions from sublevels of the ground $^4I_{15/2}$ state to sublevels of the excited $^2H_{11/2}$ state, which are most intense in the absorption spectra of Er^{3+} ions in crystals. As the temperature was decreased from 293 to 2 K, the number of lines in the spectrum decreased, while intensity of the remaining lines increased. At 2 K, when the transitions take place only from the lowest sublevel of the ground sate, the spectrum of the $^4I_{15/2} \longrightarrow {}^2H_{11/2}$ transition displays six lines (Fig. 1). This number coincides with the theoretically possible number of sublevels of the $^2H_{11/2}$ state of Er^{3+} ion occurring in a noncubic crystal field (the point symmetry group of single crystal GaN is C_{6v}^4). An analysis of the spectra measured at 2 and 77 K allowed the energy positions of the lowest sublevels of the ground $^4I_{15/2}$

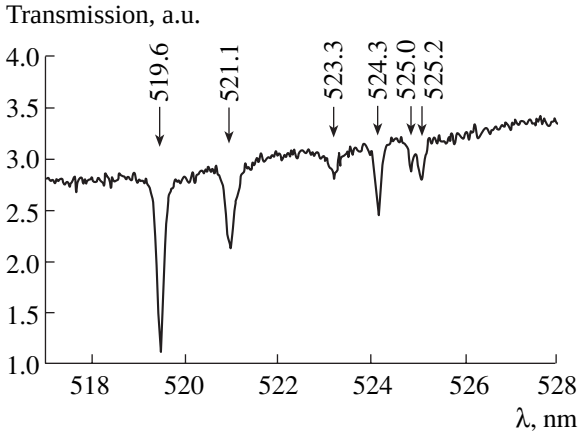

Fig. 1. The transmission spectrum of GaN:Er^{3+} in the region of the $^4I_{15/2} \longrightarrow {}^2H_{11/2}$ transition measured at 2 K.

1063-7850/02/2804-0270$22.00 © 2002 MAIK "Nauka/Interperiodica"

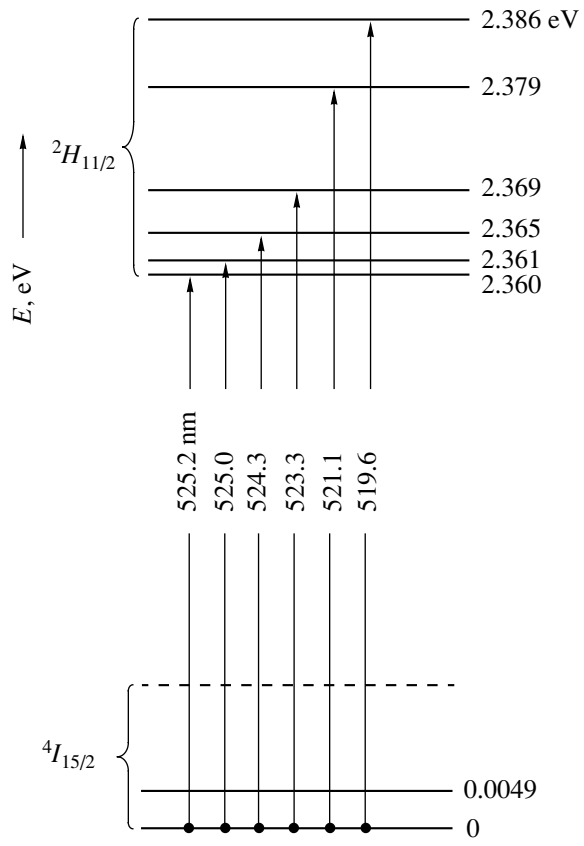

Fig. 2. The diagram of energy levels for the $^2H_{11/2}$ multiplet and the $^4I_{15/2} \longrightarrow {}^2H_{11/2}$ transitions in GaN:Er^{3+} at 2 K.

state and the excited $^2H_{11/2}$ state of Er^{3+} ions in GaN crystals to be determined (Fig. 2).

As is known, RE^{3+} ions possess a partly filled 4*f* subshell screened by the completely filled $5s^25p^6$ shells. The screening effect of the outer shells results in a weak interaction of the intraconfiguration transitions with the surrounding crystal lattice. For this reason, the spectrum of each particular RE^{3+} ion only slightly changes in various crystal matrices. The structure of levels of the $^2H_{11/2}$ multiplet found in the spectrum of our GaN:Er^{3+} samples is closest to that previously observed in Er_2O_3 crystals [1] and Y_2O_3:Er^{3+} crystals [2].

Judging by the number and small width (0.7 meV) of lines in the spectrum of the $^4I_{15/2} \longrightarrow {}^2H_{11/2}$ transition at 2 K (Fig. 1), we have reliable grounds to conclude that Er^{3+} ions predominantly occupy the same regular position (constituting the main erbium center) in the GaN crystal samples studied. Most probably, erbium ions displace gallium atoms from the crystal lattice sites. In addition to the main type of Er^{3+} centers, GaN crystals may also feature (in a significantly smaller amount) complexes composed of Er^{3+} ions, intrinsic crystal defects, and/or some uncontrolled impurities. This is evidenced by data on the selectively excited photoluminescence from GaN:Er^{3+} films [3], where the measurements revealed erbium centers of nine different types. It should be noted that the existence of several types of centers in doped crystals is rather a general phenomenon. For example, congruent $LiNbO_3$ crystals doped with Er^{3+} ions contain Er^{3+} centers of four types [4], while stoichiometric crystals of the same compound contain the centers of 11 types [5]. The existence of different erbium centers in these crystals is related to the ability of dopant ions to substitute for host atoms in various regular positions in the crystal lattice and to various mechanisms of compensation for the excess charge.

To our knowledge, the above results present the first observation of the absorption spectra of GaN:Er^{3+} crystals.

Acknowledgments. This study was partly supported by the Russian Foundation for Basic Research, project no. 99-02-18319.

REFERENCES

1. J. B. Gruber, J. R. Henderson, M. Muramoto, *et al.*, J. Chem. Phys. **45** (2), 477 (1966).
2. P. Kisliuk, W. F. Krupke, and J. B. Gruber, J. Chem. Phys. **40** (12), 3606 (1964).
3. S. Kim, S. J. Rhee, X. Li, *et al.*, J. Electron. Mater. **28** (3), 266 (1999).
4. K. Polgar and A. P. Skvortsov, Opt. Spektrosk. **58**, 229 (1985) [Opt. Spectrosc. **58**, 140 (1985)].
5. V. Dierolf and M. Koerdt, Phys. Rev. B **61** (12), 8043 (2000).

Translated by P. Pozdeev

Technical Physics Letters, Vol. 28, No. 4, 2002, pp. 272–274. Translated from Pis'ma v Zhurnal Tekhnicheskoĭ Fiziki, Vol. 28, No. 7, 2002, pp. 24–30.

Spatial and Spectral Characteristics of Two-Dimensional Photon-Fiber Crystals

L. A. Mel'nikov, Yu. P. Sinichkin, and Yu. S. Skibina

Saratov State University, Saratov, Russia

e-mail: SkibinaJS@yandex.ru

Received November 19, 2001

Abstract—The transmission spectra of two-dimensional photon-fiber crystals with various internal structures were studied. It is established that the spectra of transmitted and scattered radiation depend on the crystal orientation and the polarization of incident radiation. The spectra of radiation scattered at various angles from a two-dimensional periodic lattice were studied. The phenomenon of spectral filtration of the radiation transmitted through a photon-fiber crystal was discovered. © *2002 MAIK "Nauka/Interperiodica".*

Introduction. In recent years, a considerable effort has been devoted to the development of materials with controlled optical properties, which are capable of transmitting or, on the contrary, quenching light propagating in certain directions. One group of such materials is represented by the so-called photon crystals—structures with periodically varying dielectric permittivity, the period of which is comparable with the light wavelength [1].

A photon crystal can be made using a transparent dielectric, in which a certain number of ordered channels is created so that the light propagates in the medium containing regions possessing either a large (dielectric) or small (channels) index of refraction. This contrast of the refractive index plays the same role for photons, as does the periodic potential in a semiconductor crystal for electrons [2]. Indeed, a photon crystal possesses (in full analogy to semiconductors) allowed and forbidden bands (photon bands). Accordingly, the crystal blocks the light with a wavelength corresponding to the photon forbidden band and transmits without obstacles the light with any other wavelength [3].

The theory of two-dimensional photon crystals is still under investigation. However, it has been established that photon forbidden bands can exist in a glass–air structure [4]. Such a crystal can be manufactured by repeatedly drawing glass rods, but it would be difficult to obtain a structure with ideal packing. Real structures contain either stacking faults or a superlattice structure. However, we may expect that the main characteristics of such systems, related to the presence of a periodic structure, will be generally the same as in the ideal photon crystal.

Below we present the results of an experimental investigation of the transmission and scattering spectra of two-dimensional photon-fiber crystals fabricated by this technology.

Photon-fiber crystal fabrication. The photon-fiber crystal technology is based on the following procedures [5]. High-precision glass capillaries with a length of about 1 m are arranged in a bundle so as to obtain a hexagonal packing. Then the bundle of capillaries is passed through a furnace and subjected to drawing in a special device so as to obtain a hexagonal structure of smaller cross section (a reduced copy of the blank structure). These structures are again packed in a bundle, processed by drawing, and so on, repeating this procedure unless the structure with a preset step (air-channel period) is obtained. Upon replacing one capillary with a filled glass rod in the initial bundle and conducting the same technological process, we eventually obtain a hexagonal structure with a broken periodicity of the air channels. Using this technology, it is possible to fabricate photon-fiber crystals made of various glass compositions that possess various configurations (hexagonal, square, triangular, etc.), topologies, and defect structures. This method provides for the obtaining of high-precision nanostructures. Our samples were fabricated, using a four-stage drawing process, with a hexagonal configuration of packed capillaries. The capillary diameter varied from 0.2 to 0.8 μm.

The sample structure represented glass cylinders with a regular system of air channels aligned parallel to the axis. The regular system was assembled from elements in the form of regular hexagons, each containing several dozen of air channels. The total number of air channels in a two-dimensional photon crystal was determined as a product of the number of channels in the elementary hexagon by the number of such hexagons in the sample assembly.

The two-dimensional sample structure is presented on the inset in Fig. 1. The structures differed in the total number of air channels, spatial arrangement of the elements, and optical parameters of the two-dimensional

1063-7850/02/2804-0272$22.00

lattice [the period and the component ratio (air/dielectric) in the cross section].

Experimental procedure and results. The optical measurements were performed in the visible spectral range using a computer-controlled measuring complex based on an MDR-23 monochromator. The sample cross sections varied from 200 to 600 μm. Depending on this value, the radiation beam striking the monochromator slit was formed using one of the two possible schemes. In the first scheme (Fig. 2), the light beam transmitted through the sample structure was separated by a slit diaphragm placed immediately behind the sample. This arrangement was employed with the samples of relatively large cross section; the aperture was varied so as to correspond to the sample cross section. A disadvantage of this scheme is the impossibility of ensuring that only the radiation transmitted through the sample is incident on the monochromator slit.

In the second scheme, free of the above disadvantage, the image of the sample structure cross section was formed in the plane of the monochromator slit with the aid of a microobjective (magnification, ×10). The second scheme was selected for the following reasons. First, the size of the image formed in the plane of the monochromator slit was greater than the slit width used for the high-precision spectral measurements. The second (and most important) point was that the relative aperture of the objective was 0.2, which allowed rejection of the light beams transmitted through the sample so as to bypass the periodic photon crystal structure.

Using the second scheme of measurements, it was possible to ensure that only radiation transmitted through the periodic structure would strike the monochromator slit; the presence of color in the central part of the image was indicative of a coherent scattering of visible light from the sample structure. The second scheme was also employed for measuring the spectra of scattered radiation. In this case, the angle of incidence of a white light beam onto the sample was varied, while positions of the sample and the microobjective relative to the monochromator slit remained unchanged. The white light beam in all experiments was generated by a halogen lamp.

The transmission spectra were measured for the normal incidence of a differently polarized light beam onto the sample, which was rotated so as to expose either face or edge of the structure. In all cases (i.e., with different polarizations of light and orientations of the photon crystal), the transmission was significantly lower in a short-wavelength part of the visible spectral range. In this spectral interval, the incident light beam experienced coherent scattering leading to angular redistribution of the transmitted radiation. This effect accounts, in particular, for the formation of photon forbidden bands.

Obviously, the spectrum of radiation transmitted through the sample is influenced by refraction at the air–sample interface. As a result, a wave formed at this

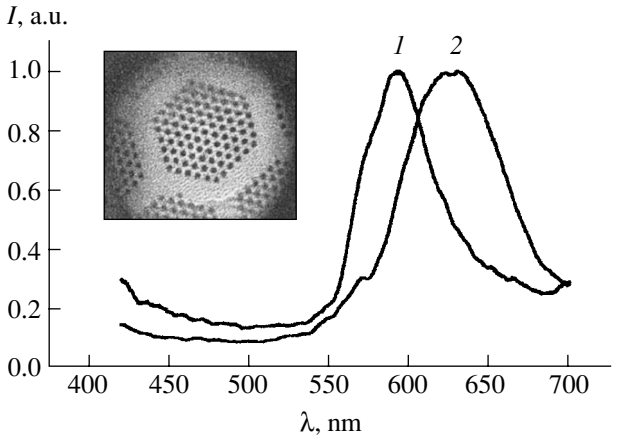

Fig. 1. The spectra of radiation scattered at various angles (*1*, 80°; *2*, 120°) for different orientations of the sample relative to the incident light beam. The inset shows a typical sample structure.

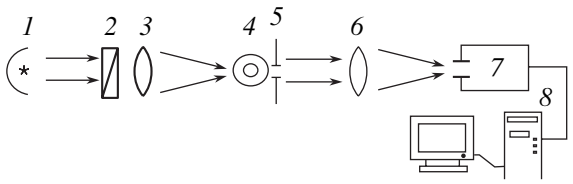

Fig. 2. Schematic diagram of the experimental setup: (*1*) halogen lamp; (*2*) polarizer; (*3*, *6*) lenses; (*4*) sample structure; (*5*) slit; (*7*) monochromator; (*8*) computer.

interface, rather than the plane incident wave, is propagating in the sample structure. Therefore, radiation transmitted through the sample contains beams propagating in various spatial directions. This may result in broadening of the photon forbidden band and in a partial transmission of light in this spectral interval.

At the same time, a relation between the structure period (all samples were characterized by a distance between adjacent air channels in the direction parallel to the structure face $a \sim 0.2$ μm) and the average wavelength λ of the forbidden band agrees with the calculated value: $a/\lambda \sim 0.4$.

The angular distribution of radiation transmitted through the sample exhibits a complicated character. The pattern depends on the sample orientation relative to the incident beam and on the polarization of the incident light. The main features of the angular distribution of radiation transmitted through the sample are considered below. Preliminary measurements of the light scattered at various angles were performed with a goniometer, one arm of which was used to illuminate the sample and another arm, to observe (via microscope) the color of the structure. These investigations revealed a complicated pattern of variation of the structure coloration, which gradually converted from one spectral range to another.

It should be noted that the first important result of our experiments was determining a criterion for selecting two-dimensional periodic structures possessing photon forbidden bands in the visible spectral range. It was established that a structure possessing such forbidden bands must exhibit a certain color when examined in a reflected white light. The samples exhibiting no such coloration in the reflected light possess a photon forbidden band in the infrared range.

When the light propagates in the sample at an angle relative to the plane of the periodic structure, the wavevector comprises two components. The component oriented along the structural elements introduces no changes into the sample transmission spectrum, whereas the component lying in the plane of the periodic structure is responsible for the formation of photon forbidden bands. An increase in the angle between the light beam propagation direction and the plane of the periodic structure is accompanied by a decrease in width of the photon forbidden bands of the photon crystal and eventually the band structure disappears. Measurements of the transmission spectra for an oblique incidence of light onto the sample structure showed that tilting the sample decreases the spectral interval corresponding to minimum transmission and shifts this interval toward shorter wavelengths.

On the background of this angular distribution, we observed the regions of bright intense coloration. The spectra of light scattered under such conditions are presented in Fig. 1. These spectra were measured using light incident at different angles for which the bright coloration was observed. The measurements were performed for two arbitrary orientations of the sample structure (face versus edge). Unfortunately, the small size of the sample did not allow the arrangement of sample faces to be specified.

As can be seen, one orientation of the sample clearly reveals the scattering of light in the long-wavelength visible spectral region, while the other orientation corresponds to scattering of the short-wavelength light. The pattern was repeated when the structure was rotated about the axis by an angle multiple of 60°. Radiation of sufficiently high spectral purity was observed in different angular intervals: spectra (1) and (2) presented in Fig. 1 were obtained within 15° and 5°, respectively. The observed spectral halfwidth (50–100 nm) allows the structures studied to be considered as miniature spectral filters.

Conclusion. The results of our experiments can be briefly summarized as follows. A method has been developed for (i) measuring the spectra of radiation transmitted through and scattered from a photon crystal structure with a transverse size below 10 μm and (ii) visual monitoring of the size of a periodic structure possessing a photon forbidden band in the visible spectral range and selecting such structures by color of the pattern observed in the reflected light.

We have measured the transmission spectra of two-dimensional periodic photon crystal structures. The spectra exhibit changes related to various polarizations of the incident light and different orientations of the incident beam relative to the sample structure. We have measured the spectra of radiation scattered at various angles from the two-dimensional periodic lattice. Using a certain orientation of the crystal relative to the incident radiation, it is possible to perform angular spectral filtration of the transmitted radiation. The tunable spectral range of filtration (from violet to red) and a rather narrow spectral width (50–100 nm) suggest that the two-dimensional periodic structures can be used as miniature spectral filters.

REFERENCES

1. R. D. Meade, K. D. Brommer, A. M. Rappe, and J. Joannopoulos, J. Opt. Soc. Am. B **10**, 323 (1993).
2. J. Broeng, T. Sondergaard, S. E. Barkou, *et al.*, J. Opt. A **1**, 477 (1999).
3. J. C. Knight, T. A. Birks, R. F. Cregan, and P. St. J. Russel, Opt. Mater. **11**, 143 (1999).
4. J. D. Joannopoulos, R. D. Meade, and J. N. Winn, *Photonic Crystals: Molding the Flow of Light* (Princeton Univ. Press, Princeton, 1995).
5. A. B. Fedotov, A. M. Zheltikov, L. A. Melnikov, *et al.*, Laser Phys. **10** (5), 723 (2000).

Translated by P. Pozdeev

Technical Physics Letters, Vol. 28, No. 4, 2002, pp. 275–278. Translated from Pis'ma v Zhurnal Tekhnicheskoĭ Fiziki, Vol. 28, No. 7, 2002, pp. 31–37.

On the High-Frequency Instability of Plasma in the Octupole Galathea Electric Discharge Trap

K. P. Kirdyashev, A. I. Morozov, A. I. Bugrova, and A. M. Bishaev

Institute of Radio Engineering and Electronics (Fryazino Branch), Russian Academy of Sciences, Fryazino, Moscow oblast, 141190 Russia

Institute of Nuclear Fusion, Russian Research Centre Kurchatov Institute, Moscow, 123182 Russia

Moscow Institute of Radio Engineering, Electronics, and Automatics (Technical University), Moscow, 117454 Russia

e-mail: kpk114@ire216.msk.su; efimov@ms.ire.rssi.ru

Received October 2, 2001; in final form, November 28, 2001

Abstract—Spectra of microwave plasma oscillations in an electric discharge trap are considered, and specific features of these spectra related to the instability of transverse current near the magnetic barrier confining the plasma are revealed. A relation between oscillations of the discharge current and the modulation of intensity of the microwave oscillations is established which indicates that the barrier region of discharge possesses an anomalous resistivity. *© 2002 MAIK "Nauka/Interperiodica".*

At present, several characteristics of the electric discharge plasma traps with confining magnetic barrier were studied [1–3]. Such traps employ a toroidal magnetic field generated by current-carrying conductors totally immersed in plasma (Fig. 1). The operating modes studied previously were characterized by a small plasma energy confinement time determined by the penetration of electrons through the magnetic barrier. It

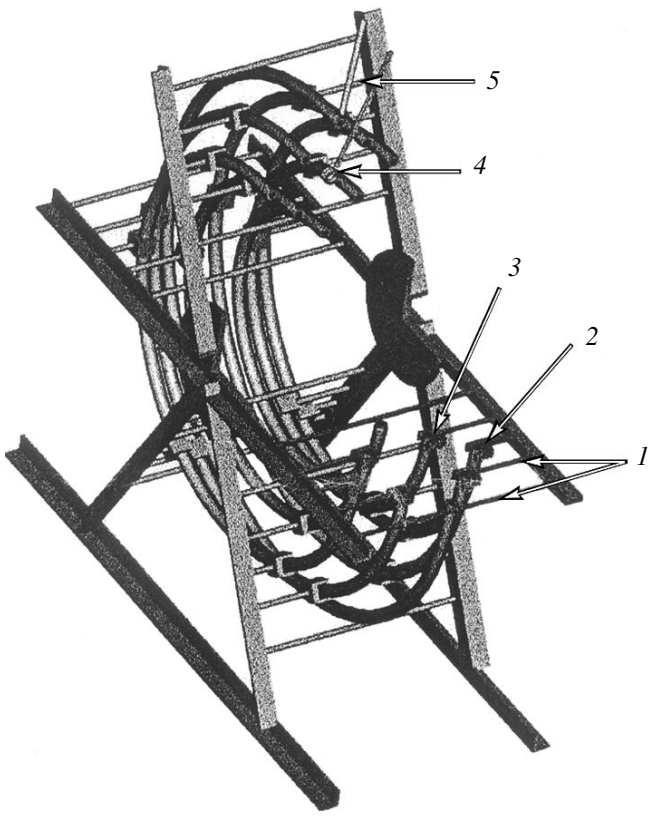

Fig. 1. Layout of the octupole galathea plasma trap: (*1*) base; (*2*) compensating coils; (*3*) mixines; (*4*) cathode; (*5*) gas supply tube.

1063-7850/02/2804-0275$22.00 © 2002 MAIK "Nauka/Interperiodica"

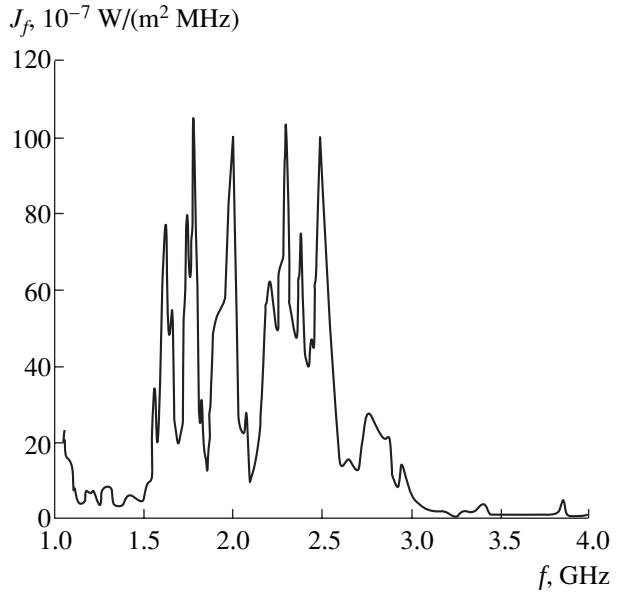

Fig. 2. Spectrum of the microwave radiation of a plasma trap (working gas, argon; gas flow rate, 0.9 cm^3/s; voltage, 60 V; magnetic field strength, 0.005 T).

was suggested that the effects related to the anomalous transverse mobility of electrons in the magnetic barrier are related to the excitation of microwave oscillations in the discharge [4, 5]. Recently [6], it was found that the microwave oscillations can be excited both in the axial region of plasma volume and in the magnetic barrier. The excitation terminates after turning off the discharge voltage. The experiments point to a nonstationary character of processes running in the plasma trap, which is manifested by fluctuations of the plasma parameters, discharge current, and intensity of microwave oscillations. The characteristic time scale of these fluctuations does not exceed 1 ms.

In this paper, we consider the results of an experimental investigation of the microwave radiation spectrum of an octupole plasma trap and the relation between the arising instability and fluctuations of the discharge current in the magnetic barrier confining the plasma. The obtained experimental data are used to discuss the possible mechanism and conditions for the onset of instability of the transverse current in the barrier plasma region.

The experiments were conducted on a vacuum test facility at the Laboratory of Physical Plasma Optics of the Moscow Institute of Radio Engineering, Electronics, and Automation. The plasma trap was operating in stationary modes with the electric discharge parameters presented in [6]. Special attention was paid to the nonstationary character of excitation of the microwave oscillations under study and the nonstationary passage of electrons (forming the discharge current) through the magnetic barrier.

The spectra of microwave oscillations can be monitored with the help of tunable microwave devices measuring the electromagnetic radiation emitted from the plasma trap; however, this approach restricts the ability of studying the development of oscillation processes and their temporal and spatial structure. At the same time, the spectra of microwave radiation measured with inertial devices are related to integral characteristics of the instability developing in the plasma volume, which is also of interest in diagnostic studies of the plasma confinement by the barrier magnetic field.

The experiments allow us to make two conclusions important for understanding processes running in the plasma trap. First, the observed irregularity of the microwave radiation spectra (Fig. 2) is characterized by a frequency spacing of 150–200 MHz between individual spectral components. This spacing corresponds to the Larmor frequency of electrons in a barrier magnetic field of 0.005–0.0075 T. Moreover, these spectral components appear in a frequency range of 1–3 GHz, corresponding to the Langmuir frequencies ω_{Pe} for an electron density of 10^{10}–10^{11} cm^{-3} in the magnetic barrier region [6].

Analyzing experimental data, we will assume that electrons are accelerated in a stationary electric discharge field to form a group of fast electrons with velocities $v_\perp \geq v_{Te}$ in the barrier region (here, v_{Te} is the thermal velocity of electrons formed in the course of ionization of the working gas (argon or hydrogen)). The need for taking into account the transverse velocities of electrons follows from a relation between the frequencies and characteristic dimensions of excited microwave oscillations, on the one hand, and the Larmor frequency ω_{Be} and the Larmor electron radius $\rho_{Be} = v_\perp/\omega_{Be}$ in the barrier region of discharge, on the other hand, at which the oscillations are excited in the domain of frequencies and wave numbers corresponding to $\omega \approx \omega_{Pe} > \omega_{Be}$ and $k_\perp \rho_{Be} \geq 1$ ($k_\perp$ is the transverse component of the wavenumber of excited oscillations). Note that determining the distribution of electron velocities near the magnetic barrier is a very complex problem because it requires considering a number of processes important for the electron dynamics, such as the acceleration of electrons in the electric discharge field, the ionization of the working gas, the effect of the barrier magnetic field, and the scattering of electrons by the excited oscillations. Under these conditions, we will adopt a simplified scheme for the development of plasma instability which takes into account the presence of a group of fast electrons in the barrier discharge region. This assumption qualitatively agrees with the results of the experiment conducted.

In accordance with [7], the condition for the excitation of microwave oscillations in the magnetic barrier reduces to the requirement that frequency $\omega_1 = (\omega_{Pe}^2 + \omega_{Be}^2)^{1/2}$ of the plasma self-oscillations propagating across the barrier magnetic field must be close to the

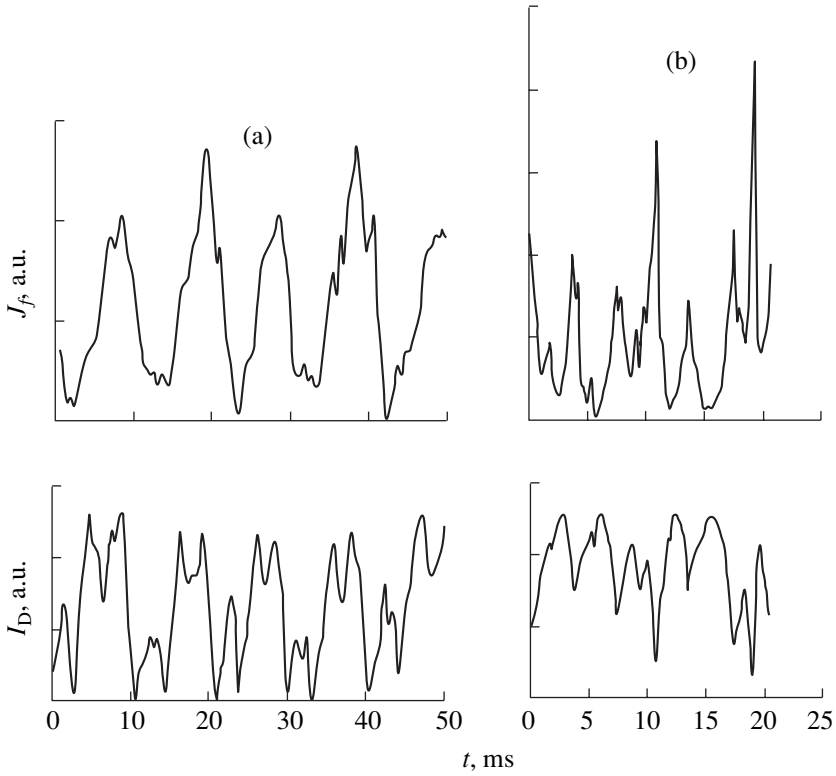

Fig. 3. Comparison of the envelope J_f of the microwave radiation generated in the plasma trap to fluctuations of the discharge current I_D in different modes of formation of the plasma structure: (a) gas flow rate, 3 cm^3/s; voltage, 200 V; magnetic field strength, 0.0075 T; (b) gas flow rate, 0.9 cm^3/s; voltage, 200 V; magnetic field strength, 0.0075 T.

harmonics of the electron Larmor frequency $n\omega_{Be}$. In this case, for harmonics with $|n| > 1$, the plasma density and the magnetic field are related as $(\omega_{Pe}/\omega_{Be})^2 = n^2 - 1$. Since the plasma near the magnetic barrier is inhomogeneous, the spectrum of Langmuir oscillations exhibits broadening determined by variations in the electron density. As a result, the spectrum of electromagnetic radiation includes harmonics of the cyclotron frequency. This is confirmed by the experiment, in which we isolate harmonics with numbers $n = 7$–15 (Fig. 2).

The second conclusion from the experiments is related to the modulation of intensity of the microwave oscillations, which appears in all modes of the electric discharge formation in the plasma trap. The envelopes of microwave oscillations recorded at several frequencies demonstrates that the plasma instability arises within limited time intervals of 0.1–1 ms, followed by breakdown of the oscillation process. Recording the envelope of microwave oscillations using spatially separated probes reveals a substantial correlation of the developing instability modulation process over the plasma volume, at least near the chosen current-carrying conductors.

Of special importance for understanding the contribution of the instability under study to the formation of the electric discharge mode in the trap is the comparison of bursts of the microwave radiation to fluctuations of the discharge current. Here we observe two fundamentally different typical situations: (i) the excitation of high-frequency instability at relatively weak microwave fields in the magnetic barrier region is accompanied by an increase in the discharge current (Fig. 3a) and (ii) an intense burst of the microwave radiation arises at the dip of the discharge current (Fig. 3b). This allows us to consider the development of instability in the barrier plasma region resulting in the "demagnetization" of electrons by the microwave oscillations, followed by the transformation of discharge into the mode with an anomalous resistivity of plasma during the formation of current through the magnetic barrier. The modes with the electron scattering by the oscillations as a factor determining the current passage through the plasma trap arise at a gas (argon) pressure in the plasma trap on the order of 3×10^{-4} Torr, when the degree of nonequilibrium of the microwave radiation (the excess over the thermal level of intensity) does not exceed 50. In this case, the statistical coefficient of correlation between the discharge current fluctuations and the microwave radiation envelope is about 0.6. As follows from Fig. 3a, within some time intervals, where the microwave radiation intensity increases above a threshold level of $\sim 10^{-8}$ W/(m^2 MHz), the modulation of the radiation envelope and fluctuations of the discharge current are out of phase. The modes with anomalous

resistivity of plasma (which are identified by the dip in the discharge current) are most pronounced at a small gas (argon) flow rate, which corresponds to a pressure of about 5×10^{-5} Torr and a degree of nonequilibrium of the microwave radiation up to $(2–5) \times 10^4$ (Fig. 3b). Under these conditions, the coefficient of correlation between the current and the microwave radiation envelope equals –0.9. It should be noted that, in all experiments conducted with hydrogen, fluctuations of the discharge current are out of phase with the microwave radiation envelope.

The experimental data obtained indicate that there exists a mechanism of the electron scattering by fluctuations of the electric field in the magnetic barrier confining the plasma. Moreover, it is the microwave oscillations that determine the formation of the electron flow from the cathode toward metal-coated current-carrying conductors, the trap design elements, and walls of the vacuum chamber playing the role of anodes. The development of plasma instability at cyclotron harmonics is a fundamentally nonstationary process: within certain time intervals, this is accompanied by the onset of an anomalous resistivity of the barrier discharge region. However, experimental data obtained to date do not allow us to reveal the reasons of breakdown of the intense microwave emission and the possible mechanisms of nonstationary processes in the barrier region of plasma.

REFERENCES

1. A. I. Morozov, A. I. Bugrova, A. M. Bishaev, *et al.*, Pis'ma Zh. Tekh. Fiz. **25** (17), 57 (1999) [Tech. Phys. Lett. **25**, 700 (1999)].
2. A. I. Morozov, V. A. Nevrovskiĭ, V. K. Kharchevnikov, *et al.*, in *Proceedings of the XXVI Zvenigorod Conference on Plasma Physics and Controlled Nuclear Fusion, 1999*, p. 38.
3. T. Ohkava and M. Yoshikava, Phys. Rev. Lett. **17**, 685 (1966).
4. A. I. Morozov, A. I. Bugrova, A. M. Bishaev, *et al.*, in *Proceedings of the XXVI Zvenigorod Conference on Plasma Physics and Controlled Nuclear Fusion, 1999,* p. 37.
5. A. M. Bishaev, A. I. Bugrova, K. P. Kirdyashev, *et al.*, in *Proceedings of the XXVII Zvenigorod Conference on Plasma Physics and Controlled Nuclear Fusion, 2000,* p. 62.
6. A. I. Morozov, K. P. Kirdyashev, A. I. Bugrova, *et al.*, Fiz. Plazmy **27** (7), 620 (2001) [Plasma Phys. Rep. **27**, 582 (2001)].
7. A. B. Mikhailovskii, *Theory of Plasma Instabilities* (Atomizdat, Moscow, 1975; Consultants Bureau, New York, 1974), Vol. 1.

Translated by A. Kondrat'ev

Technical Physics Letters, Vol. 28, No. 4, 2002, pp. 279–282. Translated from Pis'ma v Zhurnal Tekhnicheskoĭ Fiziki, Vol. 28, No. 7, 2002, pp. 38–45.

Effective Electromechanical Properties of Ferroelectric Piezoactive Composites of the Crystal–Ceramic Type Based on $(Pb_{1-x}Ca_x)TiO_3$

V. Yu. Topolov and S. V. Glushanin

Rostov State University, Rostov-on-Don, Russia

e-mail: topolov@phys.rnd.runnet.ru

Received September 12, 2001

Abstract—Based on the previously proposed models, effective electromechanical properties of the ferroelectric piezoactive composites of the "single-domain crystal–ceramic" and "polydomain crystal–ceramic" types are determined for the first time. Features of the concentration dependence of the piezoelectric coefficients of four types (e^*_{3j}, d^*_{3j}, g^*_{3j}, and h^*_{3j}) are interpreted. Advantages of the new composites in comparison with the known ferroelectric piezoceramic materials of the $PbTiO_3$ type are considered and explained. It is shown that the coefficients e^*_{3j} are most sensitive to a change in the system parameters; some reasons for this sensitivity are established. © *2002 MAIK "Nauka/Interperiodica".*

Ferroelectric piezoactive crystal–ceramic (FEPACC) composites have attracted the attention of researchers for several reasons. First, because features of the synthesis and microstructure of a FEPACC composite based on $(Pb_{1-x}Ca_x)TiO_3$ with $x \approx 0.24$ (a material with components possessing perovskite-like structures) were established [1]. Second, because FEPACC composites (in contrast to the ceramic–polymer systems [2]) contain components with comparable electromechanical parameters. Third, because no experimental data are available on the piezoelectric and other properties of FEPACC composites, which can be of importance in practical applications.

The purpose of this study was to model the effective electromechanical properties of the ferroelectric piezoactive composites based on $(Pb_{1-x}Ca_x)TiO_3$ and reveal advantages of these materials in comparison to the previously studied ferroelectric piezoceramics (FEPCs).

Consider a FEPACC composite (Fig. 1) polarized by an electric field $\mathbf{E} \parallel OX_3$ and containing a system of single- or polydomain inclusions in the form of thin disks oriented with their normals parallel to OX_3. In the presence of such inclusions, the system exhibits a significant relieving internal mechanical stresses related, for example, to a difference between elastic properties of the components [3], the interaction between compo-

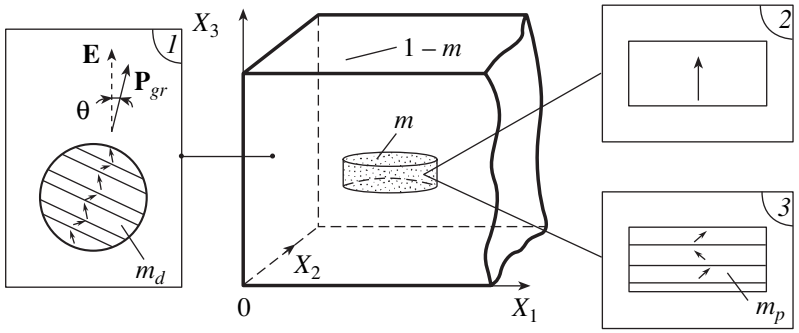

Fig. 1. A schematic diagram illustrating the FEPACC composite structure: (*1*) matrix comprising spherical grains divided into 90° domains; arrows indicate spontaneous polarization vectors $\mathbf{P}_{dj}$ of these domains; (*2*, *3*) crystalline inclusions in the form of thin single-domain (inset *2*) or polydomain (inset *3*) disk; arrows indicate spontaneous polarization vectors $\mathbf{P}_{sk}$ of domains in inclusions; m is the volume concentration of crystalline inclusions; $1 - m$ is the matrix volume concentration; m_d is the volume concentration of 90° domains with the $\mathbf{P}_{dj}$ vectors making smaller angles with the OX_3 axis; m_p is the volume concentration of domains having positive projections of vectors $\mathbf{P}_{sk}$ onto the OX_1 axis; $\theta = (\mathbf{P}_{gr}; \wedge OX_3)$ is the angle of orientation of the spontaneous polarization vector $\mathbf{P}_{gr} = m_d\mathbf{P_{d1}} + (1 - m_d)\mathbf{P_{d2}}$ of an individual grain relative to the polarizing field $\mathbf{E} \parallel OX_3$.

1063-7850/02/2804-0279$22.00 © 2002 MAIK "Nauka/Interperiodica"

nents during and after hot pressing [1], and the motion of boundaries between components [1]. The 90° domain walls in the FEPC grains and inclusions (see insets *1* and *3* in Fig. 1) are virtually immobile (this was experimentally established for $PbTiO_3$-based tetragonal FEPCs [4]) and make no contribution to the electromechanical properties of the components. The vectors $\mathbf{P}_{gr}$ of the polydomain grains of FEPCs are oriented so that $0 \le \theta \le \theta_m$ (see inset *1* in Fig. 1), where θ_m is the maximum angle between vectors $\mathbf{P}_{gr}$ and $\mathbf{E}$ (with an allowance for the 180° and 90° reorientations of domains in the tetragonal phase); note that $\theta_m = \arcsin[(2/3)^{1/2}] \approx 55°$ for $m_d = 1$ [5], or $\theta_m = 45°$ for $0.5 \le m_d < 1$ [6]. According to [6], below we characterize the residual polarization of FEPC by the angle $\theta' = 180° - \theta_m$.

The electromechanical constants of polydomain regions (see insets *1* and *3* in Fig. 1) are determined by averaging as described in [7, 8], after which the obtained values are averaged using the method of effective medium [9, 10]. Eventually, this yields a complete set of elastic, piezoelectric, and dielectric constants of FEPCs. Then, the sets of constants of the FEPC matrix and crystalline inclusions are used to determine the electromechanical properties of FEPACC composites within the framework of the matrix approach [11]. This approach is based on the Eshelby concept of the equivalent ellipsoidal inclusion [12], whereby the averaging procedure can be applied to composites in which both components are piezoactive.

The matrix of effective electromechanical constants of FEPACC composites determined by self-consistent method [13, 14] with allowance for the electromechanical interaction between components [11] is as follows:

$$\|C^*\| = \|C^{(FC)}\| + m(\|C^{(cr)}\| - \|C^{(FC)}\|) \times [\|I\| + (1-m)\|S\|\|C^{(FC)}\|^{-1}(\|C^{(cr)}\| - \|C^{(FC)}\|)]^{-1},$$

where

$$\|C^{(FC)}\| = \begin{pmatrix} \|c^{(FC),E}\| & \|e^{(FC)}\|^T \\ \|e^{(FC)}\| & -\|\varepsilon^{(FC),\xi}\| \end{pmatrix} \quad \text{and}$$

$$\|C^{(cr)}\| = \begin{pmatrix} \|c^{(cr),E}\| & \|e^{(cr)}\|^T \\ \|e^{(cr)}\| & -\|\varepsilon^{(cr),\xi}\| \end{pmatrix}$$

are the matrices of electromechanical constants of FEPCs and crystal, respectively; $\|I\|$ is the unitary matrix; $\|S\|$ is the matrix of the Eshelby coefficients depending on the $\|C^{(FC)}\|$ elements and the shape of inclusions [11]; $\|c^E\|$, $\|e\|$, and $\|\varepsilon^\xi\|$ are the matrices of elastic moduli, piezoelectric coefficients, and dielectric permittivities, respectively; the superscripts *, (*FC*), and (*cr*) refer to FEPACC, FEPC, and crystals, respectively; and *T* denotes transposition. The calculations were performed with the room-temperature electromechanical constants of single-domain $(Pb_{1-x}Ca_x)TiO_3$ crystals.[1] Figure 2 shows the most interesting examples of concentration (versus *m* or m_d) and orientation (versus θ') dependences of the effective piezoelectric coefficients e^*_{3j}, $d^*_{3j} = e^*_{3q}s^{*E}_{qj}$, $g^*_{3j} = d^*_{3j}/\varepsilon^{*\sigma}_{33}$, and $h^*_{3j} = e^*_{3j}/\varepsilon^{*\xi}_{33}$ characterizing the response of FEPACC composites along the polarization axis OX_3. These curves were calculated for composites of the following types: "single-domain crystal ($x = 0$)– FEPC ($x = 0$, $m_d = 0.5$)" (FEPACC-1, 4*mm* symmetry); "single-domain crystal ($x = 0$)–FEPC ($x = 0.24$, $0.5 \le m_d \le 0.9$)" (FEPACC-2, 4*mm* symmetry); and "polydomain crystal ($x = 0.24$, $m_p = 0.5$)–FEPC ($x = 0.24$, $0.5 \le m_d \le 0.9$)" (FEPACC-3, *mm*2 symmetry). In all these cases the bulk concentration *m* of crystals does not exceed 0.5 [1]. Let us consider some features of these dependences.

1. The piezoelectric coefficients e^*_{3j} are highly sensitive to variations of the angle θ' and concentrations *m* and *x* characterizing the inclusions. The nonmonotonic variation of $e^*_{31}(m)$ and $\operatorname{sgn} e^*_{31}$ (and, hence, the possibility of $e^*_{33}/|e^*_{31}| \longrightarrow \infty$) are related to a considerable extent to the domain-orientation processes in the crystals (Fig. 2a) or to the domain structure of inclusions (Fig. 2c). An increase in θ' and in the residual polarization of FEPC significantly influences the elastic compliances $s^{(FC),E}_{pq}$ and piezoelectric moduli $d^{(FC)}_{pq}$ determining to a considerable degree the behavior of $e^*_{3j}(m)$. In contrast to this, an increase in m_d does not significantly influence the behavior of $s^{(FC),E}_{pq}$, $d^{(FC)}_{pq}$, and $e^*_{3j}(m)$ (cf., e.g., curves *2*, *4*, and *6* in Fig. 2c). A unique example of simultaneous increase of all $e^*_{3j} > 0$ ($j = 1$–3) in a broad range of *m* is offered by curves *7*–*9* in Fig. 2c. In contrast to FEPACC composites, most of the perovskite-like FEPC possess $e^{(FC)}_{31} = e^{(FC)}_{32} < 0$ and $e^{(FC)}_{33} > 0$ [16].

[1] For example, calculations according to [9] for $x = 0.24$ yield for the elastic compliances: $s^E_{11} = 7.09$, $s^E_{12} = -1.61$, $s^E_{13} = -6.85$, $s^F_{33} = 30.4$, $s^E_{44} = 12.8$, $s_{66} = 7.60$ (in 10^{-12} Pa^{-1}); piezoelectric moduli: $d_{33} = 188$, $d_{31} = -40.8$, $d_{15} = 68.6$ (in pC/N); dielectric permittivities: $\varepsilon^\sigma_{11}/\varepsilon_0 = 213$, $\varepsilon^\sigma_{33}/\varepsilon_0 = 198$. For $x = 0$, the complete sets of s^E_{jk}, d_{pq}, and ε^σ_{jj} for mono- and polydomain ($m_p = 0.5$) crystals (see insets *2* and *3* in Fig. 1) were presented in [6]. The transitions $s^E \longrightarrow c^E$, $d \longrightarrow e$, and $\varepsilon^\sigma \longrightarrow \varepsilon^\xi$ are performed according to well-known formulas [15].

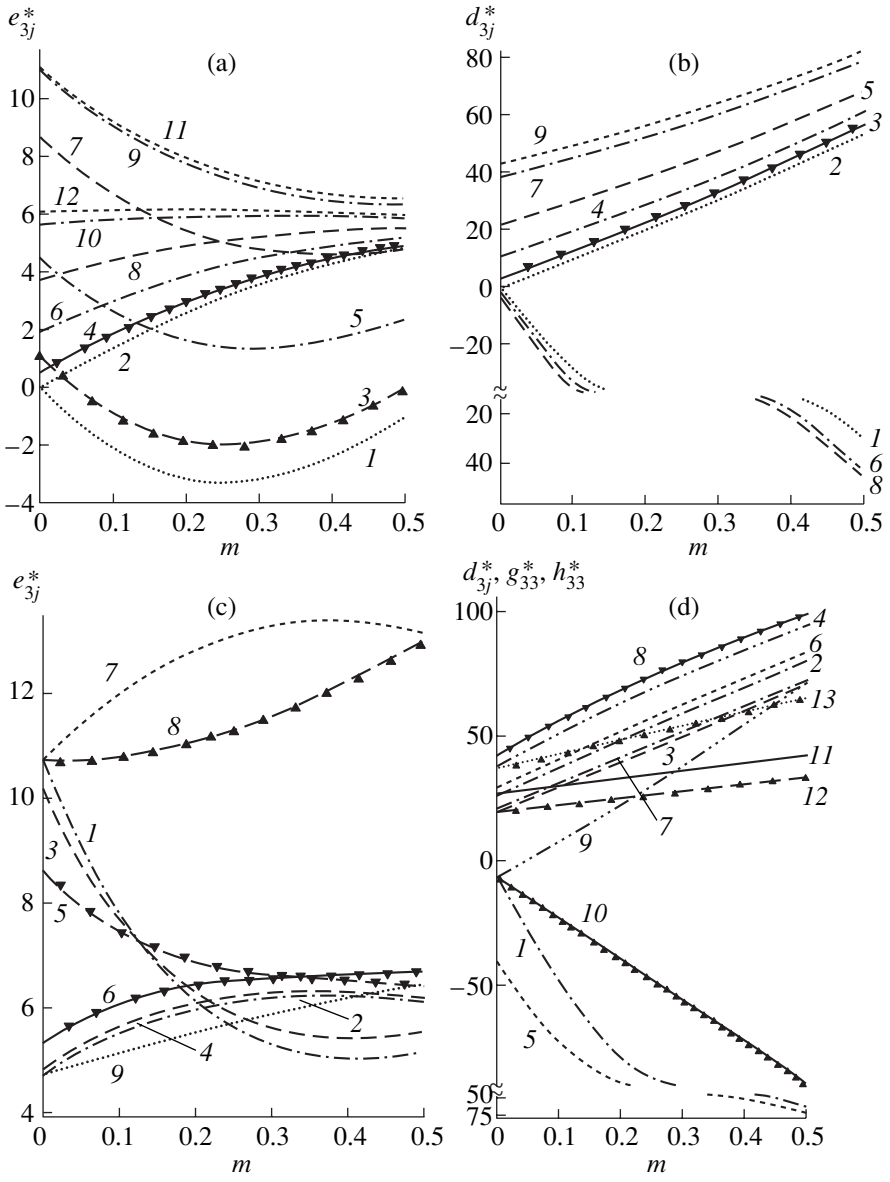

Fig. 2. Calculated concentration and orientation dependences of effective piezoelectric coefficients e^*_{3j} (C/m^2), d^*_{3j} (pC/N), g^*_{33} (mV m/N), and h^*_{33} (10^8 V m) for (a, b) FEPACC-1 and (c, d) FEPACC-2 and FEPACC-3 composites based on $(Pb_{1-x}Ca_x)TiO_3$: (a) $10e^*_{31}$, curves *1*, *3*, *5*, *7*, *9*, *11* constructed for θ' = 0°, 30°, 60°, 90°, 125°, and 135°, respectively; e^*_{33}, curves *2*, *4*, *6*, *8*, *10*, *12* constructed for θ' = 0°, 30°, 60°, 90°, 125°, and 135°, respectively; (b) $10d^*_{31}$, curves *1*, *6*, *8* constructed for θ' = 0°, 125°, and 135°, respectively; d^*_{33}, curves *2*, *3*, *4*, *5*, *7*, *9* constructed for θ' = 0°, 30°, 60°, 90°, 125°, and 135°, respectively; (c) $10e^*_{31}$, curves *1*, *3*, *5* constructed for m_d = 0.5, 0.7, and 0.9, respectively; e^*_{33}, curves *2*, *4*, *6* constructed for m_d = 0.5, 0.7, and 0.9, respectively, of FEPACC-2; and $10e^*_{31}$ (*7*), $10e^*_{32}$ (*8*), e^*_{33} (*9*) of FEPACC-3; (d) $10d^*_{31}$, curves *1* and *5* constructed for m_d = 0.5 and 0.9, respectively; d^*_{33}, curves *2* and *6* constructed for m_d = 0.5 and 0.9, respectively; g^*_{33}, curves *3* and *7* constructed for m_d = 0.5 and 0.9, respectively; h^*_{33}, curves *4* and *8* constructed for m_d = 0.5 and 0.9, respectively, of FEPACC-2; and $10d^*_{31}$ (*9*), $10d^*_{32}$ (*10*), d^*_{33} (*11*), g^*_{33} (*12*), h^*_{33} (*13*) of FEPACC-3.

2. The concentration dependences of $d^*_{3j}(m)$, $g^*_{33}(m)$, and $h^*_{33}(m)$ for FEPACC composites are monotonic (Figs. 2b and 2d). Approximately equal derivatives $[d^*_{3j}(m)]'$ (cf., e.g., the slopes of curves *1*, *6*, *8*, or *2–5*, *7*, *9* in Fig. 2b) are indicative of a significant influence of the piezoelectric moduli $d^{(cr)}_{3j}(m)$ of the crystal upon $d^*_{3j}(m)$ of FEPACC composites at various θ'. This is related, in particular, to the experimentally observed

large anisotropy $d_{33}^{(FC)}/d_{31}^{(FC)}$ of FEPC with $x \approx 0.24$ [17, 18] and the change in sign of $d_{31}^{(FC)}(E)$ of FEPC based on $(Pb_{1-x}Ca_x)TiO_3$ [18, 19] (an analogous dependence $d_{31}^{(FC)}(\theta')$ for $x = 0$ was calculated in [10]). For this reason, the introduction of crystals into the FEPC matrix leads to $d_{31}^* \approx m d_{31}^{(cr)}$ and to a rather slow increase in $d_{33}^*(m)$, which eventually significantly decreases the anisotropy of d_{3j}^*. In addition, in a broad range of m, FEPACC composites obey the condition $\operatorname{sgn} d_{33}^* = \operatorname{sgn} d_{31}^* = -\operatorname{sgn} d_{32}^* > 0$ (see curves *9–11* in Fig. 2d), which is closely connected to the relationship $d_{31}^{(cr)} \approx -d_{32}^{(cr)}$ ($x = 0$) [6] (which is unusual for polydomain crystals).

3. The variation of $g_{33}^*(m)$ and $h_{33*}(m)$ within broad limits is explained primarily by a difference in the permittivities $\varepsilon_{kk}^{(cr),\sigma}$ and $\varepsilon_{kk}^{(FC),\sigma}$. At the same time, variation of the bulk concentration of 90° domains in FEPC grains in the interval $0.5 \le m_d \le 0.9$, leading to small changes in $\varepsilon_{kk}^{(FC),\sigma}$ (below 3% according to estimates obtained by method [9]) affects neither $g_{3j}^*(m)$ nor $h_{3j}^*(m)$ of FEPACC-2. A difference in the molar concentration x of the components leads to a significant increase in g_{33}^* and h_{33}^*. For example, the calculated values of g_{33}^* and h_{33}^* of FEPACC-2 (see curves *3*, *7* and *4*, *8* in Fig. 2d) for $m \approx 0.5$ exceed the experimental values of $g_{33}^{(FC)}$ and $h_{33}^{(FC)}$ for FEPC based on modified $PbTiO_3$ [16] by a factor of 2.2 and 1.9, respectively.

Thus, we have made the first step in the theoretical investigation of the physical properties of FEPACC composites—a new class of functional materials for electronics. Despite a very restricted volume of available experimental data, we entertain that FEPACC composites are promising materials due to high values of the parameters $e_{33}^*/|e_{31}^*|$, $d_{33}^*/|d_{31}^*|$, g_{33}^*, h_{33}^* and the ability of reaching $e_{3j}^* > 0$ for $j = 1$–3. The examples of concentration (versus m or m_d) and orientation (versus θ') dependences of the effective piezoelectric coefficients, and the comparison of these curves to the experimental data for related FEPCs, show evidence of a unique piezoelectric response of FEPACC composites based on $(Pb_{1-x}Ca_x)TiO_3$.

Acknowledgments. The authors are grateful to E.S. Tsikhotskiĭ and V.V. Eremkin for fruitful discussions concerning the experimental investigation of the FEPACC composite structure and the domain structure of the system components.

REFERENCES

1. V. G. Smotrakov, V. V. Eremkin, V. A. Aleshin, and E. S. Tsikhotskiĭ, Izv. Akad. Nauk, Ser. Fiz. **64** (6), 1220 (2000).
2. S. V. Glushanin and V. Yu. Topolov, Pis'ma Zh. Tekh. Fiz. **27** (15), 15 (2001) [Tech. Phys. Lett. **27**, 626 (2001)].
3. T. Mura, *Micromechanics of Defects in Solids* (Martins Nijhoff Publ., Dordrecht, 1987).
4. A. D. Feronov, V. V. Kuleshov, V. P. Dudkevich, and E. G. Fesenko, Zh. Tekh. Fiz. **50** (3), 621 (1980) [Sov. Phys. Tech. Phys. **25**, 372 (1980)].
5. L. P. Kholodenko, *Thermodynamic Theory of Ferroelectrics of the Barium Titanate Type* (Zinatne, Riga, 1971).
6. A. V. Turik, V. Yu. Topolov, and V. I. Aleshin, J. Phys. D **33** (6), 738 (2000).
7. A. V. Turik, Fiz. Tverd. Tela (Leningrad) **12** (3), 892 (1970) [Sov. Phys. Solid State **12**, 688 (1970)].
8. E. Akcakaya and G. W. Farnell, J. Appl. Phys. **64** (9), 4469 (1988).
9. V. Yu. Topolov, A. V. Turik, and A. I. Chernobabov, Kristallografiya **39** (5), 884 (1994) [Crystallogr. Rep. **39**, 805 (1994)].
10. A. V. Turik and V. Yu. Topolov, J. Phys. D **30** (11), 1544 (1997).
11. T.-L. Wu and J. H. Huang, Int. J. Solids Struct. **37** (21), 2981 (2000).
12. J. D. Eshelby, Solid State Phys. **3**, 79 (1956).
13. T. Mori and K. Tanaka, Acta Metall. **21** (5), 571 (1973).
14. M. Dunn, J. Appl. Phys. **78** (3), 1533 (1995).
15. I. S. Zheludev, *Physics of Crystalline Dielectrics* (Nauka, Moscow, 1968; Plenum, New York, 1971).
16. *Landolt-Börnstein: Zahlenwerte und Funktionen aus Naturwissenschaften und Technik. Neue Serie* (Springer-Verlag, Berlin, 1984, 1990), Gr. III, Bd. 18; Bd. 28.
17. N. Ichinose, Y. Fuse, Y. Yamada, and R. Sato, Jpn. J. Appl. Phys., Suppl. **28** (2), 87 (1989).
18. A. V. Gorish, V. P. Dudkevich, M. F. Kupriyanov, A. E. Panich, and A. V. Turik, *Piezoelectric Instrument-Making*, Vol. 1: *Physics of Ferroelectric Ceramic*, Ed. by A. V. Gorish (IPRZhR, Moscow, 1999).
19. D. Damjanovic, T. R. Gururaja, S. J. Jang, and L. E. Cross, in *Proceedings of the 6th IEEE International Symposium on Applications of Ferroelectrics (ISAF'86), Bethlehem, 1986* (New York, 1986), p. 344.

Translated by P. Pozdeev

Technical Physics Letters, Vol. 28, No. 4, 2002, pp. 283–285. Translated from Pis'ma v Zhurnal Tekhnicheskoĭ Fiziki, Vol. 28, No. 7, 2002, pp. 46–51.

The Structure of Granular Amorphous Carbon Films with Cobalt Nanoparticles

V. I. Siklitskiĭ[a], L. V. Lutsev[b,*], and M. V. Baĭdakova[b]

[a] *Ioffe Physicotechnical Institute, Russian Academy of Sciences, St. Petersburg, 194021 Russia*

[b] *DOMEN Research Institute, St. Petersburg, Russia*

* *e-mail: lutsev@domen.ru*

Received November 19, 2001

Abstract—The films of amorphous hydrogenated carbon containing cobalt nanoparticles are studied by small-angle X-ray scattering (SAXS). The SAXS pattern structure reveals the presence of two types of scattering centers, one of which represents cobalt particles. It is suggested that the second type of scattering centers can represent the groups of nanoparticles possessing a localized electron wavefunction and forming a cluster electron state. © *2002 MAIK "Nauka/Interperiodica".*

Introduction. Granulated films comprising nanoparticles (grains) distributed in an insulating matrix are considered as promising materials for new nanoelectronic devices. This is related to the fact that, for the systems with granules on the order of a few nanometers, the electrostatic energy of a granule charged with one electron is significantly greater than the thermal energy kT (for T = 300 K), which leads to manifestations of the macroscopic quantization and Coulomb blocking effects [1– 3]. This fact indicates that the average dimensions of granules and other objects are important characteristics of such granulated systems.

In this work, we have studied the structure of granulated amorphous carbon films containing cobalt nanoparticles by the method of small-angle X-ray scattering (SAXS). An advantage of the SAXS method is the possibility of probing objects possessing nanometer dimensions and analyzing the structure of granulated systems [4]. It was found that the SAXS patterns obtained from the granulated films studied are determined by the presence of scattering centers of at least two types: cobalt granules and objects with dimensions exceeding 5 nm. It was suggested that these objects can be identified as groups of granules possessing a localized electron wavefunction and forming a cluster electron state.

Experiment. The experimental investigations were performed on the samples of amorphous hydrogenated carbon containing nanodimensional cobalt inclusions, designated as $(a\text{-}C{:}H)_{1-x}Co_x$. The $(a\text{-}C{:}H)_{1-x}Co_x$ films were grown on amorphous silicon substrates by dc magnetron cosputtering of graphite and cobalt targets in an argon–hydrogen plasma (80% Ar + 20% H_2). The content of cobalt in the amorphous carbon deposit was monitored by measuring the K_α and K_β lines of the characteristic X-ray emission from Co atoms. The exact determination of the cobalt content in the films was performed by Rutherford backscattering. This investigation was performed on the $(a\text{-}C{:}H)_{1-x}Co_x$ films with x = 0.24–0.46; the film thicknesses ranged from 250 to 550 nm.

The SAXS measurements were performed in the interval of wave vectors 0.04 Å^{-1} < q < 0.7 Å^{-1} ($q = 2\pi\sin(2\Theta_{Br})/\lambda$), which corresponds to the scattering angles 0.5° < $2\Theta_{Br}$ < 10°. The scattered radiation was measured using a single-crystal scheme in a (Θ, 2Θ) geometry. The measurements were performed on a Dmax-B/RC diffractometer (Rigaku Co., Japan) using CuK_α radiation (λ = 1.5418 Å). Typical experimental SAXS curves are presented in Fig. 1. The presence of a

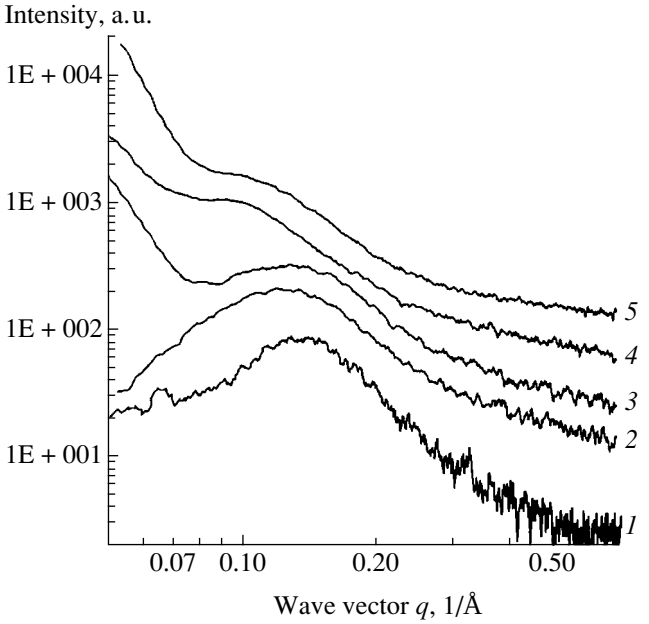

Fig. 1. SAXS curves for $(a\text{-}C{:}H)_{1-x}Co_x$ films with x = 0.24 (*1*), 0.30 (*2*), 0.35 (*3*), 0.44 (*4*), and 0.46 (*5*).

1063-7850/02/2804-0283$22.00 © 2002 MAIK "Nauka/Interperiodica"

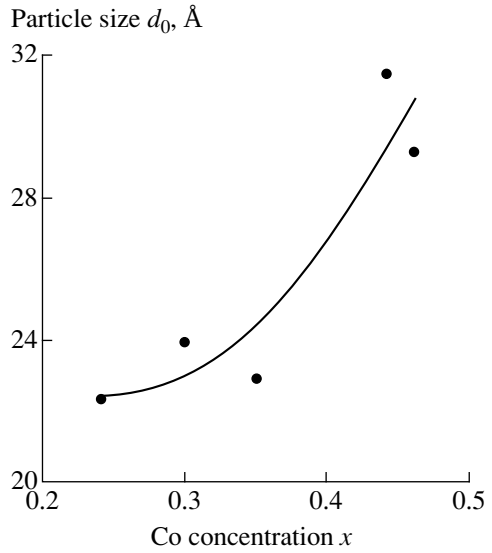

Fig. 2. The plot of average granule size d_0 versus cobalt content x in $(a\text{-}C{:}H)_{1-x}Co_x$ films.

granulated structure is confirmed by the local maxima observed at $q = 0.10$–0.14 Å^{-1} in the SAXS patterns of all samples. These maxima correspond to the X-ray scattering from Co particles and depend on the size of these particles. During the cosputtering of cobalt and carbon targets and codeposition of the sputtered material, cobalt enters the amorphous carbon matrix in the form of granules, which is confirmed by the method of electron microscopy and electron diffraction [5]. In addition to the maxima related to the scattering from Co granules, our SAXS patterns revealed an additional component at $q < 0.10$ Å^{-1}, which corresponds to scattering from the objects with dimensions significantly greater than the size of cobalt granules. This scattering component was insignificant in the samples with small Co content and sharply increased with the cobalt content. The size of these scattering centers exceeds 50 Å.

Figure 2 shows a plot of the average granule size versus cobalt content in the samples, constructed by the results of processing of the SAXS peaks due to metal granules. As can be seen, the average granule size d_0 increases with x. In the first approximation, the experimental relationship can be described by the formula d_0 [Å] $= 32.9 - 86.0x + 177x^2$; the scatter of granule dimensions was $\Delta d = 7$ Å.

Discussion. Let us consider a model explaining the formation of scattering centers with dimensions greater than the granule size d and predicting a sharp growth in the SAXS intensity with increasing concentration of metal nanoparticles. Under certain conditions, the wavefunction of an electron occurring on the Fermi level in a granule can be localized on a group (cluster) of granules [6]. Let us call this formation the cluster electron state (CES). The characteristic CES size is determined by localization of the electron wavefunction, which depends on the distribution of the depths of potential wells formed by the metal granules and on the coefficient of electron tunneling between granules.

Let us consider the case when the granule size $d = d_0 + \Delta d$ plays the role of the random parameter. In this case, the CES localization can be described by the Anderson localization model [7–9]. The random distribution of d leads to a random variation of the electric capacitance C_α and the potential well depth of the granules. The latter value varies with the capacitance from $W_0 + \min(e^2/2C_\alpha)$ to $W_0 - \max(e^2/2C_\alpha)$, where W_0 is the well depth without allowance for the Coulomb shift and $e^2/2C_\alpha$ is the Coulomb energy shift induced by the electron present on the granule α. The CES localization size L below the percolation threshold is determined by scatter of the well depths $V_0 = \max(e^2/2C_\alpha) - \min(e^2/2C_\alpha) = 2e^2\Delta d/\varepsilon(d_0^2 - \Delta d^2)$. In the first Born approximation, this scatter equals the electron mean free path over a manifold of wells with a "vertical" disorder [8]:

$$\frac{1}{L} = \frac{2\pi}{\hbar}\left(\frac{V_0}{2}\right)^2 \frac{(d_0 + l)^3 g(\varepsilon_F)}{u_F}, \qquad (1)$$

where ε is the dielectric permittivity of the matrix; l is the average distance between granules; $g(\varepsilon_F) = k_F m^*/(2\pi^2\hbar^2)(d_0/(d_0 + l))^3$ is the average density of electron states on the Fermi level ε_F in the metal (per unit energy, per unit volume of the granulated structure); and $u_F = \hbar k_F/m^*$ is the electron velocity on the Fermi surface with a wave vector k_F. To the first approximation in $\Delta d/d_0$, the effective mass of electron m^* is related to the coefficient of tunneling I between granules by the formula [8]

$$m^* = \frac{\hbar^2}{2I(d_0 + l)^2}. \qquad (2)$$

In order to determine the CES localization size L as a function of the metal content, let us assume that the average dimensions of matrix atoms A and metal atoms Me in the granulated composition $A_{1-x}Me_x$ are v_A and v_{Me}, respectively. Then the relative metal content is

$$x = \frac{v_A d_0^3}{v_{Me}[(d_0 + l)^3 - d_0^3]}. \qquad (3)$$

Taking into account formulas (2) and (3), relationship (1) for the CES localization for $l \gg d_0$ can be written as follows:

$$L = 16\pi d_0\left(\frac{v_A}{v_{Me}x}\right)^{4/3}\left(\frac{I}{V_0}\right)^2. \qquad (4)$$

The electron tunneling coefficient I entering into this expression depends exponentially on the distance l [10, 11]: $I \propto \exp(-pl)$, where p is a coefficient depend-

ing on the tunneling type and barrier height. To the first approximation in d_0/l, formula (3) yield $l \propto x^{-1/3}$. Taking this into account and using relationship (4), we conclude that the CES localization size must sharply increase with increasing metal content x. Moreover, the increase in L and in the amount of cluster electron states with the metal content is additionally favored by an increase in the tunneling coefficient I for electrons with energies below the Fermi level.

Thus, although the existence and properties of CES require additional experimental verification and rigorous theoretical investigation with allowance for a number of additional factors, the above simplified model leads to the conclusion that the formation of cluster electron states in granulated structures well explains both the existence of SAXS centers with dimensions exceeding the metal granule size and an increase in the SAXS intensity for $q < 0.10$ Å^{-1} with increasing metal content x.

Acknowledgments. The authors are grateful to T.K. Zvonareva for the preparation of samples, to V.M. Lebedev for the analysis of compositions, and to L.A. Lazebnaya for the determination of cobalt in films.

This study was supported by the Russian Foundation for Basic Research, project no. 99-02-17071a.

REFERENCES

1. S. V. Vyshenski, Pis'ma Zh. Éksp. Teor. Fiz. **61** (1–2), 105 (1995) [JETP Lett. **61**, 111 (1995)].
2. S. V. Vyshenski, Pis'ma Zh. Éksp. Teor. Fiz. **64** (7), 543 (1996) [JETP Lett. **64**, 592 (1996)].
3. S. A. Gurevich, V. V. Horenko, L. Yu. Kupriyanov, *et al.*, Pis'ma Zh. Éksp. Teor. Fiz. **64** (10), 684 (1996) [JETP Lett. **64**, 736 (1996)].
4. I. V. Rozhanskiĭ, D. A. Zakheim, T. N. Vasilevskaya, and S. A. Gurevich, Fiz. Tverd. Tela (St. Petersburg) **43** (5), 892 (2001) [Phys. Solid State **43**, 927 (2001)].
5. T. Hayashi, S. Hirono, M. Tomita, and S. Umemura, Nature (London) **381**, 772 (1996).
6. L. V. Lutsev, S. V. Yakovlev, and V. I. Siklitskiĭ, Fiz. Tverd. Tela (St. Petersburg) **42** (6), 1105 (2000) [Phys. Solid State **42**, 1139 (2000)].
7. P. W. Anderson, Phys. Rev. **109** (5), 1492 (1958).
8. N. F. Mott and E. A. Davis, *Electronic Processes in Non-Crystalline Materials* (Clarendon, Oxford, 1979; Mir, Moscow, 1982).
9. H. Böttger and V. V. Bryksin, *Hopping Conduction in Solids* (Akademie-Verlag, Berlin, 1985), p. 398.
10. C. B. Duke, *Tunneling in Solids* (Academic, New York, 1969), p. 354.
11. A. S. Davydov, *Quantum Mechanics* (Nauka, Moscow, 1973; Pergamon, Oxford, 1976).

Translated by P. Pozdeev

Technical Physics Letters, Vol. 28, No. 4, 2002, pp. 286–288. Translated from Pis'ma v Zhurnal Tekhnicheskoĭ Fiziki, Vol. 28, No. 7, 2002, pp. 52–56.

The First-Order Phase Transition as a Result of the Parametric Action of a Thermal Field

Yu. A. Kartashov and I. V. Popov

Northwest State Correspondence Technical University, St. Petersburg, Russia

e-mail: office@nwpi.ru

Received July 13, 2001

Abstract—The dynamics of an infinite chain of like particles linked both to each other and to a certain immobile base (a chain of bound oscillators) is considered. The chain of oscillators occurs in a variable and spatially inhomogeneous thermal electromagnetic field inducing significant fluctuations in the shape of potential of the interparticle interaction. It is shown that the field action renders the bound oscillators a parametric system pumped by the thermal field. An increase in the temperature (accompanied by an increase in the spectral density and frequency range of the thermal field) leads to an increase in the relaxation time of oscillators and eventually to their self-excitation. A condition of the corresponding first-order phase transition is obtained. *© 2002 MAIK "Nauka/Interperiodica".*

As is known, phase transitions are caused by the loss of stability of the initial phase. However, a thermodynamic approach dominates at present because it is still unclear which mechanism leads to the loss of stability on a microscopic level (see, e.g., recent review [1]).

Here we propose a qualitatively new approach to solving this problem. Based on [2, 3], it is possible to demonstrate that the mean-square strength of a quasi-stationary electric component of the internal thermal electromagnetic field in a substance even at rather low temperatures is on the order of 10^9–10^{10} V/m. This very strong field eventually leads to considerable fluctuations in the shape of potentials of intermolecular interactions. Thus, the oscillations of particles in a substance should be considered as parametric oscillations pumped by the thermal field. We will show that such a parametric system exhibits self-excitation at a certain temperature. We believe that this can be one of the reasons of the first-order phase transitions.

The medium will be modeled by an infinite one-dimensional chain of like particles with a mass m, linked both to each other and to a certain immobile base. The chain occurs in a thermal electromagnetic field F. The equation of the particle dynamics is

$$m(\partial^2 X/\partial t^2) = F(t, x, X, \partial X/\partial t, \partial^2 X/\partial x^2), \qquad (1)$$

where x is the coordinate of the particle center of mass along the chain and $X(x, t)$ is the particle displacement.

Let us assume that an ensemble-average value of the force F is zero and both the displacement and its derivatives are sufficiently small. Expanding the force F in powers of these quantities and restricting the consideration to the linear approximation, we obtain

$$\begin{aligned} F &= F(t, x) + mv^2(1 + \tilde{a})(\partial^2 X/\partial x^2) \\ &\quad + m\omega_0^2 X + (m/\tau)(\partial X/\partial t), \end{aligned} \qquad (2)$$

where v is the ensemble-average velocity of elastic waves; τ is the relaxation time; $v^2 = \beta r_0^2/m$ and $\omega_0 = \sqrt{\beta_0/m}$, β, β_0 are the coefficients of elasticity of the interparticle bonds and the bonds between particles and the base; r_0 is the intermolecular spacing; and $\tilde{a}$ is the random quantity with zero mean, which takes into account the mutual influence of elastic waves via the field excited by these waves (i.e., the mutual influence of phonons). Based on Eqs. (1) and (2), we obtain

$$\begin{aligned} m[(\partial^2 X/\partial t^2) - v^2(1 + \tilde{a})(\partial^2 X/\partial x^2) \\ + \tau^{-1}(\partial X/\partial t) + \omega_0^2 X] = F(t, x). \end{aligned} \qquad (3)$$

Equation (3) can be written in the spectral representation:

$$\begin{aligned} \xi(\omega, k) + \omega_0^2 K(\omega, k) \int_{-\infty}^{\infty}\int (k_1^2/k_0^2)\alpha(\omega - \omega_1, k - k_1) \\ \times \xi(\omega_1, k_1) d\omega_1 dk_1 = K(\omega, k) f(\omega, k), \end{aligned} \qquad (4)$$

where

$$K(\omega, k) = [(\omega_0^2 + k^2 v^2 - \omega^2 + i\omega/\tau)m]^{-1},$$

$$k_0 = \omega_0/v; \quad \xi(\omega, k), \quad f(\omega, k), \quad \alpha(\omega, k)$$

are the spectral amplitude of $X(t, x)$, $F(t, x)$ and $\tilde{a}(t, x)$.

1063-7850/02/2804-0286$22.00

Equations (3) and (4) are essentially the equations of parametric oscillations with pumping determined by the function $\tilde{a}(t, x)$. We can also consider these equations as describing a certain spatially distributed system with a transmission coefficient $K(\omega, k)$ and a feedback $(k_1^2/k_0^2)\alpha(\omega, k)$. Solving Eq. (4) by the Dyson method [4], we obtain the energy spectrum of $X(t, x)$ in the following form:

$$g_X(\omega, k)\left\{1 - \omega_0^4 \int_{-\infty}^{\infty}\int [K(\omega, k)K(\omega_1, k_1) + K^*(\omega, k)K^*(\omega_1, k_1)][(k^2k_1^2/k_0^4) \times g_a(\omega - \omega_1, k - k_1)]d\omega_1 dk_1\right\} - \omega_0^4|K(\omega, k)|^2 \quad (5)$$

$$\times \int_{-\infty}^{\infty}\int (k_1^4/k_0^4)g_X(\omega_1, k_1)g_a(\omega - \omega_1, k - k_1) = |K(\omega, k)|^2 g_F(\omega, k),$$

where the asterisk indicates complex conjugate; $g_a(\omega, k)$ and $g_F(\omega, k)$ are the spectral densities of the random functions $\tilde{a}(t, x)$ and $F(t, x)$, respectively. In deriving the integral in Eq. (5), we assumed the functions $\tilde{a}$ and F to be stationary and statistically independent.

The experimental Raman spectra show that the anti-Stokes components (and, hence, the thermal phonons) exist in a broad range of spatial and wave frequencies and in a wide temperature interval [5]. For this reason, we may suggest that the spectral densities $g_a(\omega, k)$ and $g_F(\omega, k)$ also exist in the wide ranges of ω and k. Assuming for simplicity that $g_a(\omega, k)$ is constant in the interval $\omega \in \pm\omega_m$ and $k \in \pm k_m$ (that is, $g_a(\omega, k) = G_a$) and that

$$\omega_m/\omega_0 \gg 1, \quad k_m \gg \omega_0/v,$$

we obtain that $G_a = \sigma_a^2/4\omega_m k_m$, where σ_a^2 is the dispersion of $\tilde{a}$.

Assuming that the dispersion relation $\omega = \sqrt{\omega_0^2 + k^2v^2}$ is satisfied, we obtain (after some transformations) an approximate relationship

$$\int_{-\omega_m}^{\omega_m} d\omega \int_{-k_m}^{k_m} k^4 g_X(\omega, k)dk = \left\{1 - v^4 G_a \int_{-\omega_m}^{\omega_m} d\omega \int_{-k_m}^{k_m} k^4 |K(\omega, k)|^2 (1 - p)\right\}^{-1} \quad (6)$$

$$\times \int_{-\omega_m}^{\omega_m} d\omega \int_{-k_m}^{k_m} k^4 |K(\omega, k)|^2 (1 - p) g_F(\omega, k)dk,$$

where $p = (1/2)k^2V^2\sigma_a^2[K(\omega, k) + K^*(\omega, k)]^{-1}$. Note that the value in braces of Eq. (6) is non-negative (since $g_X(\omega, k)$ cannot be negative) and is virtually equal to $1 - \omega_m\tau\sigma_a^2$. Therefore, for the pumping with the dispersion σ_a^2 such that

$$\sigma_a^2 = (\omega_m\tau)^{-1}, \quad (7)$$

the losses are almost completely compensated by the pumping and the integral $\int_{-\omega_m}^{\omega_m} d\omega \int_{-k_m}^{k_m} k^4 g_\xi(\omega, k)dk$ in (6) becomes very large. This integral determines dispersion of the random function $\partial^2X(x, t)/\partial x^2$ describing the interparticle elastic forces. Thus, relation (7) implies a sharp chaotization of the above forces and can be considered as the equation of the first-order phase transition. Since the dispersion σ_a^2 of the thermal pumping increases with the temperature, Eq. (7) in fact determines the temperature of the phase transition.

Let us estimate the σ_a^2 value. Since the quantity $\tilde{a}$ in Eq. (2) is related to the thermal field gradient, $\tilde{a} = -(m\omega^2)^{-1}(\partial F(t, x)/\partial x)$, the value of $\tilde{a}$ is on the order of $F(t, x)/m\omega^2 r_0$:

$$\tilde{a} = O(F(t, x)/m\omega^2 r_0).$$

At the same time, the $m\omega^2$ value near the frequency ω_0 is on the order of the coefficient of elasticity of intermolecular bonds

$$m\omega^2 r_0 = O(F_e),$$

where F_e is the intermolecular force. Taking into account that $F(t, x) = O(F_eX/r_0)$, we obtain

$$\tilde{a} = O(F_eX/r_0)/F_e) = O(X/r_0).$$

Thus, the dispersion of the thermal pumping can be estimated by the order of magnitude as

$$\sigma_a^2 = O(\sigma_X^2/r_0^2) = O(v^2/\omega^2 r_0^2) = O(kT/m\omega^2 r_0^2) = O(kT/\beta r_0^2) = O(kT/mv^2).$$

Therefore, the phase transition condition (7) reduces to

$$kT_0 > mv^2/2Q_m, \quad (8)$$

where T_0 is the phase transition temperature and $Q_m = \omega_m\tau/2$ is the quality factor. The estimates of Q by formula (8) obtained for the melting of substances such as Al, Fe, Pb, Sn, and ice (H_2O) show that Q_m values are

on the order of several tens to several hundred units, which seems to be quite realistic.

The above model of the condensed medium, owing to the simplifications employed, is valid for both solids and liquids. Therefore, relationship (7) describes both melting and boiling processes. The estimates obtained by formula (8) for the process of boiling in the same series of substances show that the Q_m values in liquids are about ten times lower than in solids.

In accordance with the fluctuation-dissipation theorem, the aforementioned pumping-induced decrease in the total losses will lead to a decrease n the internal field strength and, hence, to a decrease in the dispersion σ_a^2. Therefore, the phase transition caused by the parametric coupling in a thermodynamically equilibrium system of particles is impossible. In order to provide for the phase transition, the energy (phase transition heat) has to be supplied from outside. The amount of this energy and the other energy parameters of the first-order phase transition can be estimated, provided that the higher (nonlinear) terms in the expansion (3) are taken into account and that Eq. (4) is more exactly solved.

Thus, the above considerations show that relatively small fluctuations in shape of the interparticle interaction potential related to the parametric coupling between the particle oscillations and the thermal field may lead to a decrease in the energy losses and eventually to the phase transition. Therefore, the phase transition is related to the mutual influence of phonons; that is, it results from multiphonon processes.

REFERENCES

1. G. A. Martynov, Usp. Fiz. Nauk **169** (6), 595 (1999).
2. L. D. Landau and E. M. Lifshitz, *Course of Theoretical Physics*, Vol. 8: *Electrodynamics of Continuous Media* (Nauka, Moscow, 1992; Pergamon, New York, 1984).
3. S. M. Rytov, *Introduction to Statistical Radiophysics* (Nauka, Moscow, 1966).
4. F. J. Dyson, in *Statistical Physics, Phase Transitions and Superfluidity*, Ed. by M. Chrétien *et al.* (Gordon and Breach, New York, 1968), Vols. 1, 2; E. W. Montroll, in *Statistical Physics, Phase Transitions and Superfluidity*, Ed. by M. Chrétien *et al.* (Gordon and Breach, New York, 1968), Vols. 1, 2; M. Kac, in *Statistical Physics, Phase Transitions and Superfluidity*, Ed. by M. Chrétien *et al.* (Gordon and Breach, New York, 1968), Vols. 1, 2; M. E. Fisher, in *Proceedings of the Enrico Fermi Summer School on Critical Phenomena, Villa Monastero, 1970.*
5. M. M. Sushchinsky, *Raman Spectra of Molecules and Crystals* (Nauka, Moscow, 1969; Israel Program for Scientific Translations, Jerusalem, 1973).

Translated by P. Pozdeev

Technical Physics Letters, Vol. 28, No. 4, 2002, pp. 289–291. Translated from Pis'ma v Zhurnal Tekhnicheskoĭ Fiziki, Vol. 28, No. 7, 2002, pp. 57–61.

Energy Efficiency of the Vibration-Accelerated Liquid Mass Transfer in a Channel

G. A. Lyakhov and I. V. Shugan

Scientific Center for Wave Research, Institute of General Physics, Russian Academy of Sciences, Moscow, Russia

e-mail: wrc@kapella.gpi.ru

Received November 6, 2001

Abstract—The method of vibration-enhanced liquid mass transfer in a channel with oscillating walls is described. Homogeneous (over the channel length) transverse oscillations of the walls can provide for a significant increase in the mass transfer rate. The energy efficiency of the proposed vibrational technology is calculated. © *2002 MAIK "Nauka/Interperiodica".*

The problem of increasing the rate of mass transfer in a channel is important for many natural systems, including physiological cycles of biological organisms and processes in natural oil- and water-saturated porous media [1]. However, controlled variation of the structural characteristics of these systems, such as the geometry parameters or external pressure differences, encounters considerable technological difficulties, while some technologies are inapplicable at all. An effective alternative method of accelerating the mass transfer is based on using transverse vibrations of the channel walls [2]. This technique provides for an increase in the rate of liquid flow without changing properties of the medium. In some natural (in particular, physiological) media, this approach can be the only means of significantly increasing the transmission capacity of a channel for certain purposes.

Previously [3], a model was proposed for description of the flow of a viscous liquid in a channel with elastic walls performing harmonic oscillations. An analysis of the wave motions of the general type in a two-phase system revealed the regime of nonpropagating oscillations of the channel walls. The study was performed under the assumption of a small amplitude ε of the wall oscillations: $\varepsilon/H_0 \ll 1$, where H_0 is the unperturbed channel halfwidth.

The purpose of this study was to provide for a significant increase of applicability of the model proposed in [3] to calculate the mass transfer characteristics for the flow regimes involving large modulation of the channel width $\varepsilon/H_0 \sim O(1)$ and to analyze the energy balance under such flow conditions.

Let us consider a plane channel with width $2H$ and length L (Fig. 1), through which a liquid is transferred under the action of a pressure difference ΔP. Averaged over the transverse cross section, the Navier–Stokes equations of motion of a viscous incompressible liquid include the law of mass conservation,

$$\frac{\partial}{\partial X}\left(\int_{-H}^{H} U dY\right) + \frac{\partial}{\partial T} H = 0, \tag{1}$$

where U is the liquid flow velocity component along the X axis and T is the current time, and the law of momentum conservation,

$$\frac{\partial}{\partial T}\left(\int_{-H}^{H} U dY\right) + \frac{\partial}{\partial X}\left(\int_{-H}^{H} U^2 dY\right) = -\frac{H}{\rho}\frac{\partial P}{\partial X} + \nu\left(\frac{\partial}{\partial Y} U\right)\Big|_{Y=H}, \tag{2}$$

where ν and ρ are the kinematic viscosity and density of the liquid and P is the pressure.

A steady-state flow of the viscous incompressible liquid in the channel with immobile walls is described by the Poiseuille solution

$$U = -\frac{P_X}{2\nu\rho}(H^2 - Y^2), \quad V = 0, \tag{3}$$

where V is the transverse velocity component of the

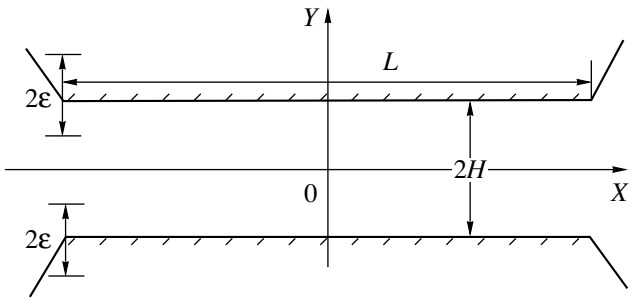

Fig. 1. A schematic diagram of the channel: L, length; H, halfwidth; ε, wall oscillation amplitude.

1063-7850/02/2804-0289$22.00 © 2002 MAIK "Nauka/Interperiodica"

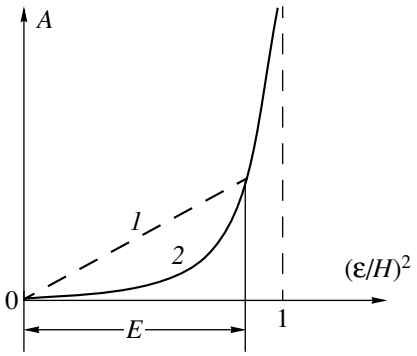

Fig. 2. A comparison between energy consumption A due to increasing pressure difference (line *1*) and channel wall oscillations (curve *2*). Interval E corresponds to the domain of effective application of the vibrational technology.

flow. The rate of liquid mass transfer is

$$Q_0 = \int_{-H}^{H} U dY = -\frac{H^3 \Delta P}{3\nu\rho L}, \tag{4}$$

where ΔP is the pressure difference between the channel entrance and exit.

Let us study a nonstationary case in which the channel walls perform symmetric (relative to the horizontal axis) vertical oscillations with amplitude ε and frequency ω:

$$H = H_0 + \varepsilon \sin(\omega T). \tag{5}$$

The flow will be described based on the averaged equations of motion (1) and (2), with the instantaneous velocity distribution in the channel cross section approximated by formula (3). Variation of the pressure P along the channel length is calculated using a natural boundary condition at the channel ends: $\Delta P = P(X = L/2) - P(X = -L/2)$.

The results of calculations show that the time-average mass transfer rate Q_1 is maximum for small Reynolds numbers $\mathrm{Re} = H_0^2 \omega/\nu \le 1$ [4] and increases with the amplitude of wall oscillations according to the formula

$$Q_1 = Q_0 \left\{ 1 + \frac{3}{2} (\varepsilon/H_0)^2 \right\}. \tag{6}$$

The maximum increase in the flow rate is provided by a regime of the compete periodic "squeezing out" of the liquid for $\varepsilon = H_0$, whereby the mass transfer rate at a given pressure drop ΔP increases by a factor of 2.5.

In some cases, it is possible to increase the mass transfer rate by changing the pressure difference and/or the geometric characteristics of the system. Acceleration of the mass transfer through the channel at the expense of increase in the pressure difference between channel ends leads to an additional energy consumption compensating for the work A of viscous forces during the liquid flow:

$$A = \left(-\int_{-H}^{H} PU dY \right)_{X = L/2} + \left(\int_{-H}^{H} PU dY \right)_{X = -L/2} = \mu \int_{-L/2}^{L/2} dX \int_{-H}^{H} U_Y^2 dY, \tag{7}$$

where μ is the dynamic viscosity coefficient. As the mass transfer rate increases from Q_0 to Q_1 due to an increase in the ΔP value, the additional energy consumption is

$$\Delta A = \frac{3\mu L}{H^3} (Q_1^2 - Q_0^2). \tag{8}$$

Evaluation of the time-average energy consumption A_V for the vibration-enhanced mass transfer yields

$$A_V = \left(-\int_{-H}^{H} PU dY \right)_{X = L/2} + \left(\int_{-H}^{H} PU dY \right)_{X = -L/2} + \frac{1}{2\pi} \int_0^{2\pi} dT \int_{-L/2}^{L/2} H_T P dX. \tag{9}$$

Acceleration of the mass transfer related to the vibration mechanism leads to the following additional energy consumption:

$$\Delta A_V = \frac{3\mu L}{H^3} Q_1 Q_0 + \frac{\mu}{4} \left(\frac{L}{H} \right)^3 \varepsilon^2 \omega^2 \frac{1}{(1 - (\varepsilon/H)^2)^{3/2}}. \tag{10}$$

A key point in evaluating the energy efficiency of the proposed method is a comparison of the energy consumption for the vibration-enhanced mass transfer to the additional energy spent in the case of increasing pressure difference. The efficiency of the vibrational technology is determined by two factors. First, by the threshold value of the dimensionless parameter α:

$$\alpha = 18 \left(\frac{Q_0}{H_0 L \omega} \right)^2 > 1. \tag{11}$$

Second, by a limitation posed on the relative amplitude ε/H_0 for which the vibrational technology is

energetically favorable:

$$\alpha\left(1+\frac{3}{2}(\varepsilon/H_0)^2\right) > \frac{1}{\{1-(\varepsilon/H_0)^2\}^{3/2}}. \qquad (12)$$

Dependence of the consumed energy on the relative amplitude of oscillations of the channel walls is depicted in Fig. 2. This figure indicates the domain of effective application of the proposed vibrational method.

Thus, application of the proposed vibrational technology for acceleration of the liquid mass transfer is energetically favorable for sufficiently fast flow regimes, whereby the flow rate Q_0 exceeds the value $LH\omega$ of the flow rate corresponding to the transfer of unperturbed channel volume per unit time.

REFERENCES

1. M. Y. Jaffrin and A. H. Shapiro, Annu. Rev. Fluid Mech. **3**, 63 (1971).
2. M. S. Longuet-Higgins, J. Fluid Mech. **137**, 393 (1983).
3. I. Shugan, Phys. Vib. **7** (2), 107 (1999).
4. I. Shugan and N. Smirnov, Phys. Vib. **9** (2), 83 (2001).

Translated by P. Pozdeev

Technical Physics Letters, Vol. 28, No. 4, 2002, pp. 292–294. Translated from Pis'ma v Zhurnal Tekhnicheskoĭ Fiziki, Vol. 28, No. 7, 2002, pp. 62–67.

Diffusion Healing of the Radiation Defects During Ion Bombardment of a Ge(111) Crystal Face

N. N. Gorobeĭ, V. E. Korsukov*, A. S. Luk'yanenko, R. R. Nazarov, and B. A. Obidov

Ioffe Physicotechnical Institute, Russian Academy of Sciences, St. Petersburg, 194021 Russia

** e-mail: Vjacheslav.Korsukov@pop.ioffe.rssi.ru*

Received December 6, 2001

Abstract—The kinetics of ion-bombardment-induced damage and thermal annealing of a Ge(111) single crystal surface is studied by electron energy loss spectroscopy. The activation energy for the diffusion healing of radiation defects formed on the Ge(111) surface bombarded with 3-keV Ar^+ ions is estimated at $Q = 0.3$ eV. *© 2002 MAIK "Nauka/Interperiodica".*

Diffusion is a significant factor in the phenomenon of healing of surface damage, which serves as a basis for experimental determination of the diffusion coefficient [1]. Also possible is a reverse process of the surface relief formation, whereby the surface occurs in a stressed state, for example, in the course of heteroepitaxial growth [2] or under direct mechanical loading [3]. The efficiency of the diffusion factor is determined by the presence of a diffusion "material"—relatively weakly bound surface atoms (adatoms)—and by their mobilities. During epitaxy, the source of adatoms is represented by a molecular beam; on a deformed surface, the diffusing atoms are supplied from edges of the relief features occurring in a significantly overstressed state [4].

The transport of adatoms over the surface is essentially a temperature-activated random-walk process, the parameters of which also determine the efficiency of the diffusion factor. A convenient means of determining the diffusion mobility of adatoms is offered by observation of the kinetics of healing of the radiation defects formed on a surface bombarded with ions. Here, the same ion bombardment process presents a source of the diffusion material. The purpose of our work was to study the kinetics of the ion-bombardment-induced surface damage and thermal annealing on a Ge(111) crystal face bombarded with Ar^+ ions. The surface was analyzed by the spectroscopy of electron energy losses on plasmons [5].

The initial Ge(111)–(2×8) surface was prepared by multiply repeated cycles of ion bombardment followed by thermal annealing. The crystal surface structure and composition was monitored by low-energy electron diffraction (LEED) and Auger electron spectroscopy (AES). The sample surface was considered as prepared when no peaks of impurity atoms (primarily C and O) were observed in the AES spectra and the 2×8 superstructure was clearly manifested in the LEED patterns. In the course of our experiments, the sample surface was bombarded at various energies $E_i = 0.2$–3 keV and currents $I_i = 0$–100 nA of the primary Ar^+ ion beam. The area of a surface region scanned with the ion beam was 1 cm^2. The primary ion beam was incident on the sample surface at an angle of 60° relative to the normal. As is known, the surface irradiated at such relatively large angles remains virtually smooth in the course of ion bombardment [6]. The effects of ion bombardment and thermal annealing to various temperatures were studied by measuring the energy positions of plasmon peaks in the electron energy loss spectra (EELS).

Figure 1 shows variation of the energy shifts of the bulk and surface plasmon peaks in the course of a complete ion bombardment–thermal annealing cycle. Beginning with an initial state (point I) and gaining a significant irradiation dose at room temperature, the

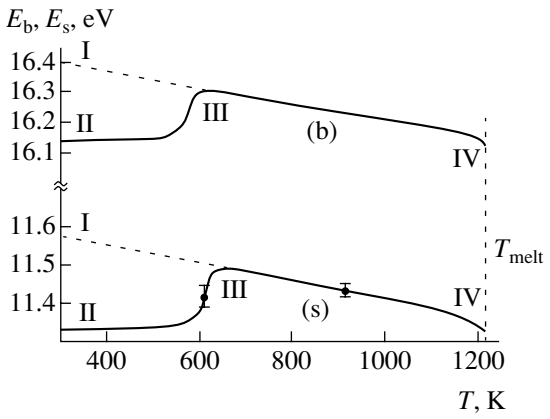

Fig. 1. Energy shifts of the (b) bulk and (s) surface plasmon peaks in the EELS of a Ge(111) crystal surface in the course of a complete ion bombardment–thermal annealing cycle.

1063-7850/02/2804-0292$22.00 © 2002 MAIK "Nauka/Interperiodica"

surface arrives at the state II. At this point, the ion gun is switched off and the sample heater is turned on. A slow increase in the sample temperature up to 550 K does not bring about significant changes in EELS; however, the peak positions exhibit a jumplike change at point III. We believe that this point features a phase transition of the disorder–order type in a sufficiently thick surface layer (not less than 3 nm, which corresponds to the bulk plasmon localization depth). It should be noted that the ideal Ge(111)–(2 × 8) surface exhibits a reverse (order–disorder) phase transition [7], but this transformation involves a less thick surface layer (on the order of 0.5 nm). Further heating of the sample up to the melting temperature (point IV) is accompanied by a monotonic decrease in the energy of plasmon peaks in EELS, which is apparently related to the thermal expansion effect. Finally, cooling of the sample leads to a smooth linear restoration of the initial state (point I).

Figure 2 shows a time variation (beginning with the moment of the ion bombardment onset) of the surface plasmon peak energy observed at various sample temperatures in the above indicated interval. As can be seen, the plasmon energy shift exhibits saturation on a level depending on the temperature. The strong temperature dependence of this kinetic can be explained only by a contribution due to the surface healing factor possessing a thermal activation character. Below we will estimate the activation energy within the framework of a simple model taking into account the balance between radiation damage and diffusion healing.

The surface plasmon energy is related to the electron density n_s (in Ge, the density of valence electrons) by the Ritchie–Langmuir relationship [8]

$$E_s = \frac{\hbar}{\sqrt{2}}\left(\frac{4\pi n e^2}{m}\right)^{1/2}. \quad (1)$$

According to this, small variations of the electron density and surface plasmon energy obey the linear relation

$$\frac{\Delta n_s}{n_s} = 2\frac{\Delta E_s}{E_s}. \quad (2)$$

Let Δn_m be the maximum decrease in the density of surface atoms within a certain region, related to a single radiation defect (by our estimates, this region has an area on the order of 1 × 1 nm for E_i = 34 keV). Here, a part of atoms is removed from the target surface, while another part remains in a weakly bound state forming a diffusion material necessary for the surface healing. We believe that the radiation damage is not a temperature-activated process. The reverse process of healing of the radiation defect is described by a simple

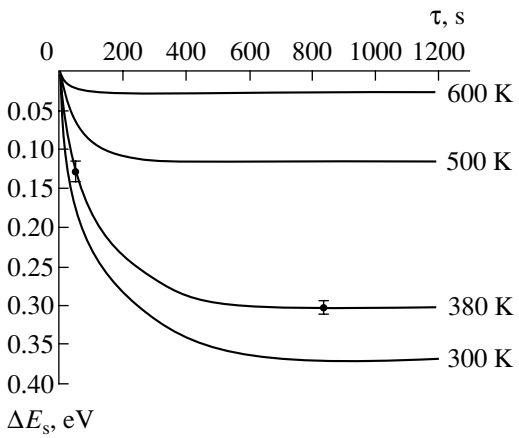

Fig. 2. Time variation of the surface plasmon peak shift in the EELS of a Ge(111) crystal surface bombarded with Ar^+ ions (E_i = 3 keV, I_i = 30 nA) at various temperatures.

law with a single time parameter τ determining the process rate:

$$\Delta n_s = \Delta n_m \exp\left(-\frac{t}{\tau}\right). \quad (3)$$

Since the healing process is diffusion controlled, the time parameter depends on the temperature as follows:

$$\tau = \tau_0 \exp\left(\frac{Q}{kT}\right).$$

Let us determine the activation energy Q by considering the balance of two aforementioned competing processes in a stationary regime at $t \longrightarrow \infty$. In the approximation of small ion current on–off ratio κ_0 (calculated for one defect), the asymptotic surface density change is given by the formula

$$\Delta n_\infty = \Delta n_m\left(1 - \frac{\kappa_0}{\tau}\right). \quad (4)$$

Comparing this expression to the experimental plasmon energy shifts ΔE_∞ observed at various temperatures (Fig. 2), we obtain Q = 0.3 eV. It is also interesting to compare this value to the activation barrier for the surface self-diffusion on the Ge(111)–(2 × 8) face: Q_0 = 1 eV [9]. The latter value is somewhat higher because this self-diffusion is limited by the temperature-activated process of adatom–vacancy pair production. Thus, a low activation barrier for the diffusion of adatoms on the ion-bombarded Ge(111) surface accounts for the effective healing of radiation defects formed in the course of ion bombardment of the crystal.

Acknowledgments. The authors are grateful to V.A. Zakrevskiĭ for fruitful discussions.

This study was supported by the Russian Foundation for Basic Research, project nos. 99-02-18287 and 2000-00-00482.

REFERENCES

1. Ya. E. Geguzin, *Surface Diffusion and Spreading* (Nauka, Moscow, 1969), p. 11.
2. J. Tersoff and F. LeGoues, Phys. Rev. Lett. **72** (23), 3570 (1994).
3. S. N. Zhurkov, V. E. Korsukov, A. S. Luk'yanenko, *et al.*, Pis'ma Zh. Éksp. Teor. Fiz. **51** (6), 324 (1990) [JETP Lett. **51**, 370 (1990)].
4. N. N. Gorobeĭ, S. A. Knyazev, V. E. Korsukov, *et al.*, Pis'ma Zh. Tekh. Fiz. **28** (1), 54 (2002) [Tech. Phys. Lett. **28**, 23 (2002)].
5. V. E. Korsukov, A. S. Luk'yanenko, and V. N. Svetlov, Poverkhnost, No. 11, 28 (1983).
6. J. Matsura, H. Shichi, and Y. Matsui, J. Vac. Sci. Technol. A **12** (5), 2641 (1994).
7. R. M. Feenstra, A. G. Slavin, G. A. Held, *et al.*, Phys. Rev. Lett. **66** (25), 3257 (1991).
8. H. Raether, Springer Tracts Mod. Phys. **38**, 88 (1965).
9. S. M. Repninskiĭ, *Introduction to the Chemical Physics of Surfaces* (Nauka, Novosibirsk, 1993).

Translated by P. Pozdeev

Technical Physics Letters, Vol. 28, No. 4, 2002, pp. 295–297. Translated from Pis'ma v Zhurnal Tekhnicheskoĭ Fiziki, Vol. 28, No. 7, 2002, pp. 68–72.

The Initial Stage of the Gallium Selenide–Gallium Arsenide Structure Formation by Heterovalent Substitution of Selenium for Arsenic

V. F. Antyushin, A. V. Budanov, E. A. Tatokhin, and Ya. A. Boldyreva

Voronezh State Technological Academy, Voronezh, 394017 Russia

Received November 13, 2001

Abstract—The initial stage of Ga_2Se_3–GaAs heterostructure formation by heterovalent substitution of selenium for arsenic in the solid state was studied by methods of scanning tunneling microscopy, electron microscopy, optical microscopy, and electron diffraction. © *2002 MAIK "Nauka/Interperiodica".*

The method of heterovalent substitution of selenium for arsenic in GaAs with the formation of a single-crystalline gallium selenide was proposed [1] for the obtaining of insulating coatings on the surface of gallium arsenide. The efficiency of electrical passivation and physical perfection of the interface are determined to a considerable extent by dimensions of the transition layer and by the scale of boundary microinhomogeneities in the resulting Ga_2Se_3–GaAs heterostructure. In order to determine these parameters, we have studied the initial stage of Ga_2Se_3 film growth in this heterostructure; this stage controls the structure of the boundary layer.

The Ga_2Se_3–GaAs heterostructures were obtained on the surface of ⟨100⟩ oriented GaAs substrates subjected to thermal annealing in selenium vapors filling a quasi-closed volume with hot walls [2, 3]. The process was performed at a substrate temperature T_l varied in the interval from 600 to 750 K and a selenium vapor pressure of ~2 Pa.

In order to provide conditions for the heterovalent substitution reaction, it is necessary to form As vacancies on the GaAs surface or in the near-surface layer. The vacancies form when As atoms leave the crystal surface and escape into vacuum as a result of substrate heating. Selenium atoms chemisorb on the As vacancies and form stable bonds with gallium. The solid-state heterovalent substitution reaction can be described by the following equation:

$$3GaAs + 3Se \longrightarrow Ga_2Se_3 + Ga\uparrow + 3As\uparrow. \qquad (1)$$

The formation of one structural unit of Ga_2Se_3 is accompanied by liberation of one Ga atom, which freely diffuses over stoichiometric vacancies in gallium arsenide lattice toward the surface and interacts with selenium. In a GaAs crystal, one-third of the cationic sublattice sites are vacant [4]; therefore, the atomic diffusion most probably proceeds via stoichiometric cationic vacancies. This implies that the film of gallium selenide grows simultaneously in the two opposite directions, with one layer of unit thickness formed on the inner interface (inward growth) corresponding to a half-layer formed on the outer surface (outward growth). The concentration of selenium atoms in the reaction zone is controlled by the metal vapor pressure at the substrate surface. The As vacancies are most probably formed at microinhomogeneities of the substrate surface, because these sites contain a maximum number of stressed bonds between Ga and As atoms.

The micrographs obtained with the aid of a scanning tunneling microscope (STM) from the surface of Ga_2Se_3–GaAs heterostructures formed at T_l = 600 K for t = 300 s show that the formation of gallium selenide begins at the vertices of the surface microrelief (Fig. 1). The characteristic size of microinhomogeneities in the growing layer ranges within 10.0 to 15.0 nm.

The patterns of electron diffraction from the structures formed at T_l = 700 K for t = 600 s indicate that the film grows in the ⟨110⟩ direction. An analysis of the electron micrographs showed the presence of ellipsoidal nuclei of gallium selenide, the dimensions of which fall within 45 to 60 nm.

The optical reflection spectra, measured in a range of wavelengths λ from 650 to 500 nm for the heterostructures grown under various conditions, exhibit a Rayleigh character. The energy reflection coefficient as a function of wavelength can be described by the relationship $R = D \cdot 1/\lambda^4 + G$, where D is the Rayleigh scattering coefficient and G is the mirror reflection component. The D values determined from the slope of the R versus $1/\lambda^4$ plots are listed in the table. As can be seen from these data, the initial stage of the GaAs treatment in selenium vapors leads to an increase in the D value as compared to that for the initial substrate surface. This is indicative of an increase in the concentration of surface scattering centers. An increase in the substrate temperature and the duration of treatment in selenium

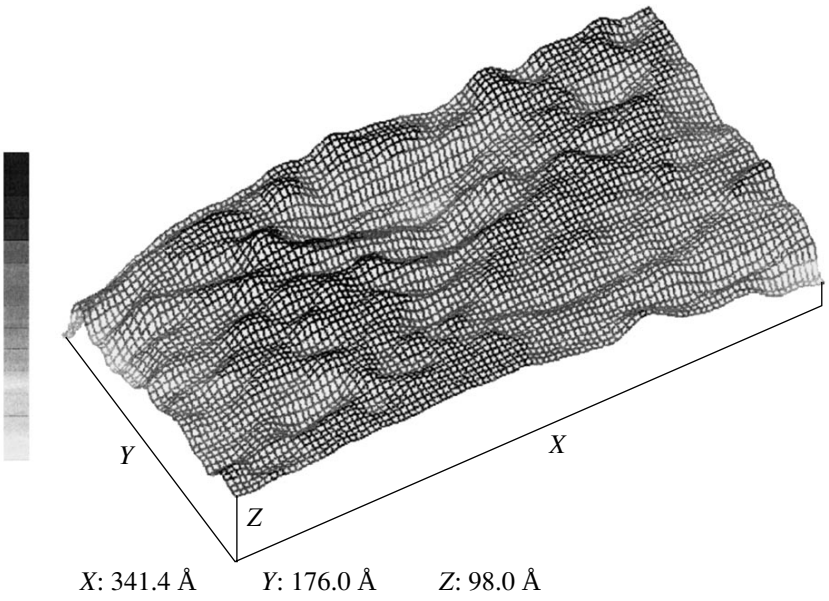

Fig. 1. STM image of a GaAs surface treated with selenium vapors (T_l = 600 K, p = 2 Pa, t = 300 s).

vapors leads to a decrease in the intensity of Rayleigh scattering, which is explained by coalescence of the growing nuclei.

An analysis of data on the enthalpy of formation of gallium selenide and arsenide [5] shows that the reaction under consideration is exothermal. Assuming that the reaction zone has an area of 1 cm^2 and a depth of 1 nm, the heat evolved as a result of the heterovalent substitution is $Q = 9.279 \times 10^{-4}$ J. Using the values of heat capacity (c = 22.961 J/(mol K)), density (ρ = 5.317×10^3 kg/m^3), and thermal conductivity (χ = 155.03 J/(m s K)) of GaAs [5], we can estimate the length L over which a temperature increment would spread for the time interval t by the following formula:

$$L = \sqrt{\frac{\chi}{c\rho}t}. \qquad (2)$$

The numerical estimates show that the substrate can heat for t = 1 s to a depth of $L \sim 0.014$ m. The substrate thickness in our experiments being $L \sim 250$ μm, we can use formula (2) to evaluate the time of substrate heating: $t \approx 3.1 \times 10^{-4}$ s. Thus, the liberated energy is removed from the reaction zone and cannot provide for the production of additional As vacancies in the near-surface layer of GaAs. Therefore, the heterovalent substitution reaction proceeds at the expense of heat supplied to the substrate from an external source and does not exhibit the character of a combustion process.

In the simplest case, assuming the process to be isothermal, the initial stage of the heterovalent substitution reaction can be described by a differential equation

$$\frac{dU_s}{dt} = \alpha_s p(1 - U_s), \qquad (3)$$

with the following solution:

$$U_s = 1 - \exp\left(-\int_0^\tau \alpha p\, dt\right), \qquad (4)$$

where U_s is the part of the substrate surface covered with Ga_2Se_3 ($1 - U_s$ is the uncovered surface fraction), α_s is a phenomenological reaction rate constant, and p is the selenium vapor pressure at the substrate surface.

The plot of $U_s(t)$ calculated for p = 2 Pa and α_s = 0.0023 (Fig. 2) shows that 70% of the GaAs surface is covered with gallium selenide for the time t = 300 s,

The values of the Rayleigh scattering coefficient D for a growing Ga_2Se_3 film determined from the optical reflectance measurements

Sample treatment conditions	$D \times 10^{-27}$, m^4
Initial GaAs substrate	8
T_l = 600 K; t = 300 s	20
T_l = 600 K; t = 600 s	10
T_l = 700 K; t = 300 s	10
T_l = 700 K; t = 600 s	8

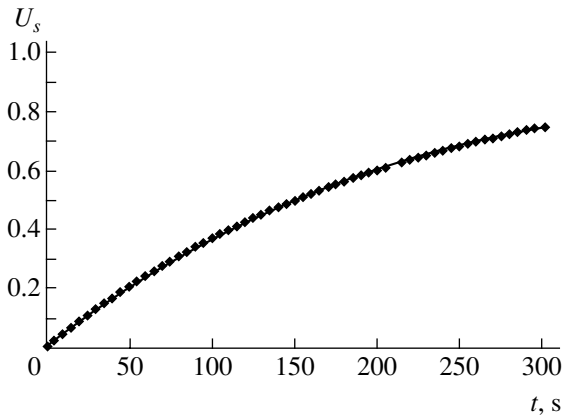

Fig. 2. A plot of the GaAs surface fraction coated with gallium selenide versus time of substrate exposure to selenium vapors (T_l = 700 K, $p \approx 2$ Pa).

which agrees with the data obtained from microscopic images of the sample surface.

Thus, the growth of a gallium selenide film on the GaAs surface proceeds via the nucleation stage, in which the surface microinhomogeneity size and the transition layer thickness are on the order of 10.0–15.0 nm.

REFERENCES

1. B. I. Sysoev, V. F. Antyushin, V. D. Strygin, and V. N. Morgunov, Zh. Tekh. Fiz. **56** (5), 913 (1986) [Sov. Phys. Tech. Phys. **31**, 554 (1986)].
2. Yu. Z. Bubnov, M. S. Lur'e, F. G. Staros, and G. A. Filaretov, *Vacuum Film Deposition in Quasi-Closed Volume* (Sov. Radio, Moscow, 1975).
3. B. I. Sysoev, V. D. Strygin, E. I. Chursina, *et al.*, Neorg. Mater. **27** (8), 1583 (1991).
4. N. A. Goryunova, *Diamond-Like Compound Semiconductors* (Sov. Radio, Moscow, 1968).
5. *Physicochemical Properties of Semiconductor Materials: A Handbook* (Nauka, Moscow, 1979), p. 60.

Translated by P. Pozdeev

Technical Physics Letters, Vol. 28, No. 4, 2002, pp. 298–299. Translated from Pis'ma v Zhurnal Tekhnicheskoĭ Fiziki, Vol. 28, No. 7, 2002, pp. 73–77.

Study of the Lithium Cluster Breakage Kinetics in Germanium

V. V. Svetukhin and P. A. Il'in

Ul'yanovsk State University, Ul'yanovsk, Russia

e-mail: slava@sv.uven.ru

Received December 10, 2001

Abstract—The lithium cluster breakage in germanium obeys an exponential kinetics with an activation energy for the particle detachment from cluster equal to 0.31 ± 0.05 eV. © *2002 MAIK "Nauka/Interperiodica".*

The small atomic radius of lithium accounts for the high diffusion mobility of these atoms in the crystal lattice of germanium. For this reason, a supersaturated solid solution of Li in Ge exhibits decay at relatively low temperatures. While the kinetics of lithium cluster formation in germanium was studied in sufficient detail (see, e.g., [1, 2]), no data are available on the cluster breakage kinetics. It should be noted that, to our knowledge, investigations of the cluster breakage in other systems have not been conducted either.

We have studied gallium-doped germanium single crystals used for the fabrication of Ge(Li) detectors. The material was characterized by a dopant concentration of $(1–1.6) \times 10^{14}$ cm^{-3}, a resistivity of 20–30 Ω cm, a dislocation density of $(1–4) \times 10^3$ cm^{-3}, and an interstitial oxygen impurity concentration of $(1–3) \times 10^{14}$ cm^{-3} [3]. The germanium plates (1–2 mm thick) were ground and chemically polished in a $3HNO_3 + HF$ mixture. The deposition of lithium, followed by a diffusion annealing at 450°C for 2 h, was performed in a modified vacuum setup of the UVR-2 type.

A sample was placed into an automated setup for the conductivity measurements by the four-point-probe technique. The concentration of lithium (N_{Li}) in the samples was determined with allowance for the electron mobility $\mu(\rho)$ depending on the resistivity ρ of lithium-doped germanium [4] and for the initial acceptor concentration N_{Ga}:

$$N_{\mathrm{Li}} = \frac{1}{q\mu(\rho)\rho} + N_{\mathrm{Ga}}, \quad (1)$$

where q is the electron charge. Determined in this way, the lithium concentration in as-prepared samples was $(7–8) \times 10^{17}$ cm^{-3}.

Because of a sufficiently high room-temperature mobility, lithium exhibits clusterization that can be monitored by measuring the changes in conductivity related to the transition of donor atoms into electrically inactive clusters. Using this method, we traced the kinetics of decay of a saturated solid solution of lithium in germanium. The experimental results showed that the decay involves two stages: fast (leading to a significant decrease in the lithium concentration within 2 to 3 days) and slow (continuing over about a week). Upon the complete solid solution decay, the concentration of electrically active lithium dropped to 1.5×10^{14} cm^{-3}.

Heating the samples leads to breakage of the lithium clusters. The cluster breakage kinetics was monitored by measuring the concentration of lithium not bound in the clusters (i.e., contributing to the conductivity). We have studied the cluster breakage kinetics in the samples heated to T = 70, 80, 90, and 100°C.

In order to exclude the contribution due to intrinsic carriers, each measurement of the lithium concentration was performed upon cooling the sample to room temperature. During the time required for cooling and measuring the sample (about 15 s), a relative change in the lithium concentration caused by atoms entering the clusters was below 1%.

An analysis of the experimental data showed that the observed kinetics is well described by the differential equation

$$\frac{dN_{\mathrm{Li}}}{dt} = -K(T)(N^0_{\mathrm{Li}} - N^E_{\mathrm{Li}}(T))\exp\{-K(T)t\}, \quad (2)$$

where $N^E_{\mathrm{Li}}(T)$ is the equilibrium concentration of lithium, N^0_{Li} is the lithium concentration before cluster breakage, and $K(T)$ is the kinetic coefficient.

Figure 1 shows the experimental data in comparison to the curve constructed by solving Eq. (2):

$$N_{\mathrm{Li}}(t) = N^E_{\mathrm{Li}}(T) + (N^0_{\mathrm{Li}} - N^E_{\mathrm{Li}}(T))\exp\{-K(T)t\}. \quad (3)$$

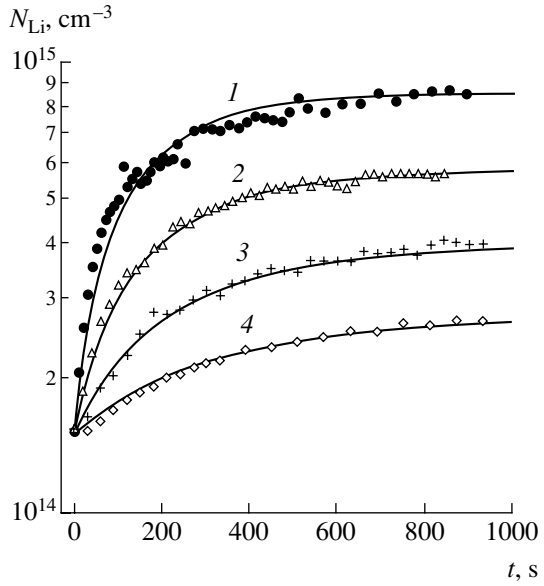

Fig. 1. Kinetics of the lithium concentration increase during the breakage of lithium clusters in a germanium crystal heated to T = (*1*) 100, (*2*) 90, (*3*) 80, and (*4*) 70°C. Points represent the experimental data; solid curves show the results of calculations by formula (3).

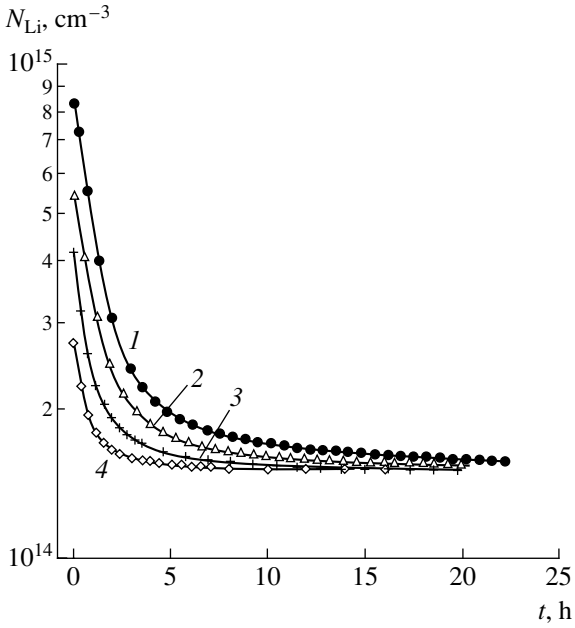

Fig. 2. Kinetics of the lithium concentration decrease during the formation of lithium clusters in a germanium crystal cooling to room temperature after being heated to T = (*1*) 100, (*2*) 90, (*3*) 80, and (*4*) 70°C. Points represent the experimental data; solid curves show the results of calculations by formula (3).

A comparison of the experimental curves to formula (3) leads to the following empirical relationships:

$$N_{Li}^{E}(T) = 10^{19}\exp(-0.35/kT), \quad \text{cm}^{-3}, \qquad (4)$$

$$K(T) = 2\times 10^{2}\exp(-0.31/kT), \quad \text{s}^{-1}. \qquad (5)$$

Note that the activation energy for the cluster breakage (0.31 ± 0.05 eV) is somewhat lower than the activation energy for lithium diffusion (by various data, 0.45–0.5 eV [2]).

After termination of the sample heating (which led to the breakage of clusters) and the establishing of room temperature, the samples are featuring the reverse process of cluster formation. During this process, the concentration of lithium decreases to an equilibrium room-temperature value (Fig. 2). It should be noted that this decay proceeds much faster than that in the as- prepared samples. This is probably related to the fact that clusters are incompletely decomposed on heating and the detached lithium atoms do not travel far from the clusters.

Acknowledgments. This study was supported by the Russian Foundation for Basic Research (project nos. 01-00209 and 01-00283), by the Ministry of Education (project no. E00-3.2-110), and by the Ministry of Atomic Energy of the Russian Federation.

REFERENCES

1. V. I. Fistul', *Decay of Supersaturated Semiconductor Solutions* (Metallurgiya, Moscow, 1977).
2. B. I. Boltaks, *Diffusion and Point Defects in Semiconductors* (Nauka, Leningrad, 1972).
3. R. Wichner, G. A. Armantrout, and T. G. Brown, IEEE Trans. Nucl. Sci. **NS-17**, 160 (1970).
4. L. A. Goncharov and N. G. Chavleĭshvili, Fiz. Tekh. Poluprovodn. (Leningrad) **7** (8), 308 (1973) [Sov. Phys. Semicond. **7**, 220 (1973)].

Translated by P. Pozdeev

Technical Physics Letters, Vol. 28, No. 4, 2002, pp. 300–302. Translated from Pis'ma v Zhurnal Tekhnicheskoĭ Fiziki, Vol. 28, No. 7, 2002, pp. 78–83.

Piezoelectric Fiber Optic Phase Modulator with a Reduced Level of Spurious Polarization Modulation

V. P. Gubin, V. G. Kovalenko, A. I. Sazonov, and N. I. Starostin

Fryazino Branch, Institute of Radio Engineering and Electronics, Russian Academy of Sciences, Fryazino, Moscow oblast, Russia

e-mail: http:\\fire.relarn.ru

Received November 9, 2001

Abstract—It is experimentally demonstrated that a tenfold decrease in the level of spurious polarization modulation can be achieved in a fiber optic phase modulator comprising two fiber sections featuring the polarization mode conversion, arranged on the same piezoelement. © *2002 MAIK "Nauka/Interperiodica".*

Fiber optic phase modulators (FPMs) are widely used in modulated-response interferometric transducers. In order to decrease the error of measurements, an FPM must ensure a low level of accompanying modulation, to which a maximum contribution is usually introduced by spurious polarization modulation (SPM). This factor was studied in much detail [1–6] for FPMs based on a piezoceramic element with a fiber coiled around. Methods suggested for the SPM suppression are mostly based on compensation schemes employing fiber polarization mode conversion [2–4, 6]. However, the problem of reducing the SPM level in FPMs has by no means been completely solved. Indeed, simple methods employing two identical piezoelectric fiber elements spaced by a mode converter [2, 3] are characterized by a rather low stability of the compensation, whereas more effective schemes (e.g., based on the Faraday reflector principle [4, 6]) are complicated and not studied in sufficient detail.

Here we report on the results of an experimental investigation of a piezoelectric FPM with SPM compensation achieved by using two fiber sections featuring mode conversion in a single piezoelement.

The idea of the proposed approach consists in using an anisotropic fiber composed of two sections wound around the same element and connected so as to provide for a 90° relative rotation of their birefringence axes. As a result, any modulation of the birefringence and mode coupling caused by modulated voltage in one fiber section (which is the main reason of SPM [4]) will be compensated by an analogous modulation of the opposite sense in the other fiber section.

The experiments were performed using a setup schematically depicted in Fig. 1. The system represents a fiber optic ring interferometer of the Sanjak type with an isotropic-fiber sensor loop and the Layot depolarizer in one arm of the circuit. An FPM [6] to be studied is connected into the optical scheme by welded joints. A harmonic modulation voltage U_m with a frequency of f_m = 42 kHz is applied to the piezoceramic element of the FPM. The radiation is produced by a superfluorescent source based on an erbium fiber with an average wavelength of 1.55 μm. The output radiation is detected by a photodiode, the output signal of which contains the voltage components U_1 and U_0 proportional to the first harmonic amplitude of the modulated light intensity and the average intensity level, respectively (these values are used to calculate the SPM characteristics). In order to decrease the error of measurements, the U_1 signal was detected using a phase-lock-in scheme, whereby the synchronous (U_{1s}) and a quadrature (U_{1q}) were measured and the first-harmonic signal was determined as $U_1^2 = U_{1s}^2 + U_{1q}^2$. Here, a synchronous tuning of the lock-in detector corresponds to maximum sensitivity of the interferometer with respect to rotation.

The FPM studied (Fig. 1) comprises a piezoceramic disk, 50 mm in diameter and 1.5 mm thick, bearing a

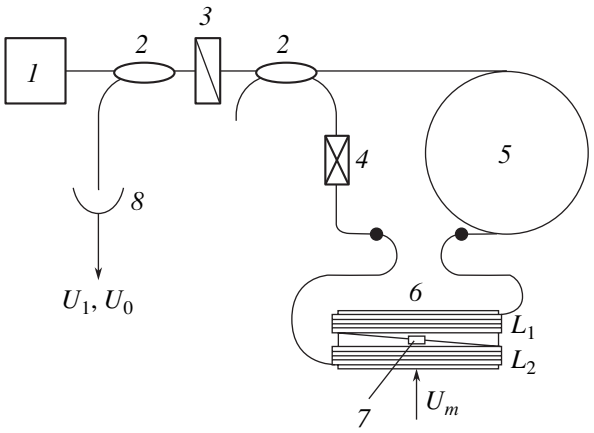

Fig. 1. A schematic diagram of the experimental setup: (*1*) radiation source; (*2*) decouplers; (*3*) polarizer; (*4*) depolarizer; (*5*) loop; (*6*) phase modulator; (*7*) welded joint; (*8*) photodetector.

1063-7850/02/2804-0300$22.00 © 2002 MAIK "Nauka/Interperiodica"

pressed aluminum ring. Wound around the ring with 50-g tension were two fiber sections with the lengths L_1 and L_2 cut from the same piece of fiber. We employed a fiber of the Panda type characterized by the polarization conservation parameter $h = 10^{-4}$ m^{-1}. Prior to winding, the sections were welded so as to provide for a 90° relative rotation of their birefringence axes (with an uncertainty of $\alpha \cong \pm 3°$). The edge turns in both sections were fixed with an epoxy glue.

A polarization modulation in the measuring interferometer is manifested by an output signal intensity modulation gained when the radiation travels through the polarizer. The SPM level was characterized by the ratio $\chi = U_{1\,\max}/U_0$ for a radiation phase deviation of $\varphi_{m0} = 1$ rad. Here, $U_{1\,\max}$ is the maximum value of the amplitude attained in a certain state of polarization at the FPM input [2, 3, 5]. Since the polarization state of the interferometer with elements made of an isotropic fiber strongly depends on the temperature, we employed the following method. The temperature of the optical elements was slowly varied in the interval from 20 to 50°C and the U_1 signal components were recorded. An example of such a record is presented in Fig. 2, where $U_{1\,\max} \cong 25$ μV ($U_0 = 950$ mV, $\varphi_{m0} \cong 1.5$ rad). A statistical analysis of the results of numerous experiments showed that the SPM maximum is revealed at a high probability. It should be noted that an error related to other effects (mode coupling in the loop fiber, spurious modulation of losses in the FPM, etc.) was also evaluated and has proved to be negligibly small. In addition, we made allowance for (subtracted) a signal component related to the rotation of Earth.

Deviation of the phase φ_{m0} was determined using the well-known relationship describing time variation of the output signal during rotation of the interferometer: $U_1(t) = U_0 J_1(2\varphi_m)\sin(2\Phi_s)\cos(2\pi f_m t)$, where $J_1(2\varphi_m)$ is the first-order Bessel function, Φ_s is the Sanjak phase-shift proportional to the angular velocity of the interferometer, and φ_m is the deviation of the difference phase of the opposite waves in the loop. The latter quantity is determined as $\varphi_m = \varphi_{m0}\sin(\pi f_m \tau)$, where $\tau = nL/c$, $L = 500$ m is the fiber length in the loop, $n = 1.44$ is the refractive index of the fiber, and c is the speed of light in vacuum. The interferometer sensitivity is maximum for $2\varphi_m = 1.84$, which was used for determining φ_{m0} at a given modulator fiber length.

Figure 3 shows a plot of the SPM level versus length L_2 of the second FPM section (for a fixed length $L_1 = 88$ cm of the first section). As can be seen from these data, the SPM level can be reduced by a factor of about ten against the value for a single-section unit, provided that the optimum length $L_{2\,opt}$ is used. Analogous curves were measured with the fiber in the second section twisted within ±(0.5–3) deg/cm. It was found that the SPM level depends but weakly on the fiber twist. Note

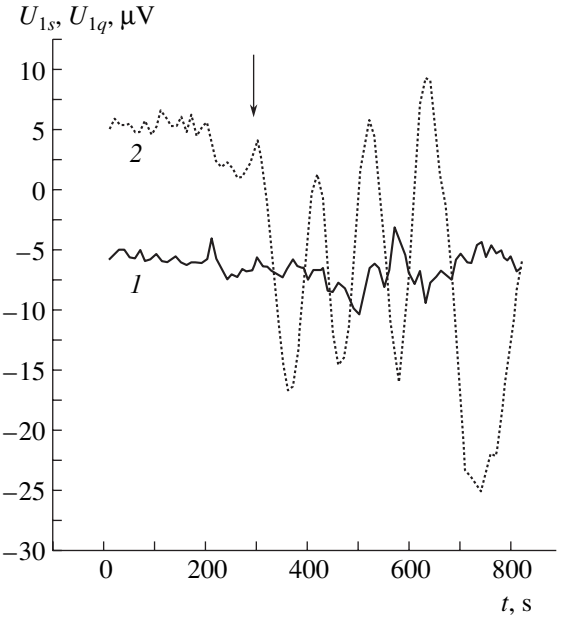

Fig. 2. Time variation of the (*1*) synchronous and (*2*) quadrature components of the interferometer output signal in the absence of rotation, measured on heating the phase modulator unit (the onset of heating is indicated by the arrow).

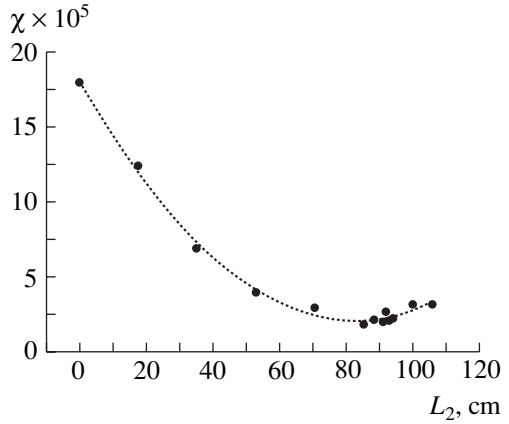

Fig. 3. The plot of SPM level versus fiber length in the second FPM section.

also a high level of stability in the degree of SPM reduction in the proposed FPM.

The degree of reduction in the SPM level achieved in this study is limited by several factors. In our opinion, the dominating role among these is played by uncertainty in the mode conversion related to the error of relative rotation α of the birefringence axes in the welded joint. Estimates made as described in [6] yield a reduction coefficient of $\sim\sin(2\alpha) \cong 0.1$, in agreement with our experiment.

Thus, we have experimentally demonstrated that a tenfold decrease in the level of spurious polarization modulation can be achieved in a fiber optic phase mod-

ulator comprising two fiber sections featuring the polarization mode conversion, wound around the same piezoelement.

Acknowledgments. The authors are grateful to E.N. Bazarov for support of this study and to É.I. Alekseev for fruitful discussions.

This study was supported by the Russian Foundation for Basic Research, project no. 00-02-17344.

REFERENCES

1. E. Kiesel, Proc. SPIE **838**, 129 (1987).
2. B. Szafraniec and J. Blake, J. Lightwave Technol. **12** (9), 1679 (1994).
3. D. G. Luke, R. McBridge, J. G. Burnett, *et al.*, Opt. Commun. **121**, 115 (1995).
4. É. I. Alekseev and E. N. Bazarov, Pis'ma Zh. Tekh. Fiz. **23** (15), 90 (1997) [Tech. Phys. Lett. **23**, 613 (1997)].
5. É. I. Alekseev, E. N. Bazarov, V. P. Gubin, *et al.*, Radiotekh. Élektron. (Moscow) **42** (9), 1150 (1997).
6. É. I. Alekseev, E. N. Bazarov, V. P. Gubin, *et al.*, Radiotekh. Élektron. (Moscow) **44** (1), 122 (1999).

Translated by P. Pozdeev

Technical Physics Letters, Vol. 28, No. 4, 2002, pp. 303–304. Translated from Pis'ma v Zhurnal Tekhnicheskoĭ Fiziki, Vol. 28, No. 7, 2002, pp. 84–88.

On the Theory of the Johann Focusing Spectrometer

T. Tchen

Moscow State Academy of Fine Chemical Technology, Moscow, Russia
e-mail: docent65@mtu-net.ru; ttchen@e-mail.ru

Received September 17, 2001

Abstract—The focusing of a spherical X-ray beam according to the Johann scheme is considered based on the dynamic theory of Bragg's diffraction in a thick crystal. With an allowance for the aberration of a diffracted beam, the beam intensity in the focal region can be described by one of the two analytical expressions, depending on the model selected for the crystal surface bending. The spectral characteristics of the Johann focusing spectrometer are considered in comparison to the existing theory of such spectrometers. © *2002 MAIK "Nauka/Interperiodica".*

A dynamic theory of the Johann focusing spectrometer [1] was developed in [2–4]. Later, Gabrielyan *et al.* [5] theoretically studied the Johann–Hamos spectrometer possessing generally the same characteristics as the original Johann spectrometer, but providing for an additional gain in transmission due to the vertical focusing effect. In the existing theory [2–5], the phases of the incident spherical wave and diffracted focused wave are expanded in a parabolic approximation, which is related to selecting the reflecting bent crystal surface in the form of a parabolic cylinder. This leads to an infinitely large value for the intensity of the focused wave. In [2–4], the nonphysical result was eliminated by performing integration within finite limits.

Below we will demonstrate that, by expanding the wave phase to within the terms $\sim x^3$ (with neglect of the reflecting surface bending, $z \approx 0$) or to within the terms $\sim x^4$ (for $z \approx x^2/2R_x$), we obtain two different formulas for the intensity distribution. Taking into account the third and higher degrees of the coordinate x ion the phase expansion implies an allowance for the geometric aberrations.

Let us consider two models of the crystal bending. In the first model, a weak bending of the crystal leaves the crystal surface flat: $z \approx 0$. In this case, the distance from the point of incidence of an arbitrary ray to the imaging point is

$$L_h(x) = L_{h(0)}(1 + x\sin\varphi_h/L_{h(0)} + x^2\cos^2\varphi_h/2L_{h(0)}^2 - x^3\sin\varphi_h\cos^2\varphi_h/2L_{h(0)}^3), \quad (1)$$

where $L_{h(0)}$ is the aberration-free distance from the crystal surface to the image. Note that formula (1) takes into account aberrations up to the third order.

With an allowance for the Huygens–Fresnel principles of X-ray diffraction and X-ray optics, the dynamic theory of Bragg's diffraction in a thick crystal developed in [2–6] yields the following expression for the diffracted wave intensity at the point ξ_p near the focus:

$$I_h(\xi_p) \sim \left| \left\{ \kappa^2 C\chi_{hr}\sigma_h \int_{-\infty}^{+\infty} d\check{y} R(\check{y})/(8\pi^{3/2}R_x^2\sin^2 2\theta_B) \right\} \times \int_{-\infty}^{+\infty} dx \exp\{ i\kappa[\xi_p x\cos\varphi_h/L_{h(0)} - \check{y}\sigma_h x/\kappa + \cos^2\varphi_h x^2/2L_{h(0)} - \cos\varphi_h x^2/2R_x - x^3\sin\varphi_h\cos^2\varphi_h/2L_{h(0)}^2]\} \right|^2. \quad (2)$$

Here, $\kappa = 2\pi/\lambda$, λ is the wavelength of the incident radiation, C is the polarization factor, χ_{hr} is the Fourier component of the X-ray polarizability, $\sigma_h = \kappa\chi_h/2\cos\theta_B$, θ_B is the Bragg angle, R_x is the crystal bending radius, $R(\check{y})$ is the flat-wave amplitude reflection coefficient, $\check{y}$ is the normalized angular variable, ξ_p is the coordinate of the observation point in the direction perpendicular to the reflected beam.

The integral over coordinate x in Eq. (2) reduces to the Airy function $\Phi(A_1/\{3A_2\}^{1/3})$, where

$$A_1 = -\kappa\xi_p/R_x + \check{y}\sigma_h, \quad A_2 = -\kappa\cos\theta_B/2R_x^2.$$

Considering for certainty a symmetric diffraction geometry, we can express the Airy function as follows:

$$\Phi(t) = (2^{-1}\pi^{-1/2})\int_{-\infty}^{+\infty} \exp\{ i(ut + u^3/3)\} du.$$

The integral over $\check{y}$ in Eq.(2) can be calculated using the stationary phase method by taking $\check{y}_{st} \approx 0$. The

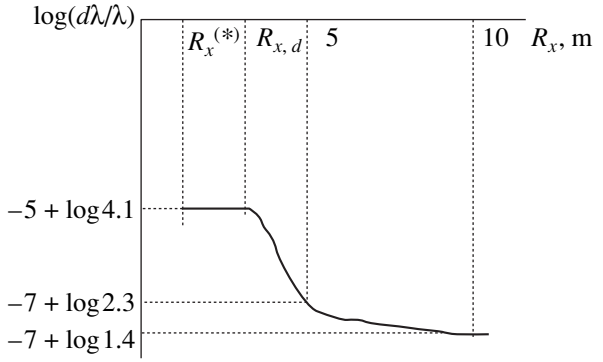

The logarithm of the spectral resolution versus crystal bending radius for the Johann focusing spectrometer. The source size is $d = 10$ μm = const; $R_{x,d} = d/(2\Delta\theta\sin\theta_B)$; the flat portion of the curve corresponds to the crystal radii obeying the condition $R_x \gg (3\pi\cos\theta_B)^{1/2}\lambda/\{(2\Delta\theta\sin\theta_B)^{3/2}\}$; and $R_x^{(*)}$ is the "critical" radius corresponding to weak bending of the reflecting crystal planes.

maximum maximorum of the Airy function (Φ = 0.9494) is attained at $t_{\max} \cong -1.02$. As can be seen, an allowance for the spherical aberration leads to noncoincidence of the points of geometric focus ($\xi_p = 0$) and maximum intensity.

Taking into account the properties of the Airy function, we can determine a diffraction width of the focus:

$$\Delta\xi_p \approx (3\pi)^{1/3} R_x^{1/3} (\cos\theta_B)^{1/3} \lambda^{2/3}. \quad (3)$$

The second model takes into account bending of the crystal surface: $z \approx x^2/2R_x$. In this case, the Johann scheme yields

$$L_h(x) = L_{h(0)}[1 + x\sin\varphi_h/L_{h(0)} + x^4\{-5\sin^2\varphi_0/2 + 1\}/(4R_x^4\cos^2\varphi_0) + x^4\{3\sin^2\varphi_0 - 1/2\}/(4R_x^4\cos^4\varphi_0). \quad (4)$$

Simple calculations lead to an expression for the intensity distribution in the form of the Pearsey integral [7]:

$$I_p(B_1 = 0, B_2) = \int_{-\infty}^{+\infty} \exp[\,i(B_2 t + t^4)]dt,$$

$$B_2 = \kappa\xi_p/\{R_x(B_4)^{1/4}\}, \quad (5)$$

$$B_4 = \kappa L_{h(0)}\{-5\sin^2\varphi_0/2 + 1 + 3\tan^2\varphi_0 - 1/(2\cos^2\varphi_0)\}.$$

Now let us consider the Johann focusing spectrometer within the framework of the first model of the crystal bending ($z \approx 0$). The spectral resolution calculated by formula (3) is worse as compared to the value derived in the existing theory [2–4]. One must take into account that, for a finite source size d, only a fraction $d_{coh} \approx 2\Delta\theta L_0$ contributes to the coherent diffraction reflection ($\Delta\theta$ is the angular halfwidth of the reflection profile). In this case, the spectral resolution is

$$d\lambda/\lambda = \cot\theta_B(\delta\xi_p + d_{coh})/L_{h(0)} \sim \cot\theta_B\{(3\pi\cos\theta_B)^{1/3}\lambda^{2/3}/(R_x^{2/3}\sin\theta_B) + 2\Delta\theta\}. \quad (6)$$

A numerical estimate of the resolution according to formula (6) for the (220) reflection of CuK_α radiation (λ = 1.54 Å) in a silicon crystal with $R_x \approx 1$ m yields $d\lambda/\lambda \sim 5 \times 10^{-5}$. It should be noted that the spectral resolution in the Johann scheme in the backscattering mode ($\theta_B \approx \pi/2$)

$$(d\lambda/\lambda)_{\pi/2} \le (3\pi)^{1/3}\lambda^{2/3}(\Delta\theta)^{4/3}/R_x^{2/3} + 2(\Delta\theta)^2 \quad (7)$$

is several times better than that for $\theta_B \neq \pi/2$ ($\sim 1.8 \times 10^{-5}$).

For a finite source size d, the best spectral resolution of the Johann spectrometer is achieved for a crystal bending radius $R_x > d/(2\Delta\theta\sin\theta_B)$ (see figure). As can be seen, for a sufficiently large radius $R_x \ge 10$ m (meeting the condition $R_x \cong R_{x,d} = d/(2\Delta\theta\sin\theta_B)$), the resolution can reach a level on the order of $\sim 10^{-7}$.

REFERENCES

1. H. H. Johann, Z. Phys. **69** (3), 185 (1931).
2. K. T. Gabrielyan, F. N. Chukhovskiĭ, and Z. G. Pinsker, Zh. Tekh. Fiz. **50** (1), 3 (1980) [Sov. Phys. Tech. Phys. **25**, 1 (1980)].
3. F. N. Chukhovskiĭ, Metallofizika **3** (5), 3 (1981).
4. K. T. Gabrielyan, F. N. Chukhovskiĭ, and D. I. Piskunov, Zh. Éksp. Teor. Fiz. **96** (3), 834 (1989) [Sov. Phys. JETP **69**, 474 (1989)].
5. K. T. Gabrielyan, G. O. Demirchyan, and F. N. Chukhovskiĭ, Zh. Tekh. Fiz. **60** (1), 170 (1990) [Sov. Phys. Tech. Phys. **35**, 102 (1990)].
6. F. N. Chukhovskiĭ, K. T. Gabrielyan, and P. V. Petrashen', Acta Crystallogr. A **34**, 610 (1978).
7. T. Pearsey, Philos. Mag. **37**, 311 (1946).

Translated by P. Pozdeev

Technical Physics Letters, Vol. 28, No. 4, 2002, pp. 305–307. Translated from Pis'ma v Zhurnal Tekhnicheskoĭ Fiziki, Vol. 28, No. 7, 2002, pp. 89–94.

Nanocrystalline Silicon Films Obtained by Plasma Enhanced Chemical Vapor Deposition under Time-Modulated-Microwave-Power Discharge Conditions

A. B. Pevtsov and N. A. Feoktistov

Ioffe Physicotechnical Institute, Russian Academy of Sciences, St. Petersburg, 194021 Russia

Received November 2, 2001

Abstract—It is suggested to use a time-modulated-microwave-power (TMWP) discharge regime for obtaining nanocrystalline silicon films by plasma-enhanced chemical-vapor deposition (PECVD) from a silane–hydrogen mixture. Using the TMWP–PECVD technique allows the nanocrystalline silicon films to be grown at a rate of up to 3 Å/s, which is 4–6 times as large as the process rate achieved with the conventional PECVD method. *© 2002 MAIK "Nauka/Interperiodica".*

In recent decades, thin semiconductor films containing nanocrystalline grains have drawn considerable attention of researchers both due to manifestations of the basic quantum confinement effects and in view of the interesting prospects for their practical applications [1, 2]. One type of the nanodimensional systems of this kind are thin silicon films possessing a mixed amorphous-nanocrystalline phase composition, grown from silane–hydrogen mixtures by method of plasma enhanced chemical vapor deposition (PECVD) [3–5].

Technological conditions favoring the PECVD of nanocrystalline films are provided by strongly diluting silane with hydrogen (>95%) [3]. A high concentration of hydrogen in the plasma shifts the chemical equilibrium of the competitive growth–etching processes at the plasma–film interface toward intensive etching of energetically unfavorable amorphous configurations in the growing film [6], thus leading to a preferential growth of crystalline nuclei. In this way, it is possible to control the size and volume fraction of crystalline grains in the film, as well as the film porosity. This technology is low-sensitive to the type of substrate and is well compatible with the standard silicon technology. The main disadvantage of the PECVD method is the relatively low (<1 Å/s) rate of the film growth.

Further development of the PECVD technology can be related to the use of nonstationary techniques based on the pulsed switching of vapor deposition regimes in the course of the film growth. Using this approach, it is possible to separate in time the formation of crystalline nuclei, etching of the amorphous clusters, and subsequent stabilizing annealing of the film [7–9]. Using a nonstationary PECVD can provide for the growth of nanocrystalline films at a higher rate [9]. However, realization of this method requires rapid (within fractions of a second) switching of the gas flows and differential pumping of the reactor between separate stages of the technological process. These requirements pose certain limitations on the possibility of pulsed modulation of the deposition parameters, especially in the case of large reactors employed for the obtaining of films on large substrates.

An alternative approach to the synthesis of nanocrystalline films suggested in [10] is based on the possible formation of crystalline silicon clusters immediately in a silane plasma. The formation of such a powder in the plasma discharge is explained by the following evolution: radicals ⟶ macromolecules ⟶ crystalline clusters ⟶ agglomerates ⟶ powder. In this connection, it would be of interest to provide for conditions in a plasma discharge favoring the formation of predominantly nanodimensional crystalline clusters, the deposition of which will lead to the growth of a nanocrystalline silicon (nc-Si) film.

In this paper, we suggest using the PECVD method under time-modulated-microwave-power (TMWP) discharge conditions. Use of the microwave discharge leads to a more effective decomposition of silane as compared to that achieved in a diode system operated at a frequency of several tens of megahertz [11]. The microwave plasma operation at a pressure on the order of 0.1 Torr is usually accompanied by intensive formation of silicon powder. By modulating the microwave discharge power, it is possible to control the size of silicon species formed in the plasma. It is assumed that switching off the discharge in the stage of cluster formation in the plasma would prevent the clusters from further growth in size.

In our experiments, the microwave (2.45 GHz) radiation power was modulated by a meander signal comprising a sequence of 2-ms rectangular pulses with a filling ratio variable from 1 : 4 to 1 : 10. The other process parameters were as follows: pulse power, 0.7–1 kW; silane relative content in hydrogen, K = 0.5–2%; gas pressure, P = 0.1–0.3 Torr; substrate tem-

1063-7850/02/2804-0305$22.00

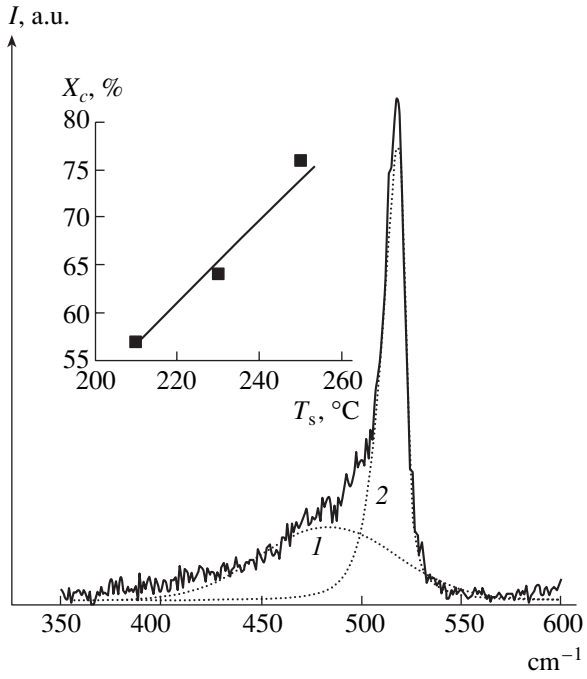

Fig. 1. The Raman spectrum of a silicon film with a mixed amorphous-nanocrystalline phase composition, grown at T_s = 200°C and P = 0.3 Torr. Dashed curves show deconvolution of the total experimental spectrum into (*1*) amorphous and (*2*) crystalline components. The crystalline grains are ~5 nm in size and their volume fraction in the film is X_c = 57%. The inset shows the plot of X_c versus substrate temperature T_s.

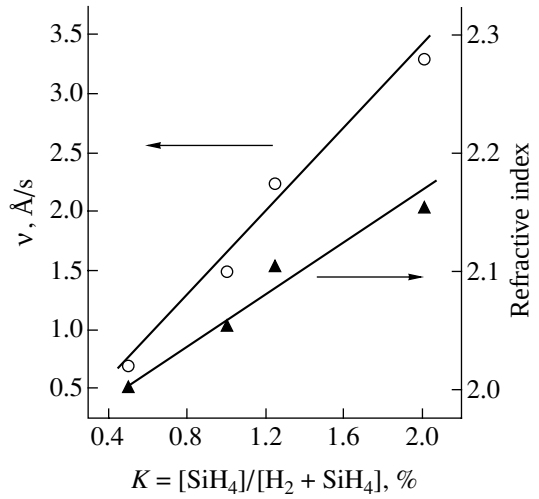

Fig. 2. The plots of film growth rate (circles) and refractive index (triangles) versus silane concentration in the gas phase for silicon films with a mixed amorphous-nanocrystalline phase composition.

perature T_s = 200–350°C; and total gas flow rate, 10–30 cm^3/min. The microwave power was supplied through a quartz window spaced by 70 mm from a heater stage holding quartz substrates. The film thickness and refractive index were measured with the aid of a laser interferometer. The thicknesses of silicon films grown in our experiments ranged from 200 to 300 nm.

The phase composition of a grown film was determined from the Raman scattering spectra [12]. Figure 1 shows a typical Raman spectrum of a sample grown at T_s = 200°C, P = 0.3 Torr and a relative silane content in hydrogen K = 1%. The spectrum represents a broad band with a maximum near 480 cm^{-1} corresponding to an amorphous phase and a narrow line peaked at 520 cm^{-1} shifted toward lower frequencies relative to the Raman-active transverse phonon mode of the crystalline silicon. The volume fraction and average size of the crystalline grains were determined by numerically processing the Raman scattering spectra with an allowance for a strong spatial confinement of the optical phonons in nanocrystalline grains [12]. For the given sample, the volume fraction of crystalline grains was ~57% and the average size of crystalline grains was ~5 nm. The inset in Fig. 1 shows a plot of the calculated volume fraction of the crystalline phase (X_c) versus substrate temperature T_s for the films studied. As can be seen, the fraction of nanocrystalline grains grows from 57 to 76% when the substrate temperature increases from 200 to 260°C.

Figure 2 shows the plots of the film growth rate and refractive index of the nc-Si films versus silane content K in the gas mixture, constructed by the results of laser interferometry measurements performed in the course of the film growth. In the range of K = 0.5–2%, the volume fraction of the crystalline phase exceeded 50%. As can be seen, the film growth rate reached 3 Å/s (for K = 2%), which is significantly higher than the rate of thickness increase (0.5–0.7 Å/s) for the nanocrystalline silicon films grown by the conventional PECVD technique at the same silane concentration (K = 2%) [12]. Thus, using the TMWP–PECVD method provides for a four- to six-fold increase in the growth rate of nanocrystalline silicon films.

The plot of refractive index versus silane concentration (Fig. 2) shows a small increase in n (from 2.0 to 2.15) when the silane content is increased from 0.5 to 2% (at T_s = 200°C). Values of n close to 2 were also typical of the nc-Si films grown at other substrate temperatures in the range T_s = 180–260°C. Thus, the nc-Si films possess the refractive indices significantly smaller than the values typical of crystalline or amorphous silicon (n ~ 3.9 at λ = 633 nm). This large difference is probably explained by a considerable porosity of the films, the amount of which can be determined within the framework of the effective dielectric medium approximation [13] using experimental values of n (n = 2.0–2.15 for nc-Si:H; n = 1.0 for pores; and n = 3.9 for silicon). Estimates showed that the value of porosity for the samples studied reaches ~70%.

The high porosity of the films deposited under the conditions studied was confirmed by the electric conductivity measurements. The conductivity varied from

10^{-7} to 10^{-5} Ω^{-1} cm^{-1} (depending on K and T_s). This is lower by 5–7 orders of magnitude as compared to the conductivity of nanocrystalline silicon films grown by standard PECVD, which had a volume fraction of the nanocrystalline phase $X_c \geq 16\%$ and featured the formation of an infinite conducting percolation cluster [12]. We believe that the presence of a large volume fraction of pores in the TMWP–PECVD films hinders the formation of such a conducting percolation cluster from silicon nanocrystalline grains between electrodes and is the most probable reason for low values of the conductivity. Note that a large porosity of the silicon films may also be indirect evidence for the film growth by a mechanism involving the fragments of silicon clusters formed in the gas phase. According to this, clusters reaching a few nanometers in size are randomly deposited onto a substrate surface and remain virtually immobile, which accounts for the high porosity of the films.

Thus, the use of a time-modulated-microwave-power discharge regime for the plasma enhanced chemical vapor deposition process allowed us to increase the rate of growth of nanocrystalline silicon films up to 3 Å/s. An analysis of the characteristics of these films suggests that the films grow according to a mechanism involving the deposition of fragments of silicon clusters formed in the gas phase.

Acknowledgments. The authors are grateful to V.G. Golubev for fruitful discussions.

This study was supported within the framework of a project of the European Society TIMOC (grant no. ERB ICL 15CT98 0819).

REFERENCES

1. L. Brus, Appl. Phys. A **A53** (6), 465 (1991).
2. C. Weisbuch, Optoelectron., Devices Technol. **8** (4), 523 (1993).
3. T. Hamasaki, H. Kurata, M. Hirose, and Y. Osaka, Appl. Phys. Lett. **37** (12), 1084 (1980).
4. A. T. Voutsas, M. K. Hatalis, J. Boyce, and A. Chiang, J. Appl. Phys. **78**, 6999 (1995).
5. Ch. Yin, X. Liu, and Y. He, J. Appl. Phys. **75**, 797 (1994).
6. Z. Iqbal and S. Veprek, J. Phys. C **15**, 377 (1982).
7. M. Otobe and S. Oda, Jpn. J. Appl. Phys. **31** (1), 1948 (1992).
8. G. N. Parsons, J. J. Boland, and J. C. Tsang, Jpn. J. Appl. Phys. **31** (1), 1943 (1992).
9. S. Koynov, R. Schwarz, T. Fisher, *et al.*, Jpn. J. Appl. Phys. **33** (1), 4534 (1994).
10. P. Roca and I. Cabarrocas, Mater. Res. Soc. Symp. Proc. **507**, 855 (1998).
11. N. Itagaki, A. Fukuda, T. Yoshizawa, *et al.*, Surf. Coat. Technol. **131**, 54 (2000).
12. V. G. Golubev, V. Yu. Davydov, A. V. Medvedev, *et al.*, Fiz. Tverd. Tela (St. Petersburg) **39**, 1348 (1997) [Phys. Solid State **39**, 1197 (1997)].
13. D. E. Aspnes, Thin Solid Films **89**, 249 (1982).

Translated by P. Pozdeev

Technical Physics Letters, Vol. 28, No. 4, 2002, pp. 308–310. Translated from Pis'ma v Zhurnal Tekhnicheskoĭ Fiziki, Vol. 28, No. 8, 2002, pp. 1–7.

Synthesis and Study of a Perovskite Phase of Yttrium Barium Metal Oxide Ceramics

M. U. Kalanov and E. M. Ibragimova

Institute of Nuclear Physics, Academy of Sciences of the Republic of Uzbekistan, Tashkent, Uzbekistan

Received September 19, 2001

Abstract—A homogeneous cubic perovskite phase of an yttrium–barium ceramics was obtained by creating thermoelastic stresses in a rapidly heated sample of a certain size. The structural parameters of the new phase were determined, and the electric conductivity was measured. © *2002 MAIK "Nauka/Interperiodica".*

The crystal structure of $YBa_2Cu_3O_{7-\delta}$ (YBCO) ceramics belongs to the class of perovskites. In contrast to the ideal perovskite structure (ABO_3), the yttrium cuprate exhibits unsaturated coordination with respect to cations. If all the allowed anionic positions in the lattice of a superconducting yttrium–barium ceramics were occupied by oxygen atoms, the structure would correspond to the perovskite composition $YBa_2Cu_3O_9 = [(Y,Ba)CuO_3]_3$. Therefore, there is a theoretical potential possibility of intercalating two additional oxygen atoms into the unit cell of a superconducting yttrium–barium ceramics [1]. For this purpose, it is necessary to deform the initial orthorhombic lattice by applying external factors so that all anionic positions would become equipotential. Such an increase in the lattice symmetry of the initial ceramics is accompanied by a phase transition.

Attempts at deforming the initial lattice of the $YBa_2Cu_3O_{7-\delta}$ ceramics (so as to introduce two additional oxygen atoms) by thermal or radiation-thermal methods did not lead to the desired results [2, 3]. However, the lattices of oxide-based materials can be also deformed by mechanical means [4]. In particular, it was reported that a thin film of an yttrium–barium ceramics grown on a magnesium oxide substrate proved to be heterogeneous. The film structure comprised alternating layers of the superconducting 123-phase and a cubic perovskite phase, which was caused by internal stresses related to the lattice mismatch between film and substrate [5]. An analogous heterogeneous composition was obtained for a powdered YBCO ceramic sample treated at room temperature in a vibrating mill for 65 h or longer, which led to straining of the surface layers of ceramic particles [6].

Previously [7], we demonstrated the possibility of obtaining a perovskite phase of the YBCO ceramics by creating thermoelastic stresses in the sample. Thus, from the standpoint of the complete phase diagram of the YBCO system, the question concerning the existence of a homogeneous perovskite phase is still open. In particular, it is unclear how cations are arranged, what is the stoichiometry of anions in the corresponding sublattice, and how the conductivity of the whole system would behave. The purpose of this study was to answer these questions. We report on the synthesis, structural analysis, and study of the electrical properties of a homogeneous perovskite phase in the YBCO system.

The initial materials were powdered oxides Y_2O_3, Ba_2O_3, and CuO taken in the ratio Y : Ba : Cu = 1 : 2 : 3 so as to obtain an $YBa_2Cu_3O_{7-\delta}$ composition. The initial powders were triturated for a prolonged time (>10 h) in an agate mortar and pressed into pellets (with a diameter of 10 mm and a thickness not exceeding 0.6 mm) under a pressure of 1 GPa. Then the pellets were placed into individual cells made of 0.5-mm nichrome wire and arranged in a furnace so as to exclude touching one another or the inner wall surface. The samples were annealed for 20 min at a temperature of 1173 K and then rapidly heated to a temperature slightly above the melting temperature (T_m = 1250–1323 K). After a short-time (<3 min) exposure at this temperature, the samples were allowed to cool down to room temperature with the furnace. Note that exposure above 3 min at $T > T_m$ led to partial surface fusion of the pressed pellets. The structural characteristics of the pellets were determined by X-ray diffraction measured on a DRON-UM1 diffractometer using Cu$K\alpha$ radiation. The temperature dependence of the resistivity was studied by the conventional four-point-probe technique at a dc current of 1 mA in the temperature interval from 77 to 300 K.

Figure 1c shows a typical X-ray diffractogram of the as-sintered YBCO sample measured in the point-by-point scan mode. This diffraction pattern principally differs from that observed for a superconducting 123-phase of the YBCO ceramics. An analysis of the X-ray diffraction reflections showed that the pattern fully conforms to the space group $Pm3m$. This corresponds to a simple cubic cell with the lattice parameter a_c = 0.4051 nm. Within the framework of the $Pm3m$ space group, the atomic positions in the unit cell are as follows: 1b positions with the coordinates (1/2, 1/2, 1/2)

1063-7850/02/2804-0308$22.00 © 2002 MAIK "Nauka/Interperiodica"

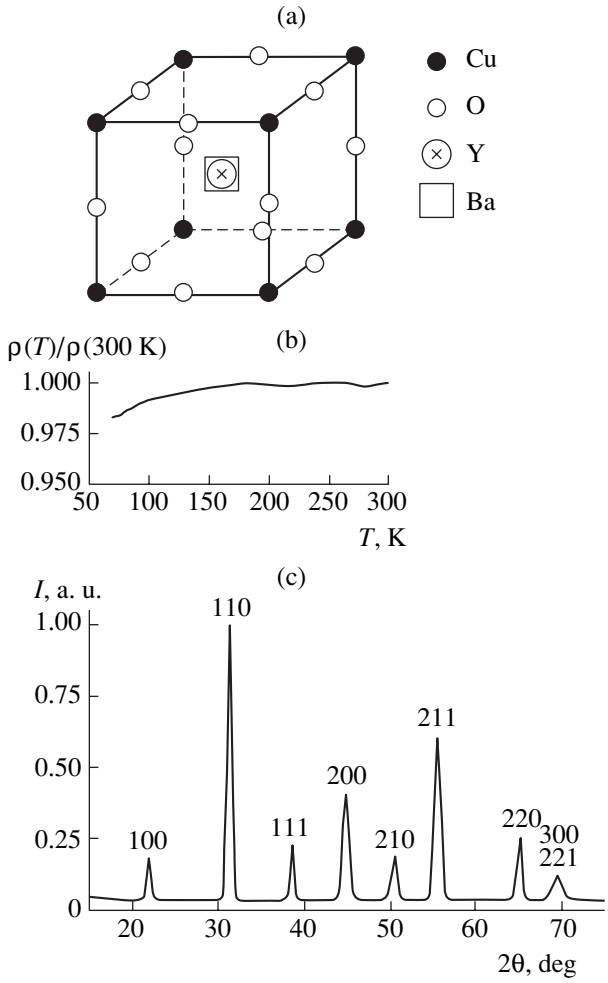

Fig. 1. The perovskite phase $[(Y,Ba)CuO_{3-\Delta/3}]_3$ of the YBCO ceramics: (a) unit cell structure; (b) temperature dependence of the resistivity $\rho(T)$; (c) X-ray diffractogram.

are occupied by yttrium and barium atoms according to the Y/Ba weight ratio (1/3 Y and 2/3 Ba); 1a positions with the coordinates (0, 0, 0) are occupied by copper atoms; and 3d positions with the coordinates (1/2, 0, 0), (0, 1/2, 0), and (0, 0, 1/2) are occupied by oxygen atoms (see Fig. 1a). The reflection intensities were calculated either by the trial method [8] or using the Ritweld profiles [9]; in the case under consideration, both methods gave identical results.

The experimental and calculated intensities of the diffraction reflections were compared within the framework of four possible models, in which the atomic positions in the unit cell are occupied as follows:

(i) 1b, yttrium and barium atoms (statistically distributed according to the weight ratio); 1a and 3d, completely filled by copper and oxygen atoms, respectively;

(ii) 1b, only yttrium; 1a and 3d, as in variant (i);

(iii) 1b, only barium; 1a and 3d, as in variant (i);

(iv) 1b and 1a, as in variant (i); 3d, incompletely occupied by oxygen (with a nonstoichiometry Δ).

The values of the reliability factor $R = (\Sigma|F_{obs} - F_{cal}|)/\Sigma|F_{obs}|$ for variants (ii) and (iii) (see table) were 14.3 and 9.7%, respectively, while that for variant (i) was 3.8%. The minimum value of this factor ($R = 1.1\%$) was obtained for variant (iv). Proceeding from the minimum R value, the YBCO ceramic phase studied can be described by the formula $[(Y,Ba)CuO_{2.85/3}]_3$ ($\Delta = 0.15$) representing a perovskite with a disordered arrangement of barium and yttrium atoms in the cationic sublattice and with an oxygen nonstoichiometry in the anionic sublattice. In our opinion, the condition of lattice electroneutrality in this phase requires that copper and oxygen atoms would be ambivalent.

As is known, rapid heating and cooling of a crystal may lead to a change of the entropy, thermal expansion, and the development of thermoelastic stresses [10]. Reaching a critical level for a given material, the thermoelastic stresses produce plastic deformation of the lattice. Under these conditions, the material structure formed in the course of deformation may experience a phase transition. The critical level of thermal stresses

Structural parameters of the $[(Y,Ba)CuO_{3-\Delta/3}]_3$ perovskite phase (space group, $Pm3m$; $a_c = 0.4051$ nm)

No.	*HKL*	d_{obs}, nm	d_{cal}, nm	I_{obs}, %	I_{cal}, %	
					$\Delta = 0$	$\Delta = 0.15$
1	100	0.4051	0.4056	15.2	12.6	13.9
2	110	0.2872	0.2864	100	100	100
3	111	0.2342	0.2345	23.8	27.1	24.3
4	200	0.2044	0.2038	44.7	51.3	46.5
5	210	0.1811	0.1814	16.4	13.5	15.7
6	211	0.1662	0.1656	64.5	57.8	62.8
7	220	0.1433	0.1437	23.5	30.6	26.1
8	300; 221	0.1351	0.1356	7.8	14.3	9.9
R, %					3.8	1.1

can be evaluated by the formula $\sigma_c = \alpha E \Delta T$, where α is the linear expansion coefficient, E is the Young modulus, and ΔT is the temperature gradient [10]. Using the measured values of the thermal expansion coefficients ($\alpha_a = 9.47 \times 10^{-6}$ K^{-1}, $\alpha_b = 7.03 \times 10^{-6}$ K^{-1}, $\alpha_c = 17.2 \times 10^{-6}$ K^{-1}) and the Young modulus ($E = 50.4$ GPa $\approx 5 \times 10^{10}$ Pa) taken from [11] (for $\Delta T = 100$ K), we obtain $\sigma_c = 48$–86 MPa. This value is sufficient to provide for the plastic deformation in the lattice of the 123-phase of the YBCO ceramics. This estimate of the critical thermal stress agrees with the data obtained in [12], where $\sigma_c = 60$ MPa was reported.

Figure 1b shows the temperature dependence of the resistivity $\rho(T)/\rho(300\ K)$ of an as-sintered $[(Y,Ba)CuO_{2.85/3}]_3$ ceramics measured in the temperature interval from 77 to 300 K. As can be seen, the sample resistivity remained virtually constant in the range from room temperature to liquid nitrogen temperature ($\rho(T) \approx$ const). However, this behavior cannot be considered as indicative of the dielectric properties of the perovskite phase of the YBCO ceramics studied. Indeed, the measured values of resistivity ($\rho(300\ K) = 8.71 \times 10^{-2}\ \Omega$ cm, $\rho(100\ K) = 8.53 \times 10^{-2}\ \Omega$ cm) are not characteristic of insulators typically possessing $\rho(300\ K) \cong 10^{10}$–$10^{20}\ \Omega$ cm [13]. In our opinion, the conductivity of the phase under consideration is determined by the interplay of two components, metallic and semiconducting. The latter component is caused by the hopping conductivity related to the carrier localization on two types of structural disorder: anionic (oxygen) vacancies and cationic sites in the yttrium–barium sublattice.

Thus, the Y–Ba–Cu–O system structure admits a perovskite modification. In contrast to most compounds in the perovskite group, the $[(Y,Ba)CuO_{3-\Delta/3}]_3$ phase under normal conditions does not possess dielectric properties and exhibits conductivity determined by the contributions of at least two mechanisms.

REFERENCES

1. Yu. I. Smolin, Yu. F. Shepelev, and A. A. Levin, Zh. Neorg. Khim. **34** (10), 2451 (1989).
2. M. S. Paĭzullakhanov, M. U. Kalanov, and V. M. Rustamova, Pis'ma Zh. Tekh. Fiz. **21** (5), 38 (1995) [Tech. Phys. Lett. **21**, 182 (1995)].
3. É. G. Ashirov, É. G. Gasanov, É. M. Ibragimova, *et al.*, Sverkhprovodimost: Fiz., Khim., Tekh. **3** (7), 1454 (1990).
4. V. M. Timchenko, G. Ya. Akimov, and N. G. Labinskaya, Zh. Tekh. Fiz. **69** (2), 27 (1999) [Tech. Phys. **44**, 156 (1999)].
5. J. A. Agostinelli, Samuel Chen, and G. Braunstein, Physica C (Amsterdam) **180** (1/4), 26 (1991).
6. F. Lavallec, M. Simoneau, G. L. Esperance, and R. Schulz, Phys. Rev. B **44** (21), 12003 (1991).
7. M. U. Kalanov, M. S. Paizullakhanov, V. M. Rustamova, *et al.*, in *Abstracts of the Third International Conference "Modern Problems of Nuclear Physics," Bukhara, Uzbekistan, 1999*, p. 350.
8. M. A. Poraĭ-Koshits, *Practical Course of X-ray Structure Analysis* (Mosk. Gos. Univ., Moscow, 1960), Vol. 2.
9. S. V. Tsybulya, S. V. Cherepanova, and L. P. Solov'eva, Zh. Strukt. Khim. **37** (2), 379 (1996).
10. W. W. Wendlandt, *Thermal Methods of Analysis* (Wiley, New York, 1974; Mir, Moscow, 1978).
11. A. C. Momin, M. D. Mathews, V. S. Jakkel, *et al.*, Solid State Commun. **64** (3), 329 (1987).
12. A. G. Ivanov and L. T. Tsymbal, Phys. Lett. A **148** (12), 131 (1990).
13. B. M. Tareev, *Physics of Dielectric* (Énergoatomizdat, Moscow, 1982).

Translated by P. Pozdeev

Technical Physics Letters, Vol. 28, No. 4, 2002, pp. 311–314. Translated from Pis'ma v Zhurnal Tekhnicheskoĭ Fiziki, Vol. 28, No. 8, 2002, pp. 8–17.

Thermodynamic Elastic-Strain Mechanism Controlling the Dynamics of Properties and Phase States in Magnetic Semiconductors

P. I. Polyakov and S. S. Kucherenko

Donetsk Physicotechnical Institute, National Academy of Sciences of Ukraine, Donetsk, Ukraine
e-mail: poljakov@host.dipt.donetsk.ua

Received November 13, 2002

Abstract—The effects of high hydrostatic pressure, magnetic field, and temperature on the dynamics of electric resistance are studied in the ceramic and film samples of $La_{0.56}Ca_{0.24}Mn_{1.2}O_3$ and $La_{0.7}Mn_{1.3}O_3$. It is found that the same variations of the sample conductivity are observed in response to equivalent changes in the temperature (by 6.4 K), magnetic field strength (2.4 kOe), or hydrostatic pressure (1 kbar). An analysis of the experimental data allows a thermodynamic mechanism accounting for the elastic anisotropic straining and determining the dynamics of properties and phase states in the magnetic semiconductors to be established. The baroresistance and baromagnetoresistance effects are revealed. The magnetoelastic-strain mechanism of realization of the giant magnetoresistance effect is outlined. © *2002 MAIK "Nauka/Interperiodica".*

Introduction. The nature of the unique interplay of the magnetic and electric properties of manganites is still a subject of discussion, despite a large number of publications and reviews [1]. In recent years, researchers frequently use nontraditional approaches to the study of rare-earth (RE) manganites, according to which changes in the conductivity characteristics were observed in response to the action of temperature, magnetic field, and hydrostatic pressure [2–4].

It was established [5–7] that the magnetic properties and resistance of RE manganites are highly sensitive to changes in applied magnetic field strength and external pressure. The possibility of measuring the effect of these external factors on the properties and phase states on magnetic semiconductors revealed several new effects not studied previously. An analysis of the observed effects of temperature, pressure, and magnetic field on the conductivity of magnetic semiconductors allowed us to propose a mechanism responsible for the dynamics of properties and phase states in these materials.

Experimental results. The ceramic and film samples of $La_{0.56}Ca_{0.24}Mn_{1.2}O_3$ and $La_{0.7}Mn_{1.3}O_3$ were synthesized by traditional methods [8]. The high hydrostatic pressures were obtained as described in [9] and measured by a manganin-based pressure sensor.

Figures 1 and 3 show the temperature dependences of resistivity of the samples measured at various magnetic field strengths (thermomagnetoresistance) or at various hydrostatic pressures (thermobaroresistance). The measurements performed with applied magnetic field at various fixed pressures illustrate the thermobaromagnetoresistance effect (Figs. 1 and 3, curves *6*). A shift of the metal–semiconductor phase transition temperature under the action of an applied magnetic field and pressure is evidence of an increase in the inter-

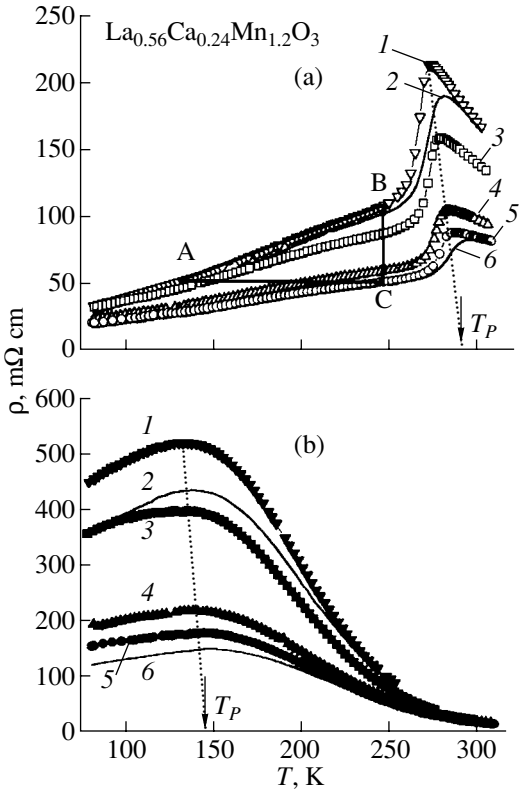

Fig. 1. Temperature dependences of the resistivity of (a) ceramic and (b) film samples of $La_{0.56}Ca_{0.24}Mn_{1.2}O_3$ measured without applied magnetic field at $P = 0$ (*1*), 6 (*3*), 12 (*4*), and 18 kbar (*5*) and in the field of $H = 8$ kOe at $P = 0$ (*2*) and 18 kbar (*6*).

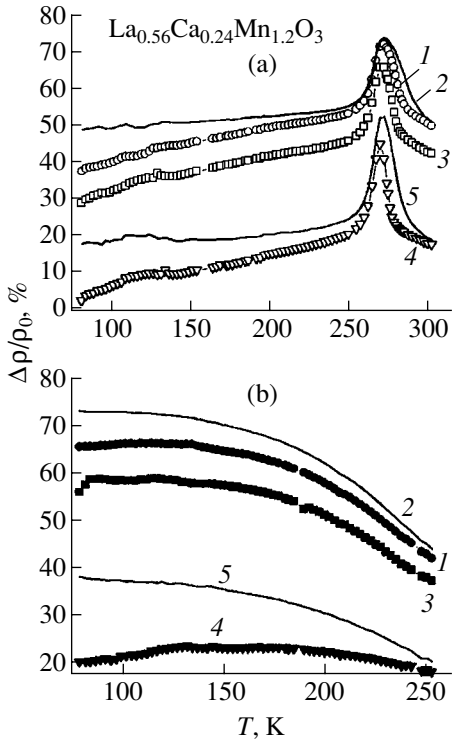

Fig. 2. Temperature dependences of the resistivity of (a) ceramic and (b) film samples of $La_{0.56}Ca_{0.24}Mn_{1.2}O_3$. Baroresistance effect, P = 18 (*1*), 12 (*3*), and 6 kbar (*4*); baromagnetoresistance effect, H = 8 kOe, P = 18 (*2*) and 6 kbar (*5*).

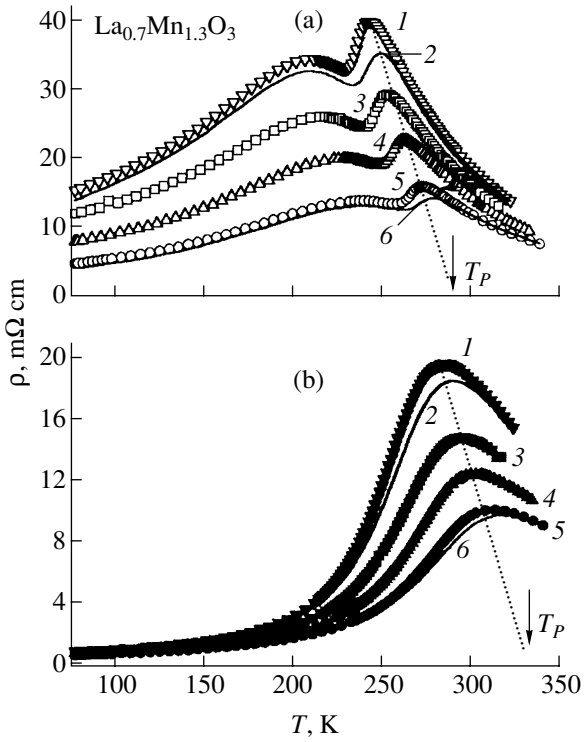

Fig. 3. Temperature dependences of the resistivity of (a) ceramic and (b) film samples of $La_{0.7}Mn_{1.3}O_3$ measured without applied magnetic field at P = 0 (*1*), 6 (*3*), 12 (*4*), and 18 kbar (*5*) and in the field of H = 8 kOe at P = 0 (*2*) and 18 kbar (*6*).

nal energy (electrostatic bonds) necessary for the transition.

By analogy with the magnetoresistance data, we measured the dependences illustrating the phenomena of baroresistance $(\rho_0 - \rho_P)/\rho_0$ [%] (Figs. 2 and 4, curves *1*, *3*, and *4*) and baromagnetoresistance $(\rho_0 - \rho_{PH})/\rho_0$ [%] (Figs. 2 and 4, curves *2* and *5*) at various hydrostatic pressures. Here, ρ_0 is the initial resistivity, ρ_P is the resistivity at a given hydrostatic pressure, and ρ_{PH} is the resistivity measured in a magnetic field (H = 8 kOe) at a fixed hydrostatic pressure. These relationships clearly illustrate the dynamics of resistivity in response to the pressure variation.

Discussion of results. The curves of baroresistance and baromagnetoresistance show evidence of two competing processes: the temperature induces thermal expansion of the crystal lattice, while the hydrostatic pressure and magnetic field tend to elastically compress the structure. The structure deformations were monitored by measuring the temperature dependence of resistivity under various conditions.

1.1. The experimental plots of $\rho(T)$ (Fig. 1a, curves *1*, *3*–*5*) display a linear portion extending up to 250 K. This dynamics is determined by the thermal expansion of the crystal lattice. The linearity of $\rho(T)$ is retained at various pressures. A competition between the elastic strain induced by increasing hydrostatic pressure and the thermal expansion is reflected by the decreasing slope of the $\rho(T)$ plots.

Since both temperature (thermoelastic strain) and pressure (elastic strain) control the dynamics of resistivity, we can estimate a change in the temperature necessary to produce the same change in ρ as that observed for a pressure increment of 1 kbar. In the linear portion of the $\rho(T)$ plot, the increment of resistivity $\Delta\rho$ per kelvin amounts to $\Delta\rho/\Delta T = 0.51$ Ω/K (Fig. 1a, curve *1*). Measured at a temperature of $T \approx 225$ K, a change in the resistivity per unit pressure increment is $\Delta\rho/\Delta P \approx 3.27$ Ω/kbar. This value was obtained using the ABC triangle (Fig. 1a, curves *1* and *5*), from which it is seen that a change in the temperature by $\delta T \approx 7$ K over a linear portion of $\rho(T)$ leads (due to a thermoelastic strain) to the same change in conductivity as that produced by a 1 kbar hydrostatic pressure increment. These values characterize the level of stresses involved in the thermoelastic straining of the sample structure.

1.2. The dynamics of resistivity (Figs. 1a and 1b, curves *2* and *6*) shows evidence of a nouniform variation of the sample resistance under the action of an applied magnetic field in various temperature intervals. The same behavior of $\rho(T)$ was observed for the combined action of a hydrostatic pressure and a magnetic field of H = 8 kOe (Figs. 1a and 1b, curves *6*; Figs. 3a and 3b, curves *2*).

Taking into account the linear character of contributions due to the pressure and magnetic field [6] to the resistivity dynamics, we can separate the most important region in a thermodynamically unstable region of maxima corresponding to the phase transitions (Figs. 1a and 1b, curves *1* and *2*). As can be seen from the $\rho(T, P, H)$ dependences (Fig. 1a, curves *1* and *2*) the effect of a magnetic field with a strength of $H = 1$ kOe corresponds to an increase in resistivity by $\Delta\rho/\Delta H = 2.96$ Ω/kOe. The pressure-induced variation of resistivity in the same temperature interval (Fig. 1a, curves *1*–*5*) amounts to $\Delta\rho/\Delta P = 7$ Ω/kbar. These data indicate that an increase in the magnetic field strength by $\delta H = 2.37$ kOe produces (by magnetostrictive stresses elastically deforming the crystal structure) the same change in the conductivity as does a 1 kbar increase in the hydrostatic pressure. The compressing mechanism of the magnetic field action is confirmed by a shift of the phase transition peak comparable to an analogous effect of the elastically straining hydrostatic pressure.

1.3. Taking into account experimental errors involved in the measurement of hydrostatic pressures (related to the losses for friction in joints and a pressure drop caused by decreasing temperature), we can estimate the accuracy of pressure determination at 10–15% on a level of 20 kbar. Therefore, a change in the temperature by $\delta T \approx 7$ K modifies the sample resistivity by a thermoelastic strain mechanism to an extent comparable with the effect of a 1 kbar increment in the hydrostatic pressure. By extrapolating a pressure-induced shift in the phase transition temperature (Figs. 1 and 3), we can numerically estimate the temperature T_P required to induce a counterpressure sufficient to suppress the metal–semiconductor phase transition. This temperature is determined at the point of intersection of the extrapolated plot and the temperature axis. The value of counterpressure can be estimated from the $T_P/\delta T$ ratio.

For $La_{0.56}Ca_{0.24}Mn_{1.2}O_3$, we obtain $T_P = 290$ K and the counterpressure $P = 42$ kbar for ceramics (Fig. 1a) and $T_P = 150$ K, $P = 22$ kbar for the film (Fig. 1b). For $La_{0.7}Mn_{1.3}O_3$, the corresponding values are $T_P = 285$ K, $P = 41$ kbar for ceramics (Fig. 3a) and $T_P = 335$ K, $P = 48$ kbar for the film (Fig. 3b). For a film of the composition $La_{0.7}Ca_{0.3}MnO_3$ [4], $T_P = 275$ K and $P = 39$ kbar; for $La_{0.7}Ca_{0.3}Mn_{0.98}Fe_{0.02}O_3$ [11], $T_P = 215$ K and $P = 31$ kbar; and for $La_{0.7}Ca_{0.3}Mn_{0.96}Fe_{0.04}O_3$ [11], $T_P = 175$ K and $P = 25$ kbar. These values can be readily verified in experiment.

From these data, it follows that the proposed thermodynamic mechanism of elastic anisotropic stresses [10] deforming the structure and determining the dynamics of properties and phase states is both qualitatively and quantitatively correct. The strain produced by these stresses is sufficiently large and increases with temperature.

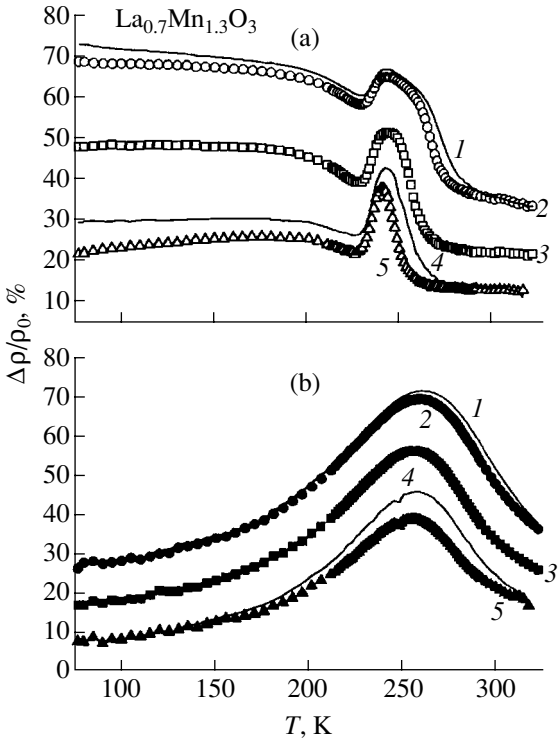

Fig. 4. Temperature dependences of the resistivity of (a) ceramic and (b) film samples of $La_{0.7}Mn_{1.3}O_3$. Baroresistance effect, $P = 18$ (*2*), 12 (*3*), and 6 kbar (*5*); baromagnetoresistance effect: $H = 8$ kOe, $P = 18$ (*1*) and 6 kbar (*4*).

1.4. The observed variation of the baromagnetoresistance effect (Figs. 2 and 4, curves *2* and *5*) reveals the dynamics of nonuniform influence of the magnetic field upon the electron properties of samples in various temperature intervals. This contribution is more pronounced at low temperatures. Therefore, any technological procedures (annealing, doping, etc.) producing structural changes increasing the phase transition temperature of a given composition lead to a decrease in the magnetoresistance effect.

A comparative analysis of the effects of temperature, magnetic field, and hydrostatic pressure on the resistance—a parameter sensitive to any structural changes—allowed us to suggest a common mechanism responsible for these effects.

2.1. The temperature is the main thermodynamic parameter controlling the properties, their anisotropy, and the phase state of the samples studied. On the other hand, the phase state, properties, and their anisotropy and dynamics reflect the chemical bonds and symmetry features of a given structure. The electric field determines the behavior of conductivity, which is most sensitive to any changes in the structure. The above comparative estimates of the relative contributions of temperature and pressure to the dynamics of resistivity characterize (with sufficient confidence) the magnitude of elastic stresses developed in the sample structure. Taking this into account, we conclude that the dynam-

ics of properties and phase states involves colossal internal elastic stresses in the material.

2.2. An applied magnetic field induces coercive forces elastically straining the sample structure in the entire temperature range, which also influences the dynamics of conductivity, as reflected by the observed thermomagnetoresistance effect (Figs. 1a and 1b, curves *2*). The magnetic field, as well as the hydrostatic pressure, induces anisotropic elastic stresses modifying the structural parameters. A 1 kbar hydrostatic pressure change is equivalent to a magnetic field strength increment of 2.5 kOe with respect to the structure deformation and the conductivity dynamics. The obtained estimates clearly illustrate the mechanism of magnetic elastic stresses controlling the dynamics of resistivity. In this context, the giant magnetoresistance effect can be considered as a resistivity jump by the mechanism of magnetostrictive anisotropic-elastic-stress-induced structural changes caused by an external magnetic field.

2.3. The hydrostatic pressure gives rise to anisotropic elastic stresses modifying the structural parameters, as manifested by the resistance dynamics illustrated in Fig. 1 (curves *1*, *3–5*) and by the temperature shift and intensity decrease of the phase transition peak in Fig. 2 (curves *1*, *3*, *4*). An analysis of these results also points to the existence of an elastic anisotropic straining mechanism. From this standpoint, the counterpressure suppresses the dynamics of resistivity and phase state, as can be seen (Figs. 1a and 1b, 3a and 3b, curves *1*, *3–5*). Therefore, it is possible to estimate the levels of counterpressures comparable with the thermoelastic stresses determining the phase transition. However, exact estimates can be obtained only by direct investigations of single crystal samples.

Conclusions. Our experimental investigation of the dynamics of resistivity under the action of external factors, including temperature, magnetic field, and hydrostatic pressure, revealed mechanisms consistent with the physical notions about the nature of interactions in the systems studied.

1. The experimental results showed equivalence of the anisotropic elastic stresses arising in response to an increase in the hydrostatic pressure by 1 kbar and in the temperature by 6.4 K, as manifested by equal changes in the resistivity of samples. This estimate indicates the role of the anisotropic thermoelastic stresses in the dynamics of properties and phase states.

2. A growth in the hydrostatic pressure by 1 kbar and an increase in the magnetic field strength by 2.37 kOe are also equivalent from the standpoint of anisotropic elastic straining of the sample structure, and they produce an equal decrease in the resistivity of samples. This estimate characterizes the magnetostrictive anisotropic elastic stresses in the structure, which are also responsible for the giant magnetoresistance effect.

3. The dynamics of properties, their anisotropy, and phase states predetermined by the chemical bonds and the symmetry of the sample structure is controlled by the interplay of two thermodynamic parameters—temperature and pressure. A mechanism based on the development of anisotropic elastic stresses in the structure is proposed which relates the thermodynamic parameters to the properties and describes the dynamics of properties and phase states in magnetic semiconductors.

Acknowledgments. The authors are grateful to N.P. Boiko for his interest in this investigation and constant attention.

REFERENCES

1. V. M. Loktev and Yu. G. Pogorelov, Fiz. Nizk. Temp. **26**, 231 (2000) [Low Temp. Phys. **26**, 171 (2000)].
2. F. Mascarenhas, K. Falk, P. Klavins, *et al.*, J. Magn. Magn. Mater. **231**, 172 (2001).
3. N. Fujii, R. Zach, M. Ishiruka, *et al.*, J. Magn. Magn. Mater. **224**, 12 (2001).
4. V. Moshnyaga, S. Klimm, V. Samwer, *et al.*, J. Appl. Phys. **88**, 5305 (2000).
5. S. S. Kucherenko, V. I. Mikhaĭlov, V. P. Pashchenko, *et al.*, Pis'ma Zh. Tekh. Fiz. **27** (15), 38 (2001) [Tech. Phys. Lett. **27**, 638 (2001)].
6. S. S. Kucherenko, V. P. Pashchenko, P. I. Polyakov, *et al.*, Fiz. Nizk. Temp. **27**, 761 (2001) [Low Temp. Phys. **27**, 559 (2001)].
7. S. S. Kucherenko, V. P. Pashchenko, P. I. Polyakov, *et al.*, Pis'ma Zh. Tekh. Fiz. **27** (11), 24 (2001) [Tech. Phys. Lett. **27**, 451 (2001)].
8. V. P. Pashchenko, S. I. Khartsev, and O. P. Cherenkov, Neorg. Mater. **35**, 1294 (1999).
9. A. V. Oleĭnik, P. I. Polyakov, and V. G. Synkov, Fiz. Tekh. Vys. Davleniĭ **4**, 88 (1994).
10. A. A. Galkin, S. V. Ivanova, V. I. Kamenev, and P. I. Polyakov, Fiz. Tverd. Tela (Leningrad) **21**, 2580 (1979) [Sov. Phys. Solid State **21**, 1486 (1979)].
11. I. V. Medvedeva, K. Barner, G. H. Rao, *et al.*, Physica B (Amsterdam) **292**, 250 (2000).

Translated by P. Pozdeev

Technical Physics Letters, Vol. 28, No. 4, 2002, pp. 315–317. Translated from Pis'ma v Zhurnal Tekhnicheskoĭ Fiziki, Vol. 28, No. 8, 2002, pp. 18–23.

Use of Topographic Data for the Study of Evolution of the Strain Distribution on a Material Surface in the Course of Plastic Deformation

S. A. Mineev, O. A. Morozov, and O. V. Semenova

Physicotechnical Research Institute, Nizhni Novgorod State University, Nizhni Novgorod, Russia

e-mail: sov@nifti.unn.ru

Received October 15, 2001

Abstract—A method is proposed for experimentally determining the inhomogeneous distribution of strain over the surface of plastically deformed material on a mesoscopic scale. The experimental results for lead samples are presented. © *2002 MAIK "Nauka/Interperiodica".*

Introduction. Investigations of the evolution of the function of strain distribution over the surface of plastically deformed solids at a resolution comparable to the average size of structural inhomogeneities (mesoscopic scale) mostly employ contactless methods such as holographic and speckle interferometry [1] or methods based on pattern recognition [2]. Below we describe an alternative experimental method for evaluation of the distribution of strain on a sample surface using the topographic data. This approach offers certain advantages in comparison to the traditional methods.

The information about all components of the strain tensor on the sample surface in the course of deformation is reflected by changes in the material's surface relief. It is suggested that experiments on the plastic deformation of solids would involve direct monitoring of the surface topography of a sample in various stages of the process. At present, there are numerous methods and techniques for obtaining topographic images of the sample surface in a broad range of spatial resolution (from microns to centimeters).

According to the proposed approach, the investigation has to include the following steps: (i) selecting and marking a working region on the sample surface; (ii) scanning the surface profile in the region of reference marks; (iii) repeated cycles of loading the sample followed by profile scanning, continued until reaching a preset deformation stage or fracture; (iv) preliminary processing (noise filtration, trend removal, centering with respect to reference marks); and (v) restoration of the strain distribution over the sample surface using profiles measured in the adjacent stages of deformation. Most of these steps falls within the framework of the standard scheme of determining the strain fields on the sample surface, except for the numerical restoration procedure [3], which is a basis of the proposed method.

Theory. It was experimentally established that plastic strain is inhomogeneously distributed over the sample surface. In the one-dimensional case, the strain of a kth region on the sample surface can be represented in the following form:

$$\varepsilon^k = \frac{l^k - l_0^k}{l_0^k}, \tag{1}$$

where l_0^k is the linear size of the kth element (region) of the surface prior to straining and l^k is that after the action. It is assumed that strain is linear within each element and only the extension or contraction of each region along the X axis is taken into account.

The coordinates of each count (point) on the primary profile after straining are as follows:

$$\begin{cases} X_0 = 0, \\ X_{i+1}^k = X_i^k(1 + \varepsilon_k), \quad 0 \le i < m - 1, \end{cases} \tag{2}$$

where k is the number of a region on the surface profile, ε_k is the relative strain of the kth region, and m is the number of points within the kth region of the profile. Once an array of the profile height f and an array of the coordinates corresponding to these heights after straining are available, we can use a special interpolation procedure to construct a model of the strained surface profile. It was established that acceptable results can be obtained with the aid of a cubic spline interpolation procedure.

A correct construction of the model of a strained surface profile opens a way to solving the problem of restoration of the strain distribution on the sample surface by iterative methods. The proposed restoration algorithm is based on the procedure of multidimensional optimization of a function of the rms mismatch between the strained surface profile and that constructed from the unstrained profile by solving the

1063-7850/02/2804-0315$22.00 © 2002 MAIK "Nauka/Interperiodica"

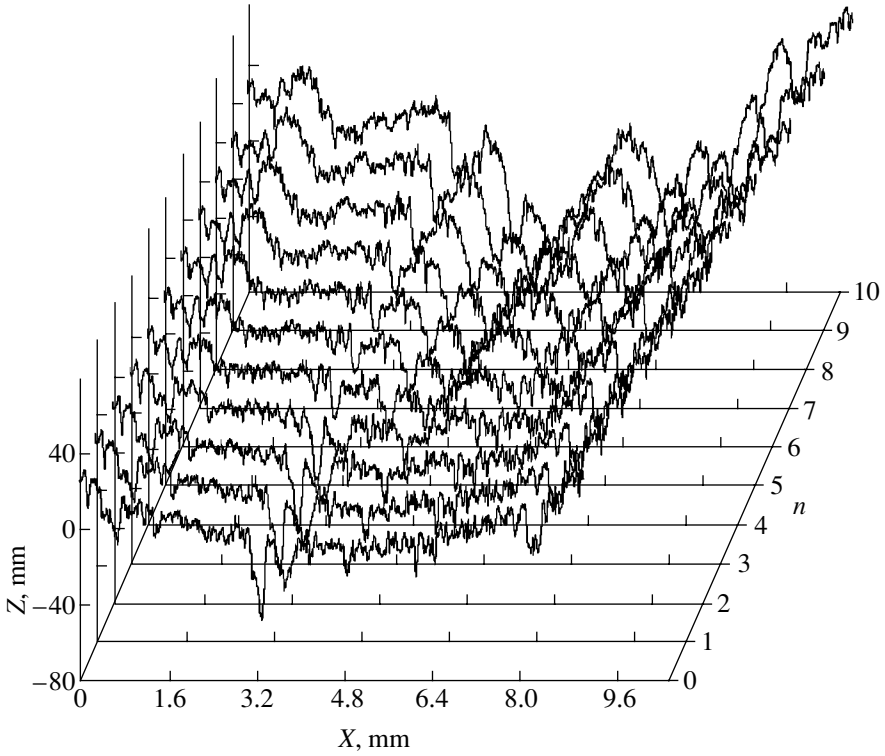

Fig. 1. Evolution of the surface profile in the same region of a sample in the course of plastic deformation (*n* is the loading cycle number).

direct problem based on a certain estimate of the strain distribution by the Monte Carlo method:

$$P(\varepsilon) = \frac{\sum_{l=0}^{N-1} (f'_l - \tilde{f}'_l[\varepsilon, f])^2}{\sum_{l=0}^{N-1} f'^2_l}, \quad (3)$$

where f is the unstrained surface profile, f' is the profile upon straining, $\tilde{f}'$ is the model of the strained surface, ε is the estimate of the inhomogeneous strain distribution function, and $P(\varepsilon)$ is a multidimensional polymodal function (the coordinate vector of the global minimum of this function represents the required estimate of the strain distribution).

Experiment. The tests were performed with a standard dumbbell sample of lead possessing the working part dimensions $19 \times 7 \times 3$ mm. The sample was manufactured by melt crystallization in an open mold and quenched in liquid nitrogen immediately upon solidification of the melt. The material was quenched in order to refine the grain size and provide for a more uniform stress distribution over a working region. The working region selection was determined by the presence of a small pit (which served as a stress concentrator) on the rear side of the sample. In selecting the working region, we also took into account the future neck formation and fracture of the sample. This region was marked with the aid of a spherical steel indentor, by drawing two lines perpendicular to the axis of tension and bounding a 10-mm-long working region.

The one-dimensional surface profiles were obtained by scanning the sample surface with a profilograph-profilometer mounted on a shock-absorbing base. The measuring unit output was connected to a voltage amplifier, the informative signal of which was digitized and used for further processing. Specially developed software allowed the profile scanned by the probe to be monitored and the next scan to be initiated (terminated) upon reaching the initial (final) mark. The characteristic semicircle surface profile at the mark allowed the initial and terminal scan points to be unambiguously determined. The loading–scanning cycles were repeated until the neck formation stage, which yielded 11 surface profiles scanned between marks on various stages of the sample deformation.

The sample was loaded *in situ* in the scanning profilometer with the aid of a specially designed electromechanical device. The loading device was capable of extending the sample with minimum transverse displacements relative to the axis of tension. The mobile sample holder velocity was 10 cm/min. Every time the holder moved 1 mm, the loading was terminated by switching off the drive, the sample was allowed to equilibrate for 1 min, the surface profile was scanned, and the probe returned to the initial position at a veloc-

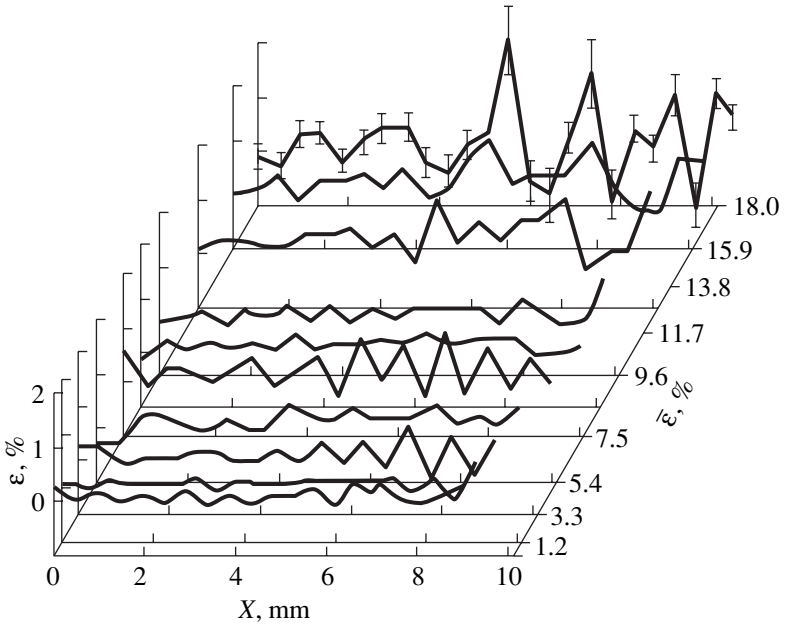

Fig. 2. Evolution of the one-dimensional strain distribution over the surface of a plastically deformed lead sample.

ity of 60 mm/min. Since the loading device contained no blocking mechanism (i.e., no stretching force acts upon the holder after switching off the drive), the results of measurements represented the residual strain of the sample.

The scanning device possessed certain features which introduced specific distortions in the form of noise and trends. These distortions were compensated on the digital processing stage. After this correction, the regions between marks were separated and used as the initial data for the restoration of strain distribution over the sample surface. Figure 1 shows the evolution of the surface profile measured in the same surface region of a sample in the course of deformation (digital processed surface profiles). The procedure of restoring the strain distribution was performed using the surface profiles obtained in the adjacent deformation stages. The results of these calculations are presented in Fig. 2.

It was established that, upon solving the problem of multidimensional optimization, the probability of realization of the strain distribution function on each portion of the surface profile measured at a fixed loading step obeys with a good precision the normal distribution law, which allows the confidence interval to be calculated for each determination of the strain distribution. The standard deviations are indicated by error bars on one of the strain distribution profiles in Fig. 2 (the bars on the other curves are omitted).

The experimental results revealed a correlation between estimates of the strain distribution and the macroscopic effects: the neck formation and the subsequent fracture took place in the region of maximum scatter of the strain distribution function on the sample surface. However, the direct relationship between these phenomena was not confirmed and, hence, this question requires further investigation.

Conclusion. The proposed method requires no preliminary treatment of the sample surface and can be used for the investigation of the structure evolution in the course of deformation of any material on an arbitrary spatial and temporal scale, based on the data obtained by both contact and contactless measuring techniques. The only restriction is that the surface profiles on the adjacent deformation stages have to be correlated. Experimental verification confirmed the possibility of constructing quantitative estimates for the evolution of the strain distribution over a solid surface using the topographic data obtained by mechanical profilometry.

REFERENCES

1. *Handbook on Experimental Mechanics*, Ed. by A. S. Kobayashi (Prentice-Hall, Englewood Cliffs, 1987; Mir, Moscow, 1990), Vol. 1.
2. V. E. Panin, V. E. Egorushkin, *et al.*, *Physical Mesomechanics and Computer Designing of Materials* (Nauka, Novosibirsk, 1995), Vol. 2.
3. S. A. Mineev, O. A. Morozov, O. V. Sotnikova, and Yu. Yu. Gushchina, Poverkhnost, No. 7, 96 (2000).

Translated by P. Pozdeev

Technical Physics Letters, Vol. 28, No. 4, 2002, pp. 318–319. Translated from Pis'ma v Zhurnal Tekhnicheskoĭ Fiziki, Vol. 28, No. 8, 2002, pp. 24–27.

A Theory of the Bulk Trapping of Particles into a Channeled Transport Mode

V. P. Koscheev

Surgut State University, Surgut, Russia

e-mail: koscheev@surgu.wsnet.ru

Received September 24, 2001

Abstract—A theory describing the bulk trapping of heavy relativistic particles into a channeled transport mode is constructed. It is demonstrated that a discrete character of the atomic plane potential in a bent crystal explains the elastic energy losses for the transverse motion of channeled particles, which exceed the inelastic losses for the same motion by a factor of 10^7. © *2002 MAIK "Nauka/Interperiodica".*

The main principles of the theory of bulk trapping into a channeled mode (BTCM) for particles moving in a crystal were formulated by Sumbaev [1]. It was established that protons can be trapped into the channeled mode, provided that the elastic energy losses for the transverse motion of channeled particles exceed the corresponding inelastic losses by a factor of 10^7.

The elastic energy losses for the transverse motion of particles in bent channels of a crystal are represented by two terms. One of these is related to the multiple scattering of particles on the thermal oscillations of atoms in the crystal and on quantum fluctuations of the positions of atomic electrons. The influence of this term upon the BTCM dynamics was originally studied by methods of computer simulation [2] and by solving the Fokker–Planck equation [3]. The second term, which accounts for the elastic energy losses of particles moving in the bent crystal channels, is related to a discrete character of the atomic plane potential. The purpose of this study was to construct a BTCM theory that would take into account the contributions due to both these terms.

The channeled particles move in the electric potential of a crystal, representing a sum of the Coulomb potentials of atomic nuclei occupying the crystal lattice sites and the Coulomb potentials of electrons in the atomic shells:

$$U(r) = \sum_n \left(\frac{Ze^2}{|\mathbf{r} - \mathbf{r}_n|} - \sum_{j=1}^{Z} \frac{e^2}{|\mathbf{r} - \mathbf{r}_{nj}|} \right), \qquad (1)$$

where Ze is the charge of the atomic nucleus, $\mathbf{r}_n = \mathbf{r}_{n0} + \delta\mathbf{r}_n$ ($\delta\mathbf{r}_n$ is a vector determining the position of the nth nucleus displaced from the lattice site due to thermal oscillations), $\mathbf{r}_{nj} = \mathbf{r}_{n0} + \delta\mathbf{r}_n + \delta\mathbf{r}_{nj}$ ($\delta\mathbf{r}_{nj}$ is a vector determining the position of the jth electron relative to the nth atomic nucleus), and $\mathbf{r}_{n0}$ determines the position of the nth crystal lattice site.

Averaging over the independent thermal oscillations of atoms in the crystal is performed with the aid of the Gauss distribution function. Averaging over the quantum fluctuations of the positions of atomic electrons is carried out using the method [4] employed by Bethe for calculating the atomic form factor. These averaging procedures, conducted with respect to the coordinates of all nuclei and all electrons, are denoted by symbols $\langle \ldots \rangle_T$ and $\langle \ldots \rangle_e$, respectively.

The crystal field potential can be represented in the following form:

$$U(r) = \bar{U} + \delta U_z(r) + \delta U(r), \qquad (2)$$

where $\bar{U} = \bar{U}(x)$ is the continuous potential of a planar channel in the crystal, averaged over the thermal oscillations of atoms; $\delta U_z(r) = \langle U \rangle_{e,T} - \bar{U}$ is a correction to the continuous potential related to the discrete arrangement of atoms on the axis or in the plane (this term is not a source of fluctuations); $\delta U(r) = U(r) - \langle U \rangle_{e,T}$ is the potential fluctuation caused by thermal oscillations of the atomic nuclei and by quantum fluctuations of the positions of atomic electrons.

The motion of high-energy charged particles in the bent crystal channels will be described by a stochastic equation of evolution of the transverse energy of particles constructed previously [5]:

$$\frac{d\varepsilon}{dt} = -\frac{2}{T(\varepsilon)} \int_{X_1(\varepsilon)}^{X_2(\varepsilon)} \frac{\partial}{\partial x}(\delta U + \delta U_z)\, dx, \qquad (3)$$

where $T(\varepsilon)$ is the period of oscillations for a particle moving in the planar channel and $X_{1,2}$ are the reversal points of the classical trajectory of the channeled particle, which can be determined from the equation $U_{\text{eff}}(X_{1,2}) = \varepsilon$. Here, U_{eff} is the effective potential of a

planar channel in the bent crystal, which has the following form:

$$U_{\text{eff}}(x) = \bar{U}(x) - \frac{pvx}{R},$$

where pv is the initial particle energy, R is the radius of crystal bending, $y = s\cos\phi$, $z = s\sin\phi$ (ϕ is an angle in the *YOZ* plane, which is far from the principal crystallographic directions), and $s \simeq vt$ is the depth of channeled particle penetration into the crystal.

As can be readily seen, it is the discrete character of the atomic plane potential in the bent crystal that accounts for nonconservation of the average energy for the transverse motion of channeled particles:

$$\frac{d\bar{\varepsilon}}{dt} = -\frac{2}{T(\bar{\varepsilon})}\{\delta U_z[X_2(\bar{\varepsilon}), t] - \delta U_z[X_1(\bar{\varepsilon}), t]\}. \quad (4)$$

This equation contains a small parameter representing the ratio of a distance between atoms in the crystal plane to a wavelength of the spatial oscillations of the particle in the planar channel. Using the multiscaling method [6], Eq. (4) can be converted to the following form,

$$\frac{d\bar{\varepsilon}}{dt} = -\frac{2}{T(\bar{\varepsilon})}\{\bar{U}[X_2(\bar{\varepsilon})] - \bar{U}[X_1(\bar{\varepsilon})]\}, \quad (5)$$

and then written as

$$\frac{d\bar{\varepsilon}}{ds} = -\frac{2pv}{R\lambda_{\text{ch}}}[X_2(\bar{\varepsilon}) - X_1(\bar{\varepsilon})], \quad (6)$$

where $\lambda_{\text{ch}} = vT(\bar{\varepsilon})$ is the wavelength of the spatial oscillations of a particle moving in the planar channel of the bent crystal.

Now we can use Eq. (6) and obtain an estimate for the elastic losses of the transverse energy of particles channeled in the bent crystal:

$$\left|\frac{d\bar{\varepsilon}}{ds}\right|_{\text{el}} \simeq \frac{2pv\Psi_L}{R\pi}, \quad (7)$$

where Ψ_L is the Lindhard critical channeling angle [7]. The last formula was derived assuming that $X_2(\bar{\varepsilon}) - X_1(\bar{\varepsilon}) \simeq d_p$ and $\lambda_{\text{ch}} \simeq \pi d_p/\Psi_L$ (d_p is the interplanar spacing). The inelastic losses of the transverse energy of particles channeled in the bent crystal are estimated as [1]

$$\left|\frac{d\bar{\varepsilon}}{ds}\right|_{\text{inel}} \simeq \Psi_L^2\rho, \quad \text{MeV/cm}, \quad (8)$$

where ρ is the crystal density (g/cm^3).

For protons with energies in the range from 1 GeV to 10 TeV channeled in a silicon crystal, the Lindhard critical angle falls within $\Psi_L \simeq 10^{-4}$–10^{-6} rad [1]. The critical value of the ratio $(pv/R)_{\text{cr}} \simeq 5$ GeV cm^{-1} for a silicon crystal was estimated from the condition that the centrifugal force is equal to the maximum Coulomb force with which the crystal atomic plane acts upon the channeled particle [8]. As can be readily seen from these estimates, the elastic energy losses for the transverse motion of channeled particles, determined by formula (7), exceed the inelastic losses for the same motion, described by formula (8), by a factor of not less than 10^7, which is in complete agreement with the requirement of the BTCM theory [1].

REFERENCES

1. O. I. Sumbaev, Zh. Tekh. Fiz. **57** (11), 2067 (1987) [Sov. Phys. Tech. Phys. **32**, 1251 (1987)].
2. A. M. Taratin and S. A. Vorob'ev, Zh. Tekh. Fiz. **55** (8), 1598 (1985) [Sov. Phys. Tech. Phys. **30**, 927 (1985)].
3. N. A. Kudryashov, S. V. Petrovskiĭ, and M. N. Strikhanov, Zh. Tekh. Fiz. **59** (4), 68 (1989) [Sov. Phys. Tech. Phys. **34**, 422 (1989)].
4. H. A. Bethe, *Intermediate Quantum Mechanics* (W. A. Benjamin, New York, 1964; Mir, Moscow, 1965).
5. V. P. Koshcheev, Pis'ma Zh. Tekh. Fiz. **27** (18), 61 (2001) [Tech. Phys. Lett. **27**, 784 (2001)].
6. A. H. Nayfeh, *Introduction to Perturbation Techniques* (Wiley, New York, 1981; Mir, Moscow, 1984).
7. J. Lindhard, Usp. Fiz. Nauk **99** (2), 249 (1969).
8. V. M. Biryukov, V. I. Kotov, and Yu. A. Chesnokov, Usp. Fiz. Nauk **164** (10), 1017 (1994) [Phys. Usp. **37**, 937 (1994)].

Translated by P. Pozdeev

Technical Physics Letters, Vol. 28, No. 4, 2002, pp. 320–322. Translated from Pis'ma v Zhurnal Tekhnicheskoĭ Fiziki, Vol. 28, No. 8, 2002, pp. 28–33.

A Hydrogen-Sensitive Structure Based on Semi-Insulating Gallium Arsenide

I. A. Karpovich, S. V. Tikhov, E. L. Shobolov, and B. N. Zvonkov

Nizhni Novgorod State University, Nizhni Novgorod, Russia

e-mail: fdp@phys.unn.ru

Received November 16, 2001

Abstract—The response characteristics of a simple hydrogen-sensitive structure based on semi-insulating single crystal gallium arsenide with planar palladium electrodes deposited onto the oxidized substrate surface are studied. It is demonstrated that such structures exhibit a fast response to hydrogen present in the gas phase. The sensitivity can be increased by growing, prior to the electrode formation, an intermediate epitaxial GaAs film with built-in strained quantum-confined layers of InGaAs and InAs onto the semi-insulating GaAs substrate. © *2002 MAIK "Nauka/Interperiodica".*

Hydrogen-sensitive semiconductor transducers are usually created using metal–insulator–semiconductor structures (capacitors, field-effect transistors, or Schottky diodes based on single crystal Si or GaAs layers) with catalytically active Pd electrodes [1]. These sensors are fabricated by a rather complicated technology and require an additional heating device, since satisfactory response characteristics are reached at 80–100°C.

Below we describe a simple hydrogen-sensitive structure based on a semi-insulating single crystal gallium arsenide substrate with a pair of closely spaced planar palladium electrodes. In a microelectronic device, one or both interdigital comblike metal electrodes can simultaneously perform as resistive heaters. We also present the results of investigation of the response characteristics of these hydrogen sensors.

The sample structures were based on semi-insulating single crystal gallium arsenide (s-GaAs) substrates. Prior to depositing palladium electrodes, the substrate was heated in air at 300°C for 30 min in order to form a thermal oxide layer with a thickness of about 3 nm. Finally, two square (1×1 mm) Pd electrodes spaced by ≈30 μm were formed on the oxidized s-GaAs substrate surface by thermal deposition in vacuum. The thickness of a semitransparent Pd electrode film was about 20 nm. In some structures, an additional epitaxial film of undoped GaAs with a thickness of ~0.5 μm was grown on the semi-insulating substrate and three quantum wells (QWs) or a quantum dot (QD) layer were built into a subsurface region of this GaAs layer [2]. The methods of obtaining heterostructures with QWs and QDs are described in [3, 4].

The effect of hydrogen on the electric and photoelectric properties of structures was studied using samples placed in the flow of an air–argon mixture containing hydrogen at a concentration C_H of up to 0.6 vol % [5]. The measurements were performed at a temperature of 100°C which was preliminarily established to provide for the best sensor characteristics.

The heterostructures obtained represent two inversely connected Schottky diodes with a common base of a semi-insulating material in the gap. The results of preliminary measurements showed that, provided the semi-insulating gap between Pd electrodes is sufficiently thin, the resistance of the base region at 100°C can be ignored. The structures possess a symmetric current–voltage characteristic typical of a reverse-biased GaAs Schottky diode. The current I is proportional to the applied voltage V for $V \le 1$ V; as the applied voltage increases above this level, the relation changes to $I \sim \sqrt{V}$ and then (about 10 V) the reverse

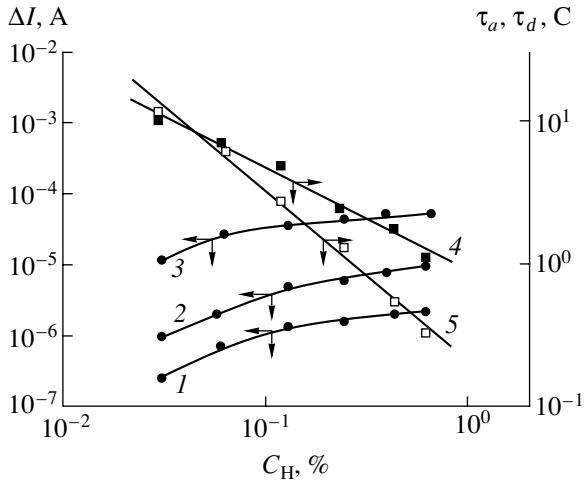

Fig. 1. The plots of (*1–3*) current increment ΔI and (*4, 5*) characteristic relaxation times τ_a and τ_d, respectively, versus hydrogen concentration in air for the sample structures with (*1, 4, 5*) plane s-GaAs substrate and with epitaxial GaAs films containing (*2*) quantum wells or (*3*) quantum dots.

1063-7850/02/2804-0320$22.00 © 2002 MAIK "Nauka/Interperiodica"

current exhibits a buildup usually related to the avalanche breakdown.

Exposed to a hydrogen-containing atmosphere, the sample structures show an increase in current. The current increment ΔI characterizing the device sensitivity with respect to hydrogen was initially proportional to the content of hydrogen at small concentrations C_H and exhibited saturation at large C_H (Fig. 1, curves *1*–*3*). The ΔI value was proportional to the applied voltage up to the breakdown threshold and dropped sharply if the voltage exceeded this level. Such a drop was followed by an irreversible change in the current and by a decrease in the sensitivity with respect to hydrogen. No irreversible changes were observed for the applied voltage below 10 V. For $C_H = 0.6\%$, the maximum relative change in the current $\Delta I/I$ (observed at the end of the current–voltage characteristic part corresponding to the law $I \sim \sqrt{V}$) reached about one order of magnitude.

The mechanism of sensitivity to hydrogen in the structures studied, as well as in the usual diode sensors, is related to the catalytic effect of palladium [1]. Indeed, no such sensitivity was observed for analogous structures with tin electrodes or with palladium electrodes on unoxidized s-GaAs substrates. The structures with undoped epitaxial GaAs films showed the same sensitivity to hydrogen as the structures on s-GaAs substrates. At the same time, the sensitivity of structures with QWs or QDs was much higher than that of the samples with undoped GaAs layers: the increase was more than tenfold in the case of QDs. The hydrogen detection threshold of the structures with QWs and QDs increased to the same extent (reaching 10^{-3} vol %). This can be explained by the fact that the strained quantum-confined layers, representing an additional potential barrier [3], retard the diffusion of hydrogen inward the GaAs volume; in addition, it was found that the QWs and QDs built into the subsurface region of GaAs decrease the barrier at the Pd–GaAs interface.

The hydrogen detection threshold of the proposed structures, despite being somewhat lower as compared to that (~10^{-4} vol % [5]) of the Schottky diodes based on conducting GaAs, is quite sufficient for alarm systems detecting explosive concentrations of hydrogen in the environment (~4%) and for leak detectors. An important characteristic of hydrogen sensors for such applications is the response speed—and the proposed structures meet sufficiently high requirements in this respect. Since the kinetics of current relaxation observed for a pulsed action of hydrogen was not exponential, the response speed was described in terms of the times of signal ascent (τ_a) and decay (τ_d) to half of the initial stationary level, characterizing the rate of hydrogen adsorption and desorption, respectively. Figure 1 (curves *4* and *5*) shows the plots of these quantities versus hydrogen concentration C_H. As can be seen,

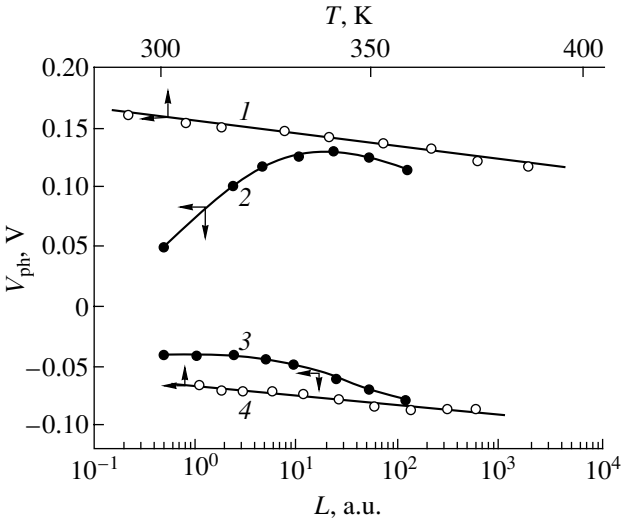

Fig. 2. The plots of photovoltage V_{ph} versus (*2*, *3*) illumination intensity L and (*1*, *4*) temperature T. The measurements were performed (*1*, *2*) in air and (*3*, *4*) in a hydrogen-containing atmosphere ($C_H = 0.6\%$).

the characteristic times vary from 10 to 0.1 s, decreasing with increase in the hydrogen concentration so that $\tau_a \sim C_H^{-1}$ and $\tau_d \sim C_H^{-1/2}$.

In order to elucidate the mechanism of hydrogen action upon the sensor structure, we have measured the photovoltage (V_{ph}) developed between the illuminated Pd electrode and an ohmic contact (Sn) deposited onto the rear side of the substrate. Figure 2 shows the plots of V_{ph} versus illumination intensity (L) and temperature. For the structure illuminated in air (curve *2*), the sign of the photoresponse ($V_{ph} > 0$) corresponds to a diffusion-barrier mechanism of the photovoltage generation with an upward band bending at the Pd/s-GaAs interface. However, the photovoltage amplitude was two to three times lower as compared to that in Pd/*n*-GaAs junctions with conducting GaAs layers ($n \sim 10^{16}$ cm^{-3}) and decreased further even for relatively small illumination intensities (curve *2*), probably due to the electron trapping on the surface traps [6].

In a hydrogen-containing atmosphere with $C_H = 0.6\%$, the photovoltage changed sign (curve *3*). This behavior is naturally explained by positive charging of the oxide/s-GaAs interface as by chemisorbed atomic hydrogen [7]. In contrast to the case of samples exposed to air, where the photovoltage linearly decreases (in agreement with the theory) with an increase in the temperature (Fig. 2, curve *1*), the negative photovoltage developed in the presence of hydrogen increased with the temperature (curve *4*), probably due to the catalytic effect of palladium [1].

Thus, simple but sufficiently effective hydrogen-sensitive structures with fast response can be fabricated on semi-insulating GaAs substrates. These structures can be used in leak detectors and hydrogen alarm sys-

tems. The semi-insulating GaAs substrate allows the electrodes to be simultaneously employed as resistive heaters. The mechanism of hydrogen sensitivity is established, which is related to an increase in positive charging of the GaAs surface. The sensitivity with respect to hydrogen can be significantly increased by growing an additional epitaxial GaAs film containing built-in quantum-confined InGaAs and InAs layers.

Acknowledgments. This study was supported by the Russian Foundation for Basic Research (project no. 00-02-17598) and by the Federal Program "Russian Universities" (project no. 015.06.01.37).

REFERENCES

1. A. V. Evdokimov, M. N. Mushurudli, A. E. Rzhanov, *et al.*, Zarubezhn. Élektron. Tekh. **2** (321), 3 (1988).
2. N. N. Ledentsov, V. M. Ustinov, V. A. Shchukin, *et al.*, Fiz. Tekh. Poluprovodn. (St. Petersburg) **32** (4), 385 (1998) [Semiconductors **32**, 343 (1998)].
3. I. A. Karpovich, A. V. Anshon, and D. O. Filatov, Fiz. Tekh. Poluprovodn. (St. Petersburg) **32** (9), 1089 (1998) [Semiconductors **32**, 975 (1998)].
4. B. N. Zvonkov, I. A. Karpovich, N. V. Baĭdus', *et al.*, Fiz. Tekh. Poluprovodn. (St. Petersburg) **35** (1), 92 (2001) [Semiconductors **35**, 93 (2001)].
5. S. V. Tikhov, V. P. Lesnikov, V. V. Podol'skiĭ, *et al.*, Zh. Tekh. Fiz. **65** (11), 120 (1995) [Tech. Phys. **40**, 1154 (1995)].
6. V. A. Zuev, A. V. Sachenko, and I. B. Tolpygo, *Nonequilibrium Near-Surface Processes in Semiconductors and Semiconductor Devices* (Sov. Radio, Moscow, 1977).
7. V. I. Gaman, M. O. Duchenko, and V. M. Kalygina, Izv. Vyssh. Uchebn. Zaved., Fiz., No. 1, 69 (1998).

Translated by P. Pozdeev

Technical Physics Letters, Vol. 28, No. 4, 2002, pp. 323–324. Translated from Pis'ma v Zhurnal Tekhnicheskoĭ Fiziki, Vol. 28, No. 8, 2002, pp. 34–37.

Turbulent Mixing Development in a Thin Liquid Layer Accelerated by Compressed Air in a Closed Volume

E. E. Meshkov and N. V. Nevmerzhitskiĭ

Institute of Experimental Physics, Russian Federal Nuclear Center, Sarov, Russia

e-mail: root@gdd.vniief.ru

Received December 7, 2001

Abstract—It is demonstrated that a zone of turbulent mixing (TM) is developed at the unstable boundary of a thin liquid film accelerated by a hot compressed gas flow. When the TM zone reaches the opposite boundary, the film breaks into fragments and expands. As a result, the liquid film transforms into a layer comprising a dispersed liquid–gas mixture. The layer thickness increases with time and may be several dozens of times that of the initial liquid film. © *2002 MAIK "Nauka/Interperiodica".*

Some cumulative systems intended for attaining high energy densities employ relatively thin heavy layers separated by light (gas) spacers [1]. The heavy layers in such systems move with acceleration, and one of the boundaries of each layer always exhibits instability of the Rayleigh–Taylor type [2], the development of which leads to the appearance of a zone of turbulent mixing (TM). A finite strength of the heavy liquid layer, albeit presenting a stabilizing factor, cannot prevent the system from the instability onset and the TM development. The material strength only leads to the existence of a critical level of the amplitude and the wavelength of the initial perturbation, above which the initial perturbations exhibit unlimited growth [3]. As a result, conditions for the unconstrained development of instability may arise in the aforementioned systems [1] at a certain stage of the energy density buildup. This leads to violation of the energy accumulation process. In some other cases, a relatively thin liquid film may perform the protective function [4], under the conditions of which the TM may play a positive role.

In the previously reported experimental investigations devoted to the TM development on the unstable boundary of a liquid layer accelerated by compressed gas, the flow was only observed within a limited time during which the TM spreads over a part of the layer. Below we describe the results of an experiment in which the process of water layer breakage was monitored even after the time moment by which the TM zone originating on one boundary reached the opposite boundary.

In our experiment (Fig. 1), a 5-mm-thick layer of water was accelerated by strongly heated products of the explosion of an acetylene–oxygen gas mixture in a square (4 × 4 cm) vertical channel with transparent walls. Initially, the water layer was supported in the channel by a thin (~5 μm) Lavsan (Mylar) film. The explosive gas mixture was detonated by an electric spark initiated simultaneously at 64 points uniformly distributed over the channel cross section. The channel, in which the liquid layer was accelerated, had a blunt end (i.e., the process developed in a closed volume).

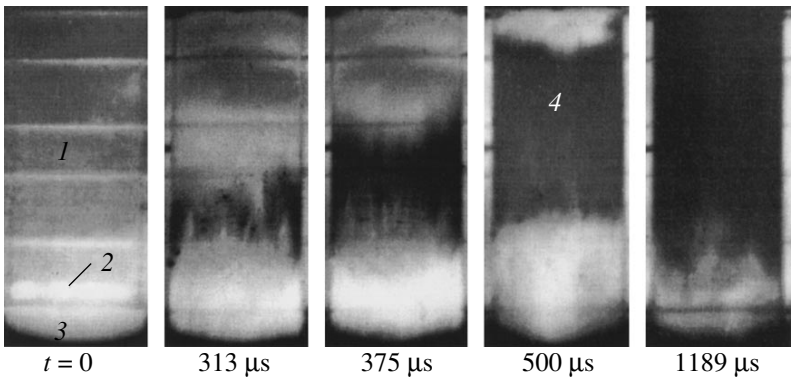

Fig. 1. A sequence of shots illustrating the fragmentation and expansion of a 5-mm-thick water film accelerated by the pressure of combustion products of an explosive ($C_2H_2 + 2.5O_2$) gas mixture in a square vertical channel: (*1*) air; (*2*) accelerated water layer; (*3*) explosive gas mixture; (*4*) dispersed water–air mixture. The current time *t* is measured from the onset of the layer motion.

1063-7850/02/2804-0323$22.00 © 2002 MAIK "Nauka/Interperiodica"

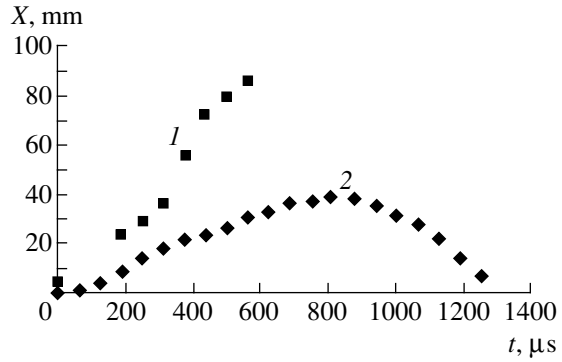

Fig. 2. The *X*–*t* diagrams for (*1*) the upper and (*2*) the lower boundaries of an expanding water layer accelerated by the pressure of combustion products of an explosive gas mixture.

The layer motion was monitored by a high-speed video camera.

In the course of acceleration, a TM zone appears and grows on the lower (unstable) boundary of the liquid layer [5]. In the developed TM zone, the gas penetrates into the liquid by forming a system of rounded "bubbles." The bubbles grow during penetration into the liquid. At the same time, the liquid penetrates into the gas in the form of streams. The streams breaks into small drops (forming a "rain") at the boundary of the TM zone.

When the propagating TM zone front reaches the external boundary of the liquid layer, the process of layer fragmentation and expansion continues. The scale and rate of this process is illustrated by a sequence of shots in Fig. 1 and by the corresponding coordinate–time (*X*–*t*) diagram (Fig. 2). Until $t = 400$–500 μs, the layer expansion proceeds with a certain acceleration, but then the process is decelerated due to the pressure of air compressed by the moving layer. By $t \approx 800$ μs, the compression wave reaches the lower boundary of the expanding layer; at this time instant, the layer starts moving in the reverse direction. This gives a new impact to the expansion process. By the end of the monitoring period, the layer thickness increases by a factor of ~20 as compared to that of the initial liquid film. As a result, the entire volume of the acceleration channel is filled with a dispersed water–gas mixture.

REFERENCES

1. G. Derentovich, Prikl. Mekh. Tekh. Fiz., No. 1, 23 (1989).
2. G. I. Taylor, Proc. R. Soc. London, Ser. A **201**, 192 (1950).
3. A. I. Lebedev, P. N. Nizovtsev, V. A. Rayevsky, *et al.*, in *Proceedings of the 5th International Workshop on Compressible Turbulent Mixing, Stony Brook, USA, 1995*, p. 231.
4. G. A. Ivanov, I. P. Voloshin, A. S. Ganeev, *et al.*, *Explosive Deuterium Power Engineering* (Snezhinsk, 1997).
5. I. G. Zhidov, E. E. Meshkov, and N. V. Nevmerzhitskiĭ, Preprint No. 56, FIAN (Lebedev Institute of Physics, Academy of Sciences of USSR, Moscow, 1990), p. 52.

Translated by P. Pozdeev

Technical Physics Letters, Vol. 28, No. 4, 2002, pp. 325–326. Translated from Pis'ma v Zhurnal Tekhnicheskoĭ Fiziki, Vol. 28, No. 8, 2002, pp. 38–41.

A Diffraction Trap for Neutrons in the Ångström Wavelength Range

T. Tchen

Moscow State Academy of Fine Chemical Technology, Moscow, Russia

e-mail: docent65@mtu-net.ru

Received July 16, 2001

Abstract—The penetration depth of thermal neutrons ($\lambda \sim 1$ Å) upon the Bragg backscattering in a bent crystal is estimated. It is demonstrated that neutrons incident onto the crystal at an angle close to the edge of the Bragg reflection curve can be accumulated inside and then (after 1–100 μs) ejected from the crystal.

Thermal neutrons with a wavelength of $\lambda \sim 0.1$–1 Å behave much like a rigid X-ray radiation exhibiting a dynamic diffraction from a crystal lattice. All parameters of the dynamic X-ray diffraction are valid for neutrons, except the absorption, which drops by more than three orders of magnitude. For this reason, crystals only a few centimeters thick can be used for trapping neutrons.

Consider the scattering of a neutron beam diffracted from a bent crystal with the curvature radius R in the plane of scattering (see the figure). From the geometric considerations, we obtain

$$t^2/\sin^2\theta = R^2 + (R+t)^2 - 2R(R+t)\cos\psi, \qquad (1)$$

where t is the crystal thickness and θ is the Bragg angle. Let us assume the angle ψ to be equal to the halfwidth of the Bragg reflection curve $\Delta\theta = |\chi_{hr}|/\sin 2\theta$, where χ_{hr} is the real part of the Fourier component of the crystal polarizability with respect to the neutron radiation.

Solving the above square equation with respect to t, we obtain that the thickness of the crystal layer involved in the Bragg diffraction reflection of neutrons is

$$t = [R(\Delta\theta)^2 + \{R^2(\Delta\theta)^4 + 4R^2\cot^2\theta(\Delta\theta)^2\}^{1/2}]/2\cot^2\theta. \qquad (2)$$

For the diffraction angles $\theta \neq \pi/2$, Eq. (2) yields

$$t \approx R(\Delta\theta)\tan\theta. \qquad (3)$$

For $R \sim 1$ m, $\Delta\theta \sim 10^{-6}$, and $\tan\theta \sim 2$, the corresponding layer thickness is $t \sim 2$ μm.

For the Bragg backscattering ($\theta \approx \pi/2$, $\cot\theta \approx \cos\theta \leq \theta$), the neutron penetration depth sharply increases to

$$t \approx \{(5)^{1/2} + 1\}R/2. \qquad (4)$$

For $R \sim 1$ m, this amounts to $t \sim 1.6$ m.

Formula (2), as well as estimates (3) and (4), do not take into account the effect of absorption. Evidently, the optimum crystal thickness in the case of backscattering is to be selected taking into account both the usual absorption and extinction.

As is known [1], the amplitude of neutron radiation (in the Ångström wavelength range) diffracted from the ideal plane crystal at a depth z is

$$E_h(z) = E_h(0)(-1)^m(1-\xi)^{z/d} \approx E_h(0)(-1)^m\exp(-k_{ext}z), \qquad (5)$$

where m is an integer, $k_{ext} = \xi/d = q(1-y^2)/d$ is the coefficient of extinction, q is the coefficient of reflection from a single plane, d is the interplanar spacing, and y is the normalized angular variable. Expression (5) can generalized so as to include the case of an elastically

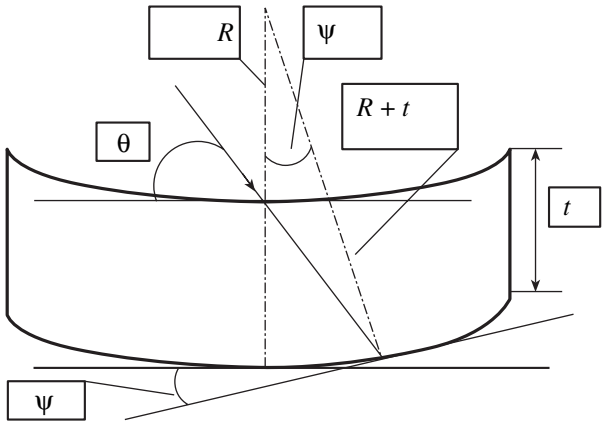

A schematic diagram illustrating the penetration of neutrons in the Ångström wavelength range into a bent crystal in the regime of dynamic Bragg diffraction.

1063-7850/02/2804-0325$22.00 © 2002 MAIK "Nauka/Interperiodica"

bent crystal. According to Eq. (5), the extinction length is

$$\Lambda \cong d/q(1-y^2)^{1/2}. \quad (6)$$

The extinction coefficient k_{ext} for an elastically bent crystal depends on the coordinate z, since the interplanar spacing d varies linearly in depth.

For neutrons incident onto the crystal at an angle close to the edge of the Bragg reflection curve ($|y| \approx 1$), the extinction length Λ significantly increases. Selecting the crystal thickness $t \geq 1$ cm $\sim \Lambda$ ($|y| \approx 1$), we can "trap" neutrons. The time T of holding neutrons in the crystal is

$$T \approx t/v, \quad (7)$$

where v is the neutron velocity. A numerical estimate for $\lambda \approx 1.5$ Å and $t \approx 1$ cm yields $T \approx 4$ μs.

By tilting the crystal within the limits of the reflection curve width, we can release the neutrons from the crystal upon elapse of time T. Such a crystal acts as a gate for neutrons with a characteristic lock time of $T \sim 1$–10 μs. Theoretically, this estimate can be increased by one to two orders of magnitude if we take $\lambda \leq 10$ Å and $t \sim 10$ cm.

We can estimate the effect of nonmonochromaticity of the neutron beam on the above estimate of the holding time T by using the uncertainty relationship in the form $\Delta E \Delta\tau \sim h$, where $E = h\nu$ is the neutron energy, ν is the frequency, h is the Planck constant, $\Delta\tau$ is the neutron lifetime in the crystal, $\Delta\nu/\nu = 2\Delta v/v$, and v is the neutron velocity. Let us assume the crystal size to be such that we may neglect the loss of neutrons as a result of multiple reflections from the side crystal faces. Setting $\Delta\tau \cong T$, $\lambda \cong 1.5$ Å, and $t \cong 10^{-1}$ m, we conclude that the incident neutron flux should be extremely monochromatic (monoenergetic): $\Delta v/v \sim 10^{-9}$. Such a supermonochromatic neutron beam can be "prepared," for example, using multiple reflection of thermal neutrons from reactor walls [2]. Note that the method proposed in [2] for the supermonochromatization of ultracold neutrons is applicable to cold neutrons as well.

Now we can demonstrate that, by focusing the neutrons leaving the crystal, it is possible to increase the neutron flux density. Let a thermal neutron flux with a density of $\Phi \sim 10^7$ neutron/(cm^2 s) be incident onto a crystal with dimensions $1 \times 1 \times 1$ cm. Note that the flux may be nonmonochromatic, containing the neutrons of various energies. Under these conditions, the crystal will accumulate $\sim 10^3$ neutrons over the time $T \sim 100$ μs. Assume that tilting the crystal near the Bragg angle allows 99% of the accumulated neutrons to escape. Then, by focusing the outgoing neutrons into a spot with dimensions $\sim 10 \times 10$ μm, we obtain a neutron density on the order of 10^7 neutron/cm^2, which is greater by four orders of magnitude than the density of neutrons incident onto the crustal.

REFERENCES

1. Z. G. Pinsker, *X-ray Crystal Optics* (Nauka, Moscow, 1982).
2. T. Tchen and R. N. Kuz'min, Pis'ma Zh. Tekh. Fiz. **17** (10), 51 (1991) [Sov. Tech. Phys. Lett. **17**, 371 (1991)].

Translated by P. Pozdeev

Technical Physics Letters, Vol. 28, No. 4, 2002, pp. 327–329. Translated from Pis'ma v Zhurnal Tekhnicheskoĭ Fiziki, Vol. 28, No. 8, 2002, pp. 42–47.

Field Electron Emitter for Air Ionization in a Supersonic Flow

S. V. Bobashev[a], Yu. P. Golovachev[a], O. P. Korovin[a], V. N. Shrednik[a], and D. Van Wie[b]

[a] *Ioffe Physicotechnical Institute, Russian Academy of Sciences, St. Petersburg, 194021 Russia*

[b] *Johns Hopkins University, Laurel, Maryland, USA*

Received December 17, 2001

Abstract—It is suggested to use a field electron emitter based on liquid gallium for the ionization of molecules in a supersonic air flow. © *2002 MAIK "Nauka/Interperiodica".*

In recent years, there has been active discussion concerning the possible application of magnetohydrodynamic (MHD) technologies with supersonic and hypersonic flows. In particular, a concept of the hypersonic jet plane for AWACS suggested a decade ago [1] was built around an MHD device capable of modifying the flow enthalpy and controlling the gasodynamic flow structures by means of magnetic field. However, the practical implementation of this approach encounters a number of physical and technical problems, each requiring special thorough investigation.

The results of recent experiments and calculations [2, 3] showed that magnetic field with a strength not exceeding 1 T can significantly influence the gasodynamic structure of a weakly ionized gas flow in laboratory models of supersonic diffusers. The experiments were performed in the flows of a weakly ionized heavy inert gas. An obvious advantage of inert gases in comparison to air or nitrogen is a low level of cross sections for the recombination of atomic ions, which allows the investigations to be conducted in laboratory gasodynamic setups. However, of most practical interest would be the study of MHD processes in supersonic flows of weakly ionized molecular gases, in particular, air and nitrogen. Here, the main problem consists in creating and maintaining for a sufficiently long time the degree of ionization required for significant MHD interaction.

These problems are actively and thoroughly discussed [4]. From the analysis, it follows that one of the most effective means of creating plasmas in molecular gases is ionization of the gas flow by an electron beam with an energy of 10–100 keV and a current density of 1–100 mA/cm^2. Thus, the task is to create a low-temperature plasma in a supersonic gas flow moving at a velocity of 1500–2000 m/s (Mach number, 4–6) and a static pressure of 0.01–0.1 atm (5–70 Torr). In order to change the flow enthalpy by several megajoules per kilogram at the expense of MHD interactions in reasonable magnetic fields (1–5 T), it is necessary to be able to maintain an electron density on the order of 10^{12}–10^{14} cm^{-3} in a volume of 1 m^3 by means of external ionization.

A nontrivial point in the problem under consideration is related to the methods of generating intense electron beams and introducing these beams into a supersonic flow. An analysis of the existing electron emitter systems shows that the use of incandescent cathodes is inefficient, since this implies a considerable energy consumption to provide for the necessary level of thermionic emission from large emitting surfaces. Moreover, the incandescent cathodes are very sensitive to vacuum conditions and are in most cases rapidly deteriorated upon contact with atmosphere.

Modern high-voltage cold (field) cathodes satisfying requirements of the problem under consideration are represented for the most part by single- and multipoint solid emitters operating in regimes of field emission or explosive (blow-up) emission [5]. Using such devices, it is possible to avoid considerable energy consumption required for the operation of incandescent cathodes. The level of voltages necessary for cathode operation in the field or an explosive emission mode corresponds to the values required for the optimum ionization of air in a gas flow. The current densities necessary for such ionization can be ensured by multipoint field cathodes, provided that the system of cathode points is characterized by the same height and curvature radius. A disadvantage of such systems is a high sensitivity to ion bombardment of the cathode points, which is especially pronounced at the level of air pressures required for MHD device operation. A disadvantage of the explosive emission mode is a relatively short lifetime of the cathode points, since each emission pulse conveys partial damage to the point and is accompanied by removal of the cathode material.

In our opinion, the most adequate solution to the problem is offered by a multipoint liquid-metal emitter based on melted gallium, in which a system of points is created with the aid of a nuclear membrane [6]. A schematic diagram of such emitter is presented in the figure. The device is based on a layer of liquid gallium, one

1063-7850/02/2804-0327$22.00

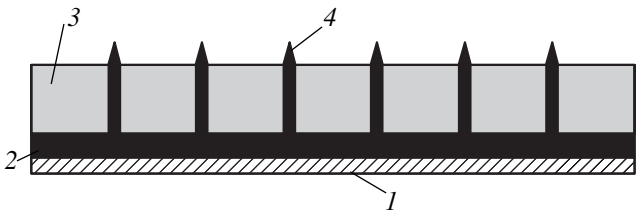

A schematic diagram of a liquid metal field emitter: (*1*) substrate; (*2*) liquid gallium layer; (*3*) track membrane; (*4*) liquid metal points.

side of which contacts with a current-carrying surface, while the other side is coated with a Mylar track membrane. The track membranes are obtained by irradiating the initial polymer film by heavy-ion beams of megaelectronvolt energy. The film thickness is typically about 10 μm. The diameter of track channels may vary within 0.3–1.0 μm, depending on the preparation conditions. The surface density of tracks (channels) in a membrane may reach up to 10^8 cm^{-2}. The emitter surface is determined by the polymer film area and can amount to several tens of square meters.

Upon application of the external voltage, the electric current is generated by the field-induced emission of electrons from liquid gallium points formed by the metal penetrating into capillaries of the track channels. A highly stable emissivity of each liquid metal point is provided by a deep negative feedback not admitting excessive sharpening of the metal points and infinite buildup of the emission current density. According to [6], the feedback is provided by the surface tension of the liquid metal, which tends to blunt the sharp tip of each point. On the other hand, a growth of the applied potential $U(t)$ leads to an increase in the electric field strength at the rounded end of each gallium column, thus extending and sharpening the emitter point. Eventually, the electric-field-induced pull-up pressure becomes equal to the pull-down pressure produced by the surface tension forces. This corresponds to the condition

$$\varepsilon_0 E_0^2/2 = 2\sigma/r_0, \quad (1)$$

where $\varepsilon_0 = 8.85 \times 10^{-12}$ F/m is the dielectric constant, E_0 is the equilibrium electric field strength [V/m], σ is the equilibrium surface tension [N/m], and r_0 is the equilibrium point radius [m].

Assuming that each emitter represents a body of revolution and the point end represents a spherical surface with the radius r_0, we can use the equilibrium condition (1) to obtain the estimate

$$E_0 = 5.7 \times 10^5 (r_0)^{-0.5}, \quad (2)$$

where the surface tension of liquid gallium is taken equal to $\sigma = 0.712$ N/m. According to formula (2), the point radii within 35–50 nm correspond to an electric field strength of $E_0 \geq 10^7$ V/cm. This is a very important estimate from the standpoint of introduction of the electron beam into a supersonic flow: in such a field, electrons are accelerated to an energy of about 10 keV over a distance of ~10 μm. Taking the emitter surface area equal to about $\sim r_0^2$, we can estimate the electron current I_0 from a singe point and (provided that the density of emitting points n [cm^{-2}] is known) determine the total current density as nI_0 [A/cm^2].

Up to now, liquid metal field emitters have been tested with various shapes of the applied voltage, including full sinusoid (with a frequency of 50 and 400 Hz and 50 kHz), half-sinusoid (with the same frequencies), constant voltage, and pulsed voltage (with a pulse duration of 100 ns and a repetition frequency of several kilohertz) [6]. Cathodes operating in the field emission mode allowed obtaining of the current densities up to 100 mA/cm^2. The parameters of field emitters calculated in terms of the Fowler–Nordheim theory with an allowance for the equilibrium of electric-field-induced pressure and surface tension in liquid gallium are presented in the table. The data include the electric field strength E, the electron emission current density J_{Ga}, the current I_0 from a single liquid metal point, and the total current density $I = I_0 n$ calculated assuming the point density $n = 10^7$ cm^{-2} for various equilibrium point radii r_0. As is known [7], a liquid metal point can provide for a stable current of not less than 10 μA in a continuous operation regime. Therefore, for the above point density (~10^7 cm^{-2}) on the emitter surface, the cathode can ensure a current density of up to 100 A/cm^2.

The parameters of a multipoint field emitter based on liquid gallium

r_0, nm	$E \times 10^{-7}$, V/cm	J_{Ga}, A/cm^2	$I_0 = j_{Ga} \times r_0^2$, A	$I = I_0 n$, A/cm^2
10	5.7	1.9×10^7	1.9×10^{-5}	190
20	4.0	2.1×10^5	8.4×10^{-7}	8.4
30	3.35	7.6×10^3	6.9×10^{-8}	0.69
40	2.84	4.9×10^2	7.9×10^{-9}	0.079
50	2.5	4.5×10^1	1.14×10^{-9}	0.0114

In concluding, we indicate the properties of multipoint field emission cathodes based on liquid gallium which, in our opinion, are important for the ionization of molecular gases under supersonic flow conditions. A cathode operating in the field emission or explosive emission mode can generate stable reproducible electron beams of kiloelectronvolt energies with a current density reaching up to several hundred amperes per square centimeter. The high stability and reproducibility of the cathode operation are related to the fact that the field emission regime is self-sustained due to the reliable negative feedback based on equilibrium between the electric-field-induced forces and the liquid metal surface tension. The density of the current gener-

ated by each single point is sufficiently low to maintain the stable field emission process. A considerable total current density is ensured by a large number (10^7–10^8 cm^{-2}) of simultaneously operating emission points. In this system, there is no problem with leveling the point parameters (as is the case with solid emitters), since the properties of liquid metal points are self-leveling. By the same token, the defects (accumulated to bring a problem in the case of solid emitters) exhibit self-healing on the surface of liquid metal points. In the regime of explosive emission, liquid metal emitters are capable of operating for a long time with a pulsed current strength of up to several hundreds of amperes at a pulse duration within 30–100 ns and a repetition frequency variable from 1 Hz up to several kilohertz (the tested emitters operated for many hours without any visible changes in the parameters of emission). Stable operation is provided by the ability of emitting points to self-recover after each explosion current pulse.

As noted above, an electric field of high strength created in the emission region near the point surface drives electrons to acquire a kilovolt energy over a distance of a few microns. This circumstance offers a new approach to the problem of introducing an electron beam into a supersonic gas flow. The emitting surfaces of field cathodes of the type under consideration may possess various shapes and considerable dimensions.

Now we are planning to study the properties of multipoint gallium film emitters operated under conditions corresponding to the injection of kiloelectronvolt beams into supersonic air flows in MHD channels.

REFERENCES

1. V. L. Fraishtadt, A. L. Kuranov, and E. G. Sheikin, Zh. Tekh. Fiz. **68** (11), 43 (1998) [Tech. Phys**. 43**, 1309 (1998)].
2. S. V. Bobashev, R. V. Vasil'eva, E. A. D'yakonova, *et al.*, Pis'ma Zh. Tekh. Fiz. **27** (2), 63 (2001) [Tech. Phys. Lett. **27**, 71 (2001)].
3. Yu. P. Golovachev, S. A. Il'in, and S. Yu. Sushchikh, Pis'ma Zh. Tekh. Fiz. **23** (16), 1 (1997) [Tech. Phys. Lett. **23**, 615 (1997)].
4. S. O. Macheret, M. N. Shneider, R. B. Miles, and R. J. Lipinski, AIAA J. **39** (6), 1127 (2001).
5. *Nonincandescent Cathodes*, Ed. by M. I. Elinson (Sov. Radio, Moscow, 1974).
6. O. P. Korovin, E. O. Popov, V. N. Shrednik, and S. S. Karatetskiĭ, Pis'ma Zh. Tekh. Fiz. **25** (8), 39 (1999) [Tech. Phys. Lett. **25**, 310 (1999)].
7. G. N. Fursey, L. A. Shirochin, and L. M. Baskin, J. Vac. Sci. Technol. **15** (2), 410 (1997).

Translated by P. Pozdeev

Technical Physics Letters, Vol. 28, No. 4, 2002, pp. 330–332. Translated from Pis'ma v Zhurnal Tekhnicheskoĭ Fiziki, Vol. 28, No. 8, 2002, pp. 48–53.

The Formation of Excited Chlorine Atoms in a Low-Pressure Transverse Volume Discharge

A. K. Shuaibov, A. I. Dashchenko, and I. V. Shevera

Uzhgorod National University, Uzhgorod, Ukraine

e-mail: ishev@univ.uzhorod.ua

Received December 11, 2001

Abstract—The characteristics of a transverse volume discharge (TVD) in chlorine at low pressures ($P(Cl_2)$ = 0.1–1.5 kPa) were studied. The excited chlorine atoms were formed in a $18 \times 2.2 \times (0.5–1.0)$ cm volume using relatively low values of the capacitor bank charging voltage ($U_{ch} \le 10$ kV) in the pulsed discharge voltage source. The optical emission from plasma was studied in a spectral range from 500 to 900 nm. Homogeneous TVD pulses of short duration ($\tau \le 100$ ns) obtained under these conditions are of interest for use in UV–VUV lamps employed in pulsed plasmachemical reactors for dry etching of thin films. The density of excited atomic chlorine radicals can be monitored on medium-resolution spectrometers using the ClI emission lines with λ = 725, 754, and 821 (2) nm. © *2002 MAIK "Nauka/Interperiodica".*

The pulsed volume discharge in chlorine at low pressure is of considerable interest for the development of high-power short-wavelength spontaneous radiation sources operating on the electron-vibrational transitions in Cl_2 molecules [1, 2]. This discharge can be also employed for the dry etching of thin coatings in pulsed plasmachemical reactors analogous to the reactors pumped with a transverse volume discharge (TVD) in fluoromethane [3].

The problem of *in situ* monitoring the plasmachemical processes and detecting the time of termination of the process of dry etching of nanometer- thick films can be solved based on the thorough plasma diagnostics and the chlorine radical density control in the course of etching [4]. For this purpose, the plasma in reactors employing RF-pumped low-pressure discharge in halogen-containing gases is frequently probed by methods of optical spectroscopy. This approach requires knowledge of the optical characteristics of a particular reactor plasma. The most intense emission lines of chlorine atoms, which can be used for monitoring the chlorine radical density in the course of etching, occur in the near IR range [5]. Our previous study [2] of radiation from a TVD plasma in chlorine and a He–Cl_2 gas mixture referred to the spectral range from 140 to 280 nm and revealed a purely molecular character of the emission. The optical characteristics of chlorine plasmas in the region of a longer wavelength remained uninvestigated.

Below we report on the conditions ensuring a homogeneous transverse discharge in chlorine and present the results of a spectroscopic investigation of the formation of excited chlorine atoms, the decay of which is accompanied by emission in the IR wavelength range.

The TVD was confined within a volume of $18 \times 2.2 \times$ (0.5–1.0) cm between electrodes spaced by 2.2 cm. The interelectrode gap preionization was provided by automated two-side spark discharge. The pulsed discharge voltage generator employed a scheme with a capacitor C_0 = 10 nF recharging via a shaping capacitor bank with a total capacitance of C_1 = 9.4 nF.

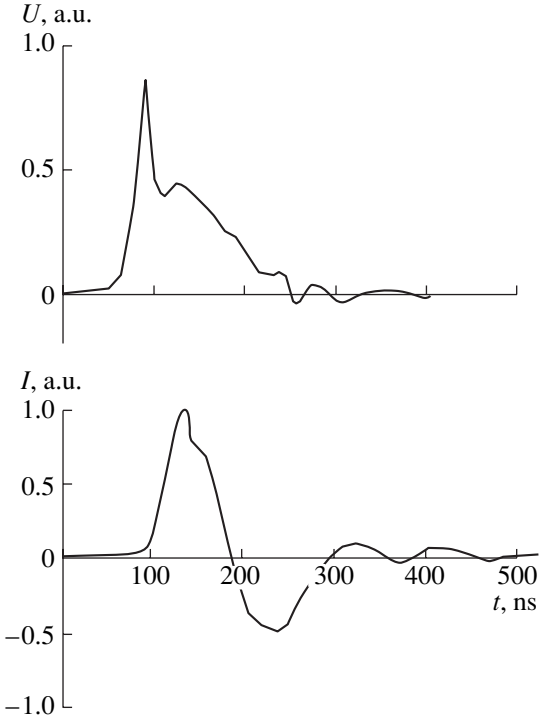

Fig. 1. Oscillograms of discharge voltage and current for TVD in chlorine at $P(Cl_2)$ = 0.40 kPa and U_{ch} = 7.5 kV.

1063-7850/02/2804-0330$22.00 © 2002 MAIK "Nauka/Interperiodica"

The commutation was provided by a hydrogen thyratron of the TGI-I 1000/25 type. The charging voltage U_{ch} could be varied from 5 to 10 kV. The discharge modulus design and the system used for monitoring electrical characteristics of the TVD were described elsewhere [6–8]. The spectral lines and bands were assigned using tabulated data [9–11]. The TVD radiation was studied in the spectral range from 500 to 900 nm. The measured radiation spectra were corrected for the relative spectral sensitivity of an MDR-2 monochromator equipped with a 600 strokes/mm grating and a FEU-106 photomultiplier tube. The radiation detection system was calibrated with the aid of a band lamp. Superposition of an intense second-order molecular emission from chlorine in the UV range was rejected by a filter transmitting at $\lambda \geq 500$ nm.

A homogeneous transverse discharge was stably initiated for $U_{ch} \geq 5$ kV in the interval of chlorine pressures from 0.1 to 1.5 kPa. As the chlorine pressure was increased, the TVD width decreased from 1.0 to 0.5 cm. Figure 1 shows typical oscillograms of the interelectrode voltage and the TVD current. The discharge current profile exhibited positive and negative half-waves with a duration ≤100 ns each. The current arose after breakdown of the discharge gap at the maximum of the discharge voltage and was maintained provided interelectrode voltage was sufficiently large. Oscillograms of the interelectrode voltage and the current of TVD in chlorine were similar to those observed for a pulsed volume discharge in elegas [12–14]. The E/N ratio corresponding to a quasi-stationary part of the voltage oscillogram (τ = 100–250 ns, Fig. 1), observed at a number density of chlorine atoms of $\approx 6 \times 10^{17}$ cm^{-3}, was 100–300 Td (while a stable regime of the dc glow discharge plasma corresponds to E/N = 3 Td [15, 16]).

Figure 2 shows the emission spectra of TVD plasma in chlorine. In the region of 500 nm ≤ λ ≤ 700 nm, the spectrum exhibits a system of molecular bands on a weak continuum background; some of these bands can be assigned to the emission from Cl_2^+ ions (λ = 539.6 and 569.3 nm [9]) and Cl_2 molecules. In the region of 700–900 nm, the spectrum displays dominating lines of emission from chlorine atoms, representing the ClI (4*s*, 4*s*'–4*p*, 4*p*') system of transitions. The relative intensities of emission for these transitions in chlorine atoms are summarized in the table. An increase in the chlorine pressure up to 1.5 kPa led to the intensity of ClI spectral lines growing by a factor of 1.5–5.0 and the intense emission lines of chlorine appearing in the region of $\lambda \geq$ 900 nm; this was accompanied by an increase in the contribution of emission from the molecular ions Cl_2^{+*} and excited molecules Cl_2 in the wavelength interval from 500 to 700 nm.

The character of the observed emission spectrum significantly differed from that reported for the plasma of a dc glow discharge in chlorine [17]. The latter spectrum contained the lines of emission from chlorine atoms only at λ = 725, 741, and 755 nm and exhibited no molecular emission structure in the 540–700 nm range.

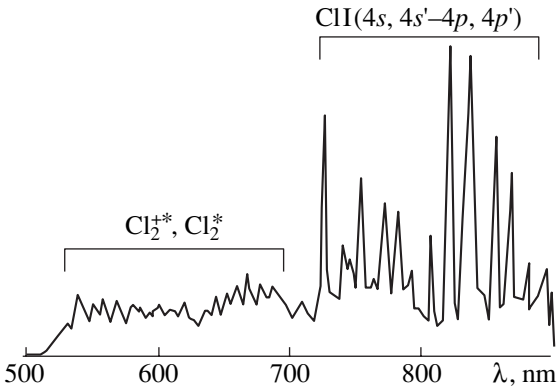

Fig. 2. The emission spectrum of a low-pressure TVD plasma in chlorine.

The ClI emission line intensities in the near IR range for the TVD plasma in chlorine at a pressure of P = 0.40 kPa and a charging voltage of U_{ch} = 7.5 kV

λ, nm	Excited level	E_h, eV	J/k_λ, a.u.
868.(6)	$4p^4 S^0_{3/2}$	10.63	0.90
858.(5)	$4p^4 D^0_{5/2}$	10.43	0.85
857.(5)	$4p^4 D^0_{3/2}$	10.47	
842.(8)	$4p^4 D^0_{7/2}$	10.50	0.45
837.(5)	$4p^4 D^0_{7/2,\,3/2}$	10.40	1.00
833.(3)		10.47	
822.(1)	$4p^2 D^0_{5/2}$	10.49	0.80
821.(2)	$4p^4 D_{5/2}$	10.43	
808.(7) 808.(6) 808.(5) 808.(4)	$4p'^2 D^0_{3/2,\,5/2}$	11.96	0.25
793.(2)	$4d(2)_{9/2}$	11.96	0.10
792.(1)	$4p^2 P^0_{3/2}$	10.59	
782.(1)	$4d(2)_{7/2}$	11.86	0.25
774.(4)	$4p^4 S^0_{3/2}$	10.63	0.25
771.(7)	$4p^2 P^0_{3/2}$	10.59	0.25
754.(7)	$4p^4 S^0_{3/2}$	10.63	0.30
741.(4)	$4p^2 P^0_{3/2}$	10.59	0.10
725.(6)	$4p^4 S^0_{3/2}$	10.63	0.40
708.(6)	$6s(2)_{5/2}$	12.06	<0.05

Thus, we have established that, at a moderate capacitor charging voltage (U_{ch} = 5–10 kV), a homogeneous plasma is formed in the low-pressure TVD in chlorine (0.1–1.5 kPa). The emission spectrum of this plasma is of interest for use in pulsed plasmachemical reactors for dry etching. The density of excited atomic chlorine radicals in the plasma can be monitored using the ClI emission lines with λ = 725, 754, and 821 (2) nm, measured with spectrometers possessing a medium resolution on the order of 1 nm.

REFERENCES

1. L. M. Vasilyak, S. V. Kostenko, A. V. Krasnochub, *et al.*, Teplofiz. Vys. Temp. **33** (6), 826 (1995).
2. A. K. Shuaibov, Zh. Tekh. Fiz. **70** (10), 117 (2000) [Tech. Phys. **45**, 1346 (2000)].
3. Yu. D. Korolev, G. A. Mesyats, and A. M. Yarosh, Khim. Vys. Énerg. **21** (5), 464 (1987).
4. A. A. Orlikovskiĭ and K. V. Rudenko, Mikroélektronika **30** (2), 85 (2001).
5. B. S. Danilov and V. Yu. Kireev, *Application of Low-Temperature Plasma for Etching and Cleaning of Materials* (Énergoatomizdat, Moscow, 1987).
6. A. K. Shuaibov, Kvantovaya Élektron. (Moscow) **26** (2), 127 (1999).
7. O. K. Shuaibov, L. L. Shimon, I. V. Shevera, and A. J. Minja, J. Phys. Stud. **3** (2), 157 (1999).
8. A. K. Shuaibov, L. L. Shimon, I. V. Shevera, and A. I. Dashchenko, Fiz. Plazmy **25** (7), 640 (1999) [Plasma Phys. Rep. **25**, 585 (1999)].
9. R. W. B. Pears and A. G. Gaydon, *The Identification of Molecular Spectra* (Chapman and Hall, London, 1963).
10. *Spectroscopic Data*, Vol. 2: *Homonuclear Diatomic Molecules*, Ed. by S. N. Suchard and J. E. Melzer (IFI/Plenum, New York, 1976).
11. A. P. Striganov and G. A. Odintsova, *Tables of Spectral Lines of Atoms and Ions: Handbook* (Moscow, 1982).
12. G. L. Spichkin, Zh. Tekh. Fiz. **56** (10), 1923 (1986) [Sov. Phys. Tech. Phys. **31**, 1150 (1986)].
13. Yu. I. Bychkov, S. A. Gorchakov, and A. G. Yastremskiĭ, Izv. Vyssh. Uchebn. Zaved., Fiz., No. 8, 43 (1999).
14. V. V. Appolonov, A. A. Belevtsev, S. Yu. Kazantsev, *et al.*, Kvantovaya Élektron. (Moscow) **30** (3), 207 (2000).
15. A. V. Gorokhov, A. I. Maksimov, V. D. Sizov, and L. S. Stepanova, Zh. Tekh. Fiz. **42** (10), 2176 (1972) [Sov. Phys. Tech. Phys. **17**, 1717 (1972)].
16. A. P. Kupriyanovskaya, V. V. Rybkin, and V. I. Svettsov, Izv. Vyssh. Uchebn. Zaved., Khim. Khim. Tekhnol. **28** (3), 61 (1985).
17. A. M. Efremov, A. P. Kupriyanovskaya, and V. I. Svettsov, Zh. Prikl. Spektrosk. **59** (3), 221 (1993).

Translated by P. Pozdeev

Technical Physics Letters, Vol. 28, No. 4, 2002, pp. 333–335. Translated from Pis'ma v Zhurnal Tekhnicheskoĭ Fiziki, Vol. 28, No. 8, 2002, pp. 54–59.

Dynamic Effects during Thermoelastic Martensitic Transformations in TiNiCu Alloys

T. A. Shakhnazarov, I. K. Kamilov, Sh. M. Ismailov, and A. R. Bilalov

Institute of Physics, Dagestan Scientific Center, Russian Academy of Sciences, Makhachkala, Dagestan, Russia

e-mail: kamilov@datacom.ru

Received June 28, 2001

Abstract—Spontaneous periodic oscillations in the phase transformation rate during a system evolution toward a stationary state are observed in TiNiCu alloys. The conditions of manifestation and amplification of these oscillations are established and possible applications of this phenomenon are considered. © *2002 MAIK "Nauka/Interperiodica".*

Significant thermoelastic interactions manifested in alloys based on a TiNi intermetallic system are related to the thermal effect of the phase transformation reaction. For example, a high rate of the platelike martensite formation under the conditions of dominating shape memory effect [1] resulted in local heating and led to the formation of a thermal front, which served as a driving force of the reverse transition and was characterized by a certain delay. In the case of a plastic transformation, there must be a considerable mechanical contribution besides the thermal component of the phase transformation reaction. If such a process takes place under conditions hindering deformation of the material, the mechanical stress becomes dependent on the rate of the phase transformation. This provides for a possibility to trace the simultaneous action of the thermal and mechanical components on the phase transformation rate.

We have experimentally realized this situation using the rod-shaped samples of a TiNiCu alloy with a large length-to-diameter ratio (l = 60 mm, d = 2 mm). The necessary adiabaticity of the transformation process was ensured by thermal insulation of the rod with a vacuum jacket along the entire length of the working part. The oriented martensite plate growth along the rod was ensured by applying an initial tensile stress (≈100 MPa) and initiating the transformation at one end (reverse process) while cooling the other end (direct process). Under these conditions, it was possible to estimate the average velocity of the platelike martensite front propagation along the rod by determining the rate of the tensile stress variation. The tensile stresses were measured using a Model 2099P-5 test machine.

The results of experiments showed that, when the system was driven out of the stationary regime by applying external pulsed tensile stress, the direct martensitic transformation process exhibited periodic oscillations in the phase transformation rate (Fig. 1). A more detailed time pattern of the oscillatory parts of the curve (Fig. 2) revealed a rather significant duration of these oscillations. In the region of reverse martensitic transformation, the system could not be driven out of the stationary regime. This is explained by the shape memory effect that dominates under these conditions [2].

The observed periodic oscillations in the phase transformation rate represent nonmonotonic evolution of the thermodynamic system toward a stationary state. Under these conditions, dependence of the thermal fluxes on the thermodynamic forces acquires a nonlinear character and the theorem of minimum entropy production becomes inapplicable [3]. Here, the process of phase transformation obeys essentially the same laws as the process of relaxation of a large-scale fluctuation of the corresponding type. However, as noted in [4], the small-scale fluctuations also significantly contribute to some macroscopic characteristics and "participate" in the development of the irreversible process by influencing the energy dissipation.

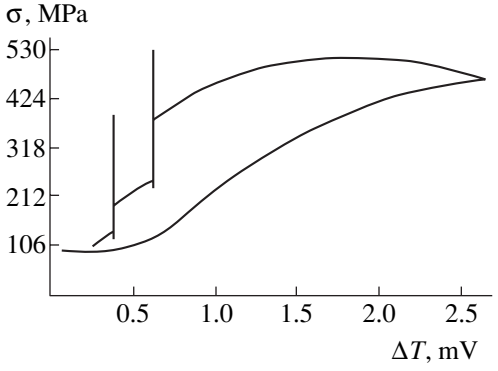

Fig. 1. A hysteresis loop of the thermoelastic martensitic transformation.

1063-7850/02/2804-0333$22.00 © 2002 MAIK "Nauka/Interperiodica"

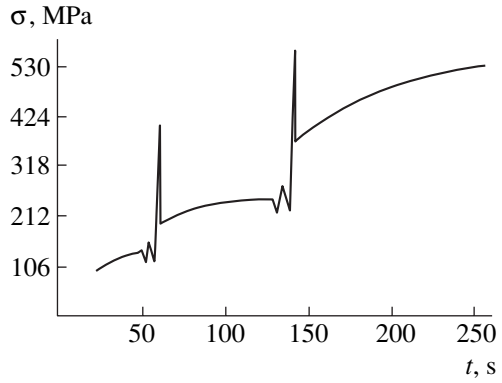

Fig. 2. Large-scale time variation of the stress level in the region of mechanical pulse action.

A solution to the equations describing the system perturbation is obtained in the complex form. The time variation of the oscillations is determined according to [3] by a complex quantity

$$\omega = \omega_r + i\omega_i, \tag{1}$$

where $i\omega_i$ is the imaginary part describing oscillations. The tie variation according to (1) is manifested when the stationary state is sufficiently far from the thermodynamic equilibrium, this distance being evaluated [3] by the chemical affinity $A > 9.2RT$. For the thermoelastic martensitic transformations, this distance must be determined relative to the state of thermoelastic equilibrium.

According to the model concepts developed in [5], we may consider the balance of forces acting upon a thermoelastic phase transformation:

$$X = \frac{\Delta\mu}{\varepsilon_s} - \sigma_i, \tag{2}$$

where $\Delta\mu = \Lambda(T - T_0)/T_0$ is the free thermodynamic force, Λ is the enthalpy of the phase transformation reaction, T_0 is the temperature of the phase equilibrium, T is the current temperature, σ_i is the internal stress field, and ε_s is the intrinsic deformation related to the transformation.

The rate of the thermoelastic martensitic transformation can be defined as

$$J = L\left(\frac{\Delta\mu}{\varepsilon_s} - \sigma_i\right). \tag{3}$$

Here, $J = \varepsilon_0/\varepsilon_s$ is the volume fraction of converted material, ε_0 is the microscopic deformation averaged over the ensemble of crystals (rather than the macroscopic plastic strain determined by the shape change of the whole sample in the course of the transformation, which is zero for a polycrystalline sample if we neglect the volume transformation effect), and L is the conductivity coefficient. Relationships (2) and (3), summed over the free thermodynamic force ($\Delta\mu$) and the force of constraint (σ_i), correspond to the Gauss principle of least constraint in the thermodynamic interpretation [6]. In these terms, the distance of a martensitic transformation process from the thermoelastic equilibrium can be measured by the quantity X: indeed, the process rate is zero ($J = 0$) for $X = 0$.

In the course of the direct and reverse thermoelastic martensitic transformation, the X value is determined by summing the external action with the thermal and mechanical components of the phase transformation reaction. The thermal component influences the $\Delta\mu$ value by changing the temperature in the reaction zone, while the mechanical component influences the σ_i value. The result of this interaction, determining the process rate, depends both on the rate of external action and on the differential rate of action of the thermal and mechanical components of the phase transformation reaction. The periodic oscillations in the phase transformation rate observed in our experiments take place on a certain level of the average process rate. This phenomenon is related to a difference in the rate of variation of the free thermodynamic force and the force of constraint and, hence, can be considered as a dynamic effect.

It should be noted that we are not considering the domain of effects corresponding to $A \longrightarrow \infty$, that is, to large transformation rates (nondecaying oscillations of the Lotk–Volter type, Zhabotinskii reaction, etc.). Here, we speak only of a nonmonotonic (oscillatory) evolution of a thermodynamic system toward a stationary state at a moderate rate of the transformation process. A practical significance of this phenomenon depends on how easily the system can be driven out of the stationary state. There are cases [7] when a phase transformation can be driven out of the stationary state by an external action with an amplitude lower by one order of magnitude than the amplitude of resulting oscillations. Such a high sensitivity [7], explained by increasing efficiency of the negative feedback, results in that periodic oscillations in the phase transformation rate are observed during the whole period of the phase transformation. In the case of thermoelastic martensitic transformations, increasing uncertainty of the reverse action of the process rate upon the free thermodynamic force and force of constraint can be achieved at the expense of increasing adiabaticity of the process, selecting compositions capable of higher inelastic strain, creating a mechanical stress gradient directed against the temperature gradient, and increasing the stress and temperature gradients.

The ability of alloys featuring thermoelastic martensitic transformations to be reversibly strained in a narrow (30–50 K) temperature interval allows these materials to be used for the reprocessing of low-potential thermal sources. This circumstance, in addition to the high relative exergy, makes other means of energy conversion uncompetitive. However, in order to provide for a sufficiently high transformation rate in real martensite

engines, it is necessary to create a certain initial overcooling below the temperature of the onset of the direct martensitic transformation and a sufficient overheating above the temperature of termination of the reverse transition. As a result, the real temperature interval increases to 250–300 K [8].

The thermoelastic martensitic transformations in a nonstationary oscillatory regime are accompanied by a violated linear relation between the thermodynamic driving force and the process rate. Under these conditions, the question of inertia of the system response can be omitted and the cyclic character of the process can be ensured without reaching complete martensitic transformation. This possibility can be realized by initiating the oscillatory process at the expense of large-scale fluctuations in the transformation rate, which are manifested upon jumplike variation in the martensite growth rate, whereby the plates reach up to a several microns in size within a single jump [9].

REFERENCES

1. V. É. Gyunter, V. I. Chernyshev, and T. L. Chekalin, Pis'ma Zh. Tekh. Fiz. **26** (4), 19 (2000) [Tech. Phys. Lett. **26**, 143 (2000)].
2. S. P. Belyaev, S. L. Kuz'min, V. A. Likhachev, and L. N. Shcherbakova, Fiz. Met. Metalloved., No. 1, 205 (1991).
3. P. Glansdorff and I. Prigogine, *Thermodynamic Theory of Structure, Stability and Fluctuations* (Wiley, New York, 1971; Mir, Moscow, 1973).
4. K. P. Gurov, *Phenomenological Thermodynamics of Irreversible Processes* (Nauka, Moscow, 1978).
5. A. G. Kosilov, Izv. Vyssh. Uchebn. Zaved., Fiz. **72** (5), 54 (1985).
6. I. Gyarmati, *Non-Equilibrium Thermodynamics* (Springer-Verlag, Berlin, 1970; Mir, Moscow, 1974).
7. G. A. Shakhnazarov, Zh. Fiz. Khim. **54** (1), 85 (1980).
8. S. P. Belyaev, S. L. Kuz'min, V. A. Likhachev, and V. V. Mozgunov, Available form VINITI No. 2427-85 (Leningrad, 1985).
9. M. P. Kashchenko, *Wave Model of the Martensite Growth during Transformation in Iron-Based Alloys* (Nauka, Yekaterinburg, 1993).

Translated by P. Pozdeev

Technical Physics Letters, Vol. 28, No. 4, 2002, pp. 336–339. Translated from Pis'ma v Zhurnal Tekhnicheskoĭ Fiziki, Vol. 28, No. 8, 2002, pp. 60–68.

A Fiber Optic Phase Modulator with an Optical Frequency Shift of up to 20 GHz

A. M. Mamedov, V. T. Potapov, and S. V. Shatalin

Fryazino Branch, Institute of Radio Engineering and Electronics, Russian Academy of Sciences, Fryazino, Moscow oblast, Russia

e-mail: mamedov@ms.ire.rssi.ru

Received November 23, 2001

Abstract—A fiber optic phase modulator is described in which the phase of a light wave traveling in an optical fiber is modulated by a composite electromechanical resonator with $Q \cong 1000$. The instantaneous frequency of the wave at the modulator output varies according to a harmonic law. The interval of tuning of the instantaneous light wave frequency achieved in the experiment is 20 GHz, which corresponds to a modulation index of $\cong 10^6$. It is demonstrated that a maximum value of the frequency tuning range is determined by the elastic limit of the resonator material. © *2002 MAIK "Nauka/Interperiodica".*

Numerous applications of tunable lasers include optical frequency domain reflectometry (OFDR) [1] (which has inspired this study), integral optical device testing [2], photodetector calibration [3], etc. The OFDR procedure involves a linear sweep of the light wave frequency, after which the beats between reference and scattered waves contain various spectral components uniquely corresponding to various parts of a tested line or a passive multiplex network of fiber optic sensors. However, existing tunable semiconductor lasers have the minimum bandwidth of several hundred kilohertz, thus restricting the tested range to a few hundred meters [1].

An alternative to direct modulation was represented by an electrooptical modulator [4] in which the source emitted a fixed frequency and the modulation was performed behind the source. This approach requires using a high-rate processing system with a frequency band of a few gigahertz, since the optical wave frequency shift equals the frequency of the electric modulation signal. Another disadvantage of this scheme was the presence of modulation harmonics leading to nonlinear second-harmonic distortions of the photocurrent beat signal.

Previously [5], we proposed a scheme of the fiber optic modulator in which the phase of a light wave propagating in the fiber was changed by extending a part of this fiber coiled around a piezoceramic cylinder. This solution is intrinsically compatible with single-mode fiber optic devices and is wavelength-independent, which makes it applicable to any type of light sources. In addition, this scheme is free from the problem of harmonics and requires no wideband electronic processing system (because of a low resonance frequency of the piezoceramic cylinder ($\cong$25 kHz)). A disadvantage of this modulator scheme is a low resonator quality factor ($Q \cong 25$) for which the frequency tuning in a sufficiently wide range (4 GHz) is achieved at the expense of considerable power (8 W) that is dissipated in the modulator.

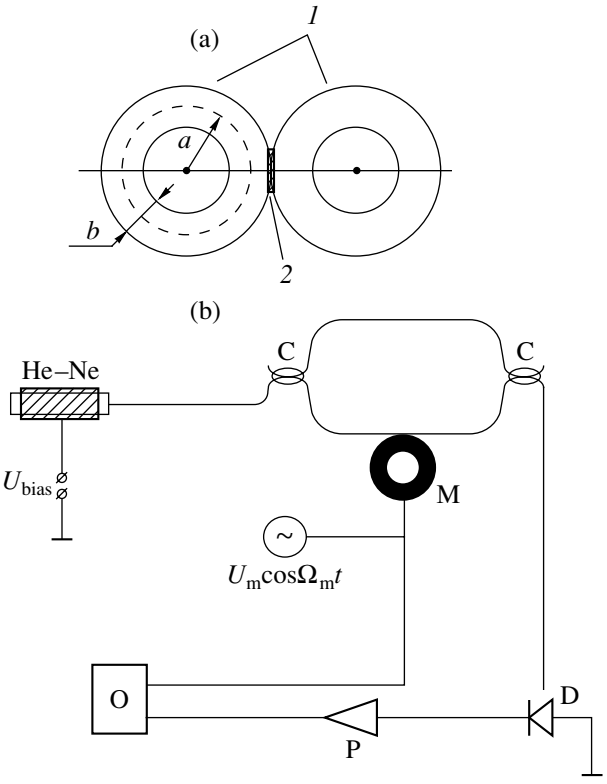

Fig. 1. Schematic diagrams showing (a) the top view of a composite electromechanical resonator (*1*, bronze cylinder; *2*, piezoelectric transducer) and (b) the experimental setup: (D) photodiode; (C) fiber couplers; (M) fiber optic phase modulator; (O) oscillograph; (P) amplifier.

1063-7850/02/2804-0336$22.00 © 2002 MAIK "Nauka/Interperiodica"

Below we describe a fiber optic phase modulator based on a composite resonator (Fig. 1a) around which about 300 m of a single-mode optical fiber was wound.

Theory. In order to study the light wave frequency modulation, we used a double-beam interferometer scheme (Fig. 1b). In the case of a source with two longitudinal modes, the photocurrent i is determined by the interference of four waves:

$$i \approx \langle ra_1\cos\omega t + ra_2\cos(\omega t + \Delta\omega t) + a_1t^2\cos(\omega t + \varphi) + a_2t^2\cos(\omega t + \Delta\omega t + \varphi)\rangle^2, \quad (1)$$

where r and t are the amplitude reflection and transmission coefficients of the interferometer; a_1 and a_2 are the longitudinal mode amplitudes; φ is the phase increment; ω is the cyclic frequency of the light wave; and $\Delta\omega = 2\pi\Delta\nu$ is the mode spacing (angle brackets denote time average).

Let the interferometer include a phase modulator such that $\varphi = \varphi_m\cos(\Omega_m t)$. Under the condition $\varphi_m \gg 1$, expression (1) reduces to

$$i(t) = G[\Omega(t)] \times \left\{A\cos\int_0^t \Omega(t)dt + B\cos\int_0^t [\Omega(t) \pm \Delta\omega]dt\right\}, \quad (2)$$

where $\Omega(t) = \varphi_m\Omega_m\sin\Omega_m t$ is the instantaneous frequency; $A = rt^2(a_1^2 + a_2^2)$ and $B = rt^2a_1a_2$ are the beat amplitudes. The coefficient of proportionality in Eq. (2) represents a spectral response $G[\Omega(t)]$ of the photodetector at the instantaneous frequency. For simplicity, the constant component of the photocurrent is omitted, which is equivalent to assuming $G(0) = 0$.

In the case of single-mode laser operation ($a_2 = 0$ and $B = 0$), an amplitude-modulated wave is incident onto the photodetector. The modulation frequency of this wave exhibits periodic variations from 0 to $\Omega_{max} = \varphi_m\Omega_m$. At the time instants such that $\Omega_m t \ll 1$, the frequency is modulated according to a linear law and the photocurrent envelope is

$$\bar{i}(t) \cong \frac{A}{2}G(\Omega_{max}\Omega_m t). \quad (3)$$

This expression is of practical interest for determining the amplitude–frequency characteristics of photodetector structures: the photocurrent envelope displayed on the oscilloscope visualizes the frequency response of the photodetector.

A convenient means of calibrating the phase modulator is offered by a double-mode laser operation ($a_1 = a_2$, $B \neq 0$). In this case, the photodetector measures the beats not only near the points of zero frequency, but at the time instants τ for which $\Omega(\tau) = \Delta\omega$ as well. Thus, we can readily determine the light wave frequency deviation as

$$\Omega_{max} = \frac{\Delta\omega}{\sin\Omega_m\tau}. \quad (4)$$

Let us analyze the factors determining the range of frequency deviation. The phase modulation index φ_m and, hence, the range of instantaneous frequency deviation Ω_{max} are proportional to the fiber strain amplitude. Denoting by Δl be the strain amplitude of the fiber half-turn, we obtain

$$\Omega_{max} = \frac{4\pi n}{\lambda}N\Omega_m\Delta l, \quad (5)$$

where N is the number of turns, λ is the radiation wavelength, and n is the refractive index of the fiber core.

Proceeding from the general considerations, we expect that the resonator oscillation amplitude and, hence, the fiber strain Δl can be controlled by three parameters: (i) the elastic limit of the fiber; (ii) the power transmitted to the composite resonator; and (iii) the elastic limit of the resonator material. The elastic limit of the fiber is reached only for a relative fiber strain on the order of 1% [1]. This level of dynamic straining can be attained only in metallic glasses or in a specially treated beryllium bronze.

An analysis of the latter two parameters shows that, similar to the case of a piezoceramic modulator [5], the main factor limiting the strain amplitude in a low-Q resonator is the transmitted power. However, the situation will principally change for a resonator possessing very high Q, in which the strains corresponding to the elastic limit can readily be achieved. Let us consider this case in more detail.

For a cylindrical modulator operating on the principal bending mode, one can readily check that [6]

$$\Delta l = \frac{4}{3}\frac{\sigma}{E}\frac{r_0^2}{d}, \quad (6)$$

where σ is the elastic strain amplitude, E is the elastic modulus of the modulator material, r_0 is the cylinder radius, and d is the cylinder wall thickness. Formula (6) is derived under the assumption that the cylinder wall thickness d is small as compared to the radius r_0. Therefore, all subsequent expressions will also refer to the case of a thin-walled cylinder.

The principal bending mode frequency of a thin-wall cylinder is given by the formula [6]

$$\Omega_m \cong 0.48\frac{d}{r_0^2}\sqrt{\frac{E}{\rho}}, \quad (7)$$

where ρ is the modulator material density. Using formulas (5)–(7), we readily obtain an expression relating

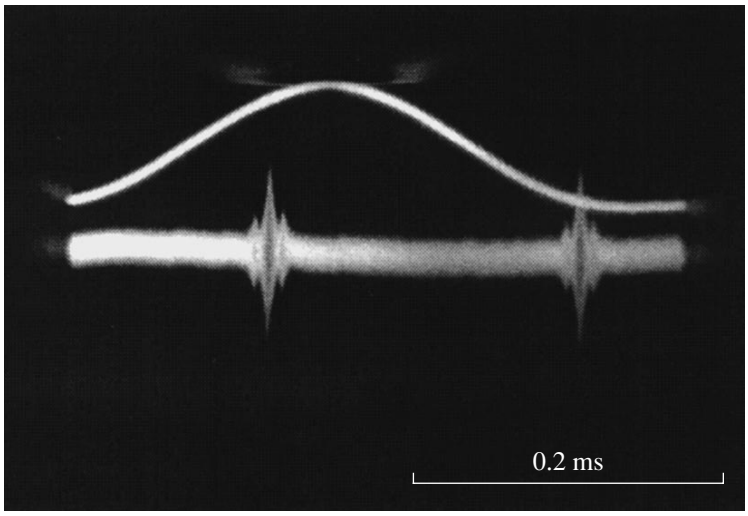

Fig. 2. Oscillograms of the photodetector signal observed in a double-mode lasing regime.

the instantaneous frequency deviation to the physicochemical parameters of the modulator material:

$$\frac{\Omega_{max}}{2\pi} = 1.28\frac{n}{\lambda}N\sqrt{\frac{\sigma^2}{E\rho}}. \quad (8)$$

The term under square root sign in Eq. (8) has a physical meaning of the specific elastic energy stored per unit mass of the strained element. Therefore, this relationship implies that the range of the instantaneous frequency deviation is determined by the elastic modulus E, modulator material density ρ, and elastic stress σ. In practice, the maximum possible elastic stress σ is determined by the elastic limit σ_{el} of the modulator material. Exceeding this limit leads to violation of the Hooke law, whereby the oscillator becomes nonlinear and the system escapes from resonance. As is known [7], the $\sqrt{\sigma_{el}^2/\rho E}$ value is maximum for copper-based alloys. In addition, there is a specially developed commercial technology of thermal treatment that additionally increases the $\sigma \geq \sigma_{el}$ value by more than one order of magnitude.

In order to determine the transmitter power, we have calculated the mechanical energy U stored in the strained resonator using the explicit form of the principal bending mode:

$$U = \frac{13}{16}M\Omega_m^2 S^2. \quad (9)$$

Here, M is the cylinder mass, Ω_m is the resonance frequency, and S is the maximum amplitude of the cylinder bending oscillations. At the same time, the oscillation amplitude S is related to the frequency tuning range $\nu_{max} = \Omega_{max}/2\pi$ by the following expression:

$$S = \frac{\nu_{max}\lambda}{4N\Omega_m n}. \quad (10)$$

Using Eqs. (9) and (10) together with a formula for the transmitted power, $P = \Omega_m U/Q$, we obtain an expression for the frequency deviation range:

$$\nu_{max} = \frac{16Nn}{\lambda}\sqrt{\frac{PQ}{M\Omega_m}}. \quad (11)$$

As can be seen from this expression, the frequency tuning range can be increased by reducing the resonance frequency Ω_m and increasing the Q value and the power transmitted to the resonator.

Experiment. The radiation source in our experiments was a He–Ne laser of the LGN-207 type (λ = 0.63 μm). In comparison with the commercial device, our setup allowed the resonator frequency to be changed relative to the amplification spectrum, thus switching the source from double- to single-mode lasing. The interferometer scheme assumed a double-beam configuration (Fig. 1b) with a phase modulator in the signal arm.

The fiber optic phase modulator represented a ≅300-m-long single-mode optical fiber tightly coiled in seven layers (≅1000 turns) on a composite electromechanical resonator. The resonator comprised a pair of elastic cylindrical elements made of bronze, touching one another along the cylinder generatrix. The principal bending mode of the cylindrical elements (≅4.9 kHz) was excited with the aid of piezoceramic transducers. In an unloaded state (~10 turns), the modulator had $Q \sim 1000$. The piezoceramic transducers were driven by a unipolar ac voltage with an amplitude of about 150 V applied to the electrodes.

When the laser operated in a double-mode regime, the oscillogram contained symmetric spikes (Fig. 2) described by the second term in Eq. (2). The spikes correspond to an intermode beat frequency of $\Delta\nu$ = 650 MHz. The instantaneous frequency deviation produced by the phase modulator was calculated as

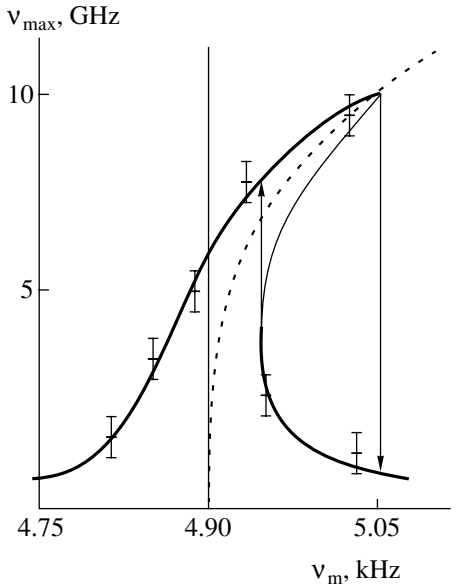

Fig. 3. The plot of instantaneous frequency deviation versus frequency of the applied voltage (U_m = 150 V).

described in [5]. Formula (4) yields 10 GHz, which corresponds to the total frequency tuning range of 20 GHz.

As demonstrated above, the frequency deviation in our system was determined by the interval of a linear relationship between the elastic strain amplitude and the external force magnitude. Calculation of the Ω_{max} value for a modulator with ρ = 8000 kg/m^3, $\sigma_{el} \cong$ 100 MPa, E = 120 GPa, λ = 0.63 μm, n = 1.45, and N = 1000 yields $\Omega_{max}/2\pi \cong 9.4$ GHz, in agreement with the experimental value.

If the oscillation amplitude increases so that $\sigma \geq \sigma_{el}$, the anharmonicity of the restoring force becomes an important factor leading to a nonlinear relationship between the resonance frequency and the external force amplitude. As a result, the resonance curve exhibits bending typical of the nonlinear oscillator. Figure 3 shows a resonance curve characteristic of the oscillations with a finite amplitude. The frequency detuning in our case was $\cong$150 Hz.

The transmitted power estimated by formula (11) for the instantaneous frequency deviation $\Delta\nu$ = 10 GHz amounts to $P \cong 12$ W. However, no heating of the resonator was observed in experiment. A thorough analysis of the energy losses showed that the resonator quality is mostly determined by a response to the acoustic emission from the oscillating system to the environment.

In our opinion, the use of a specially heat-treated beryllium bronze element will allow an instantaneous frequency deviation range up to 100 GHz (with a total frequency tuning range of 200 GHz) for a modulator coil containing 1000 turns. This is comparable to the frequency tuning range of a single-frequency dynamic semiconductor laser.

REFERENCES

1. P. Oberson, B. Huttner, and N. Gisin, Opt. Lett. **24**, 451 (1999).
2. H. Barfuss and E. Brinkmayer, J. Lightwave Technol. **7**, 3 (1989).
3. Miguel V. Andres, Meas. Sci. Technol. **3**, 217 (1992).
4. K. Tsuji, K. Shimizu, T. Horiguchi, and Y. Koyamada, IEEE Photonics Technol. Lett. **7**, 804 (1995).
5. V. T. Potapov, A. M. Mamedov, D. A. Sedykh, and S. V. Shatalin, Pis'ma Zh. Tekh. Fiz. **17** (16), 13 (1991) [Sov. Tech. Phys. Lett. **17**, 575 (1991)].
6. N. M. Belyaev, *Resistance of Materials* (Gostekhizdat, Moscow, 1962).
7. Zh. P. Pastukhova and A. G. Rakhshtadt, *Spring Alloys of Non-Ferrous Metals* (Metallurgiya, Moscow, 1983).

Translated by P. Pozdeev

Technical Physics Letters, Vol. 28, No. 4, 2002, pp. 340–342. Translated from Pis'ma v Zhurnal Tekhnicheskoĭ Fiziki, Vol. 28, No. 8, 2002, pp. 69–73.

Quantum Waveguides Laterally Coupled by a Periodic System of Small Windows: Bandgap Evaluation

O. P. Mel'nichuk and I. Yu. Popov

Institute of Fine Mechanics and Optics (Technical University), St. Petersburg, Russia

Received November 30, 2001

Abstract—The existence of a gap in the Laplace operator spectrum of two-dimensional quantum waveguides coupled by a periodic system of small windows is demonstrated by a variational method. © *2002 MAIK "Nauka/Interperiodica".*

Development of nanoelectronic technology has led to the need for studying quantum mesoscopic systems. An analysis of the ballistic transport of electrons in such quantum structures is based on studying the spectral properties of the Schrödinger operator. In the case under consideration, this operator reduces to the Laplace operator. Such systems were considered by many researchers [1–5].

We have studied a pair of two-dimensional (2D) waveguides coupled via a periodic system of small windows. Considering an analogous problem for a system with one window or with a finite number of such windows, Exner and Vugalter [4, 5] obtained variational estimates for an eigenvalue appearing due to the presence of coupling between the two channels. The corresponding asymptotics were found by one of the authors previously [6–8].

In the periodic case, the problem reduces to determining the band parameters. The corresponding solution must obey the Bloch condition: $\psi(x + L) = e^{i\theta l}\psi(x)$, where L is the period and θ is the quasi-momentum ($-\pi/L \le \theta \le \pi/L$). For an operator with a fixed quasi-momentum, this leads to the problem of finding the eigenvalues λ_{θ_a}. By varying the θ values within the above limits, we determine the band parameters. It is important to know whether a gap (forbidden band) is present between this band and the continuum of the Laplace operator for the waveguide without holes (the latter part of the spectrum is retained in the system with holes). Below we demonstrate that there exists a constant δ_a such that the inequality $\pi^2 d^{-2} - \lambda_{\theta_a} > \delta_a > 0$ is valid for all θ.

Consider two 2D waveguides with the same transverse size d, coupled via a periodic system of $2a$-wide windows arranged at a period of L. Let a trial function (on a single period $[-L/2, L/2]$) be represented in the form $\psi = F + G$,

$$F_{\left[-\frac{L}{2}, -a\right]}(x, y) = \alpha V(y)\{Ae^{k(x+a)} + Be^{-k(x-a)} + e^{k(x+a)}\},$$

$$F_{\left[a, \frac{L}{2}\right]}(x, y) = \alpha V(y)\{Ae^{k(x+a)} + Be^{-k(x-a)} + e^{-k(x-a)}\},$$

$$F_{[-a, a]}(x, y) = \alpha V(y)\{1 + Ae^{k(x+a)} + Be^{-k(x-a)}\},$$

$$G(x, y) = \sum_{-\infty}^{\infty} \eta\chi_{[Ln-a, Ln+a]} e^{inL\theta} \cos\left(\frac{\pi(x - nL)}{2a}\right) R(y),$$

where

$$A = \sum_{n=1}^{\infty} e^{-nL(k - i\theta)}, \quad B = \sum_{n=1}^{\infty} e^{-nL(k + i\theta)}, \quad A = \bar{B},$$

$$R(y) = \begin{cases} e^{-\frac{\pi y}{2a}}, & y \in \left[0, \frac{d}{2}\right], \\ 2\left(1 - \frac{y}{d}\right)e^{-\frac{\pi d}{4a}}, & y \in \left[\frac{d}{2}, d\right], \end{cases}$$

$$V(y) = \sqrt{\frac{2}{d}} \sin\left(\frac{\pi y}{d}\right),$$

and α, η and k are certain parameters which will be determined below.

Consider the form $M(\psi) = (H\psi, \psi) = \frac{\pi^2}{d^2}\|\psi\|^2$, where H is the Dirichlets Laplacian. Representing the operator

part as the sum $\|\psi_x\|^2 + \|\psi_y\|^2$, we obtain for the above trial function

$$M(\psi) = \|F_x\|^2 + \|G_x\|^2 + \|G_y\|^2 - \int_{-a}^{a} G(x,0)[\bar{F}_x(x,0) + F_x(x,0)] + \int_{-a}^{a} dx \int_0^d dy G_x[\bar{F}_x + F_x].$$

For sufficiently small a, the above quantities obey the following inequalities:

$$\|R\|^2 = \frac{a}{\pi} + \left(\frac{d}{6} - \frac{a}{\pi}\right)e^{-\pi d/2a} < \frac{a}{\pi}(1+\varepsilon),$$

$$\|R'\|^2 = \frac{\pi}{4a} + \left(\frac{2}{d} - \frac{\pi}{4a}\right)e^{-\pi d/2a} < \frac{\pi}{4a}$$

and, hence,

$$\|G_x\|^2 + \|G_y\|^2 = \eta^2\frac{\pi^2}{4a}\|R\|^2 + \eta^2 a\|R'\|^2 < \frac{\pi}{4}(2+\varepsilon)\eta^2.$$

Now let us estimate the integrals in the above expression for $M(\psi)$:

$$\int_{-a}^{a} G(x,0)[\bar{F}_x(x,0) + F_x(x,0)] = \alpha\eta\sqrt{\frac{2}{d}}\frac{8a}{d},$$

$$\int_{-a}^{a} dx \int_0^d dy G_x[\bar{F}_x + F_x] = -\alpha\eta\frac{4a\pi k^2(A+B)}{\pi^2 + 4a^2k^2}(e^{2ka}+1)\int_0^d RV dy,$$

$$\int_0^d RV dy = \frac{d}{\pi}\sqrt{\frac{2}{d}}\frac{4a^2}{d^2+4a^2} + \frac{2e^{-\frac{\pi d}{4a}}}{\pi}\sqrt{\frac{2}{d}}(1-ad) < \frac{d}{\pi}\sqrt{\frac{2}{d}}\frac{4a^2}{d^2+4a^2}(1+\varepsilon_1).$$

By minimizing all terms in $M(\psi)$ (except for $\|F_x\|^2$) with respect to η, we obtain

$$M(\psi) < \|F_x\|^2 - \alpha^2\frac{2^7a^2}{\pi d^3(2+\varepsilon)}(1-\varepsilon_2).$$

Now we can write expressions for the norms $\|F_x\|^2$ and $\|F\|^2$:

$$\|F_x\|^2_{[-a,a]} = \alpha^2 k(AB(e^{4ka}-1) - 2ake^{2ka}(A^2+B^2)),$$

$$\|F_x\|^2_{\left[a,\frac{L}{2}\right]} = \frac{\alpha^2 k}{2}((1+A+B)(1-e^{-k(L-2a)}) + 2ABe^{2ka} \times (\sinh kL - \sinh 2ka) - ke^{2ka}(L-2a)(A^2+B^2+A+B)),$$

$$\|F\|^2_{\left[a,\frac{L}{2}\right]} = \frac{\alpha^2}{2k}((1+A+B)(1-e^{-k(L-2a)}) + 2ABe^{2ka} \times (\sinh kL - \sinh 2ka) + ke^{2ka}(L-2a)(A^2+B^2+A+B)),$$

$$\|F\|^2_{[-a,a]} = \frac{\alpha^2}{k}(2ak + 2(A+B)(e^{2ka}-1) + AB(e^{4ka}-1) + 2ake^{2ka}(A^2+B^2)).$$

For sufficiently small k, $M(\psi) < 0$ and, hence, an estimate from above for the ratio $M(\psi)/\|\psi\|^2$ can be obtained by increasing the denominator and $\|F_x\|^2$:

$$\|\psi\|^2 \le 2\|F\|^2_{a<x<\frac{L}{2}} + 2\|F\|^2_{-a<x<a} + 2\|G\|^2_{-a<x<a} = 2\|F\|^2_{a<x<\frac{L}{2}} + 2\|F\|^2_{-a<x<a} + 2a\eta^2\|R\|^2.$$

Since the last term in this sum is on the order of a^5, we obtain

$$\|\psi\|^2 \le 2\left(\|F\|^2_{a<x<\frac{L}{2}} + \|F\|^2_{-a<x<a}\right)(1+\varepsilon_3).$$

The norm $\|F\|^2$ significantly depends on the AB, $A+B$, and A^2+B^2 values, which are different for various θ (at sufficiently small k). For $\theta = 0$, the AB, $A+B$, and $A_2 + B_2$ values are on the order of $1/k$, $1/k^2$, and $2/k^2$, respectively, while for $\theta \neq 0$, these values are limited. Evaluating the denominator and the norm $\|F_x\|^2$ from above (i.e., using ψ values corresponding to $\theta = 0$), we obtain

$$\|\psi\|^2 \le \frac{1}{k^2}\left(\frac{4}{L} + o(k^0)\right) \sim \frac{C_1}{k^2},$$

$$\|F_x\|^2 \le k^2\left(\frac{5}{6}L + o(k^0)\right) \sim k^2 C_2.$$

Thus, the required estimate from above is

$$\frac{M(\psi)}{\|\psi\|^2} \le \frac{1}{C_1}\left(k^4 C_2 - \frac{2^7a^2k^2}{\pi d^3(2+\varepsilon)}(1-\varepsilon_2)\right)(1+\varepsilon_3).$$

Minimized with respect to k, this expression even-

tually yields

$$\frac{M(\psi)}{\|\psi\|} \le -\frac{C_2}{C_1}\frac{2a^4(1-\varepsilon_2)^2}{\pi^2 d^6(2+\varepsilon)^2}(1+\varepsilon_3).$$

This estimate refers to the upper band edge, proves the existence of the gap, and provides for an estimate of the bandgap width:

$$\Delta \ge \frac{C_2}{C_1}\frac{2a^4(1-\varepsilon_2)^2}{\pi^2 d^6(2+\varepsilon)^2}(1+\varepsilon_3).$$

It should be emphasized that this is a rough estimate.

Acknowledgments. This study was supported by the Russian Foundation for Basic Research, project no. 01-01-00253.

REFERENCES

1. C. W. J. Beenakker and H. van Houten, Solid State Phys., Adv. Res. Appl. **44**, 1 (1991).
2. W. Bulla, F. Gesztesy, W. Renger, and B. Simon, Proc. Am. Math. Soc. **125**, 1487 (1997).
3. Y. Takagaki and K. Ploog, Phys. Rev. B **49** (3), 1782 (1994).
4. P. Exner and S. A. Vugalter, Ann. Inst. Henri Poincaré **65** (1), 109 (1996).
5. P. Exner and S. A. Vugalter, J. Phys. A **30**, 7863 (1997).
6. I. Yu. Popov, Pis'ma Zh. Tekh. Fiz. **23** (3), 57 (1999) [Tech. Phys. Lett. **25**, 106 (1999)].
7. I. Yu. Popov, Rep. Math. Phys. **43** (3), 427 (1999).
8. I. Yu. Popov, Appl. Math. Lett. **14**, 109 (2001).

Translated by P. Pozdeev

Technical Physics Letters, Vol. 28, No. 4, 2002, pp. 343–345. Translated from Pis'ma v Zhurnal Tekhnicheskoĭ Fiziki, Vol. 28, No. 8, 2002, pp. 74–78.

The Formation of Development Centers in Silver Bromide Based Composites under the Action of Electric Field and Temperature

L. V. Kolesnikov, Yu. S. Popov, A. I. Plotnikov, I. L. Kolesnikova, S. A. Sozinov, and L. A. Kozyak

Kemerovo State University, Kemerovo, Russia

e-mail: lvk@phys.kemsu.ru

Received December 10, 2001

Abstract—We have studied the formation of development centers in composites of the silver bromide–pyroelectric type under the action of electric field and temperature. It is demonstrated that an excitation (in the form of charge carriers or light quanta) can be transferred from some pyroelectric materials to silver bromide under thermal excitation conditions. The electric-field-induced formation of development centers in the composites is probably related to the surface reconstruction under the action of a polarizing electric field. © *2002 MAIK "Nauka/Interperiodica".*

The formation of development centers (silver clusters) on the surface of silver bromide (AgBr) microcrystals can be initiated by direct absorption of a light quantum, followed by the formation of an electron–hole pair (e^-, p^+) and a latent image (Ag_n) according to the scheme

$$AgBr + h\nu \longleftrightarrow e^- + p^+,$$

$$e^- + Ag_i^+ \longrightarrow Ag^0 + e^- \longrightarrow Ag^- + Ag^+$$

$$\longrightarrow Ag_2^+ + \ldots \longrightarrow Ag_n^+,$$

where Ag_i^+ is an interstitial silver ion, $h\nu$ is the light quantum, and e^- and p^+ are the electron and hole in AgBr microcrystals.

Alternatively, the development centers can appear as a result of the transfer of a light quantum, electron, or hole via contact with some other material excited under the action of an electric field or temperature. In order to check for this possibility, we have studied a system comprising AgBr–pyroelectric composites dispersed in gelatin.

The composites were prepared using homogeneous AgBr microcrystals possessing a (111) octahedral habit. In the first step, the AgBr grains with an average size of ~1 μm were obtained by a double-jet crystallization technique [1] in a gelatin matrix. Then a microcrystalline pyroelectric was introduced into the reactor in the form of a micron-sized powder or a solution of certain concentration (provided that the pyroelectric compound possessed sufficiently high solubility). Finally, the resulting emulsions were applied onto a substrate and dried.

The microcrystalline pyroelectrics were selected for the known dependence of the spontaneous polarization on the temperature and applied electric field strength. The pyroelectrics (as well as ferroelectrics) exhibit the phenomenon of spontaneous emission induced by temperature variations, which is related to a change in the surface charge state in the course of the pyroeffect development. The conditions and laws of the spontaneous emission activity of pyroelectrics were extensively studied in the past two decades (for the most exhaustive review, see [2]).

We have studied the spontaneous emission activity of selected pyroelectrics by measuring the spectra of thermoinduced photon and electron emission. Figure 1 shows the spectra obtained for a LiB_4O_7 single crystal.

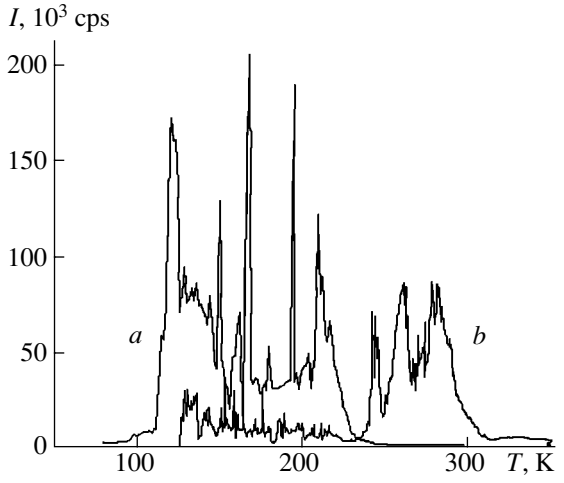

Fig. 1. The spectra of temperature induced (*a*) photon and (*b*) electron emission from a LiB_4O_7 single crystal.

1063-7850/02/2804-0343$22.00 © 2002 MAIK "Nauka/Interperiodica"

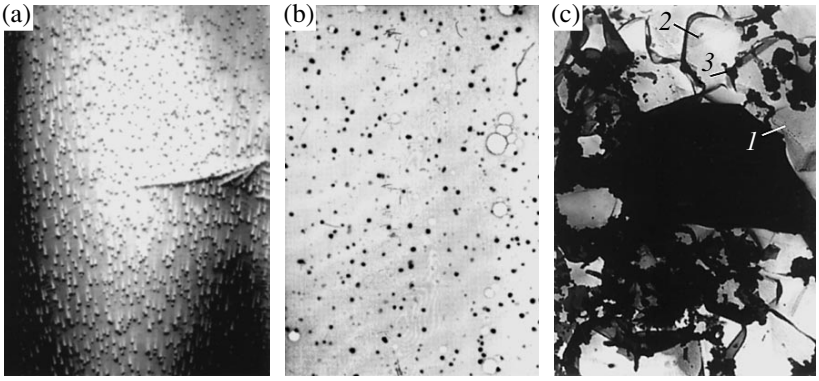

Fig. 2. Photographs illustrating the effect of (a) electric field and (b) temperature on the formation of a development center in AgBr–pyroelectric composites; (c) micrograph of an AgBr–pyroelectric composite showing (*1*) pyroelectric grains, (*2*) AgBr(111) grains, and (*3*) silver clusters.

Polycrystalline samples of pyroelectrics (with an average size of ~1 μm) also exhibit spontaneous emission activity, but the intensity of the process is somewhat lower as compared to that in single crystals.

The redistribution of charge carriers in composites of the type studied can be driven by the difference in the Fermi energy of the contacting materials and in the temperature dependence of this parameter. Information on the Fermi energy relations between some pyroelectric and AgBr microcrystals was obtained by the Kelvin method. Application of this technique to the system under consideration has certain features related to a high concentration of the Frenkel defects in silver halide crystals and to a high polarizability of pyroelectrics. The samples were polarized when the voltage applied to a vibrating electrode differed from the compensating voltage, which was taken into account in determining the contact potential difference (CPD). The potential at the sample–substrate contact was determined by solving a system of equations describing the thermodynamic equilibrium of particles capable of crossing the interface and the electroneutrality in the sample volume. In this way, we obtained equations relating the CPD value to the Fermi energy and the thermodynamic characteristics of the samples studied. Since the CPD values (see table) of *L*-arginine, $LiIO_3$, and KH_2PO_4 are close to the value for AgBr(111), the systems employing these components will exhibit no dark translation of charge carriers through the interface with AgBr. As for LiB_4O_7, we may expect that a dark transport of electrons through the contact into AgBr will take place with the formation of a latent image.

Figures 2a and 2b show the photographs of developed emulsion layers based on the AgBr–pyroelectric composites studied. These images confirm the formation of development centers in mc-AgBr both after exposure of the emulsion to an electric field and after cooling to liquid nitrogen temperature. For comparison, we have also studied "pure" AgBr emulsions.

All samples were examined under an electron microscope in order to determine the dimensions of microcrystals, their distribution, and the features of silver cluster formation on the surface of AgBr grains in the presence of pyroelectric microcrystals. For this purpose, AgBr grains were isolated from the gelatin matrix, mixed with powdered pyroelectric, and subjected to thermal cycling. Then, the sample was developed in a standard 2% developing solution.

In order to reveal the silver clusters, the results were compared to those obtained for a control sample not

CPD values for emulsions with pyroelectrics and AgBr(111) measured immediately upon application, after dehydration (water removal from the surface by heating to 370 K), and after storage for 3 days

	CPD, mV						
sample	initial	upon dehydration			after 3-day storage		
[temperature, K]	300	300	370	300	300	360	300
L-arginine	61	60	55	51	55	58	60
$LiIO_3$	75	51	43	46	48	59	69
KH_2PO_4	24	38	48	45	49	55	66
LiB_4O_7	106	93	98	111	97	106	104
AgBr(111)	58	53	49	51	51	61	65

subject to thermal cycling and developed under identical conditions. Figure 2c shows a micrograph of the AgBr(111) grains with pyroelectric particles. In all the samples after development, the surface of AgBr grains contained silver particles. The formation of these development centers can be explained by the redistribution of charge carriers (electrons and holes) in the contact system and by the particular preparation conditions. The features of silver evolution on the surface of AgBr microcrystals in immediate contact with the pyroelectric were studied by methods of the electron diffraction analysis.

Thus, we have obtained for the first time data showing that information can be recorded in AgBr–pyroelectric composites in the dark due to the spontaneous pyroelectric activity phenomenon. The formation of development centers (silver clusters) in the AgBr–pyroelectric composites exposed to an electric field is a new effect that cannot be explained by the emission of light quanta or charge carriers from pyroelectric grains. A possible reason for the silver cluster formation on AgBr microcrystals under these conditions can be the AgBr surface modification related to displacement of the ion equilibrium in the contact region as a result of polarization of the pyroelectric. A similar effect was observed in AgBr(111) microcrystals upon changing the ion equilibrium in the AgBr(111)–gelatin system [1], where the resulting sensitivity was comparable with that induced by sulfur-containing additives.

Acknowledgments. The authors are grateful to Prof. L.I. Isaenko for kindly providing the samples of pyroelectrics.

This study was supported by the Russian Foundation for Basic Research, project nos. 00-03-32538, 01-03-06077, and 01-03-06078.

REFERENCES

1. I. L. Kolesnikova, S. A. Sozinov, E. V. Shaposhnikova, *et al.*, Zh. Nauchn. Prikl. Fotogr. **45** (3), 17 (2000).
2. G. Rosenmann and D. Shur, J. Appl. Phys. **88** (11), 6109 (2000).

Translated by P. Pozdeev

Technical Physics Letters, Vol. 28, No. 4, 2002, pp. 346–348. Translated from Pis'ma v Zhurnal Tekhnicheskoĭ Fiziki, Vol. 28, No. 8, 2002, pp. 79–84.

Dissipation of the Fluctuational Electromagnetic Field Energy, Tangential Force, and Heating Rate of a Neutral Particle Moving near a Flat Surface

G. V. Dedkov and A. A. Kyasov

Kabardino-Balkarian State University, Nal'chik, Kabardino-Balkaria, Russia

Received November 19, 2001

Abstract—A relationship between the dissipation of the fluctuational electromagnetic field energy, tangential (decelerating) force, and heating rate of a neutral particle moving parallel to a plane polarizable surface is considered for the first time in a nonrelativistic approximation. The formulas obtained take into account dielectric properties of the particle and surface. *© 2002 MAIK "Nauka/Interperiodica".*

The process of a fluctuation-dissipative interaction between moving neutral particles (atoms, clusters, and nanoparticles) and a solid surface is still incompletely clear despite considerable effort of several groups of researchers [1–14]. In recent papers [10], we have developed a nonrelativistic theory of the corresponding conservative and dissipative forces. In particular, the tangential force acting upon a moving particle was determined as the integral of dissipative energy losses of the fluctuational electromagnetic field, which was taken over the particle volume and divided by the particle velocity. An analogous approach was used in [5, 12], where the power of the dissipative tangential force was determined as the rate of heating (cooling) of the contacting bodies. Alternatively [11, 13], the local surface heating under the action of a probing electron beam in a scanning electron microscope was determined as the work performed by the fluctuational electromagnetic field upon electrons of the beam. However, a more detailed analysis shows that, although the dissipative forces between bodies performing relative (contactless) motion and the heat exchange are basically related, the relation between these factors is by no means simple. However, no clear definition of these values within the framework of the problem of sliding friction has been given so far, which is a source of numerous discrepancies [1–3, 5, 7–13].

The purpose of this study was to establish general (nonrelativistic) relationships between the work of a fluctuational electromagnetic field, the rate of heating of a moving particle, and the tangential force acting upon the particle, and to calculate these quantities using a general computation method [10].

Consider a neutral particle moving in vacuum along the x axis with the velocity V at a distance of z_0 from the flat boundary of a semi-infinite medium with the dielectric permittivity $\varepsilon(\omega)$ (it is assumed that z_0 is much greater than the atomic size). Following [10], the vector of polarization induced by the particle in the medium is

$$\mathbf{P}(\mathbf{r}, t) = \delta(x - Vt)\delta(y)\delta(z - z_0)\mathbf{d}(t), \qquad (1)$$

where $\mathbf{d}(t)$ is the fluctuating dipole moment of the particle. By definition, the electric current density related to the polarization $\mathbf{P}(\mathbf{r}, t)$ is $\mathbf{j} = \partial\mathbf{P}(\mathbf{r}, t)/\partial t$. In the absence of radiation, the law of energy conservation in the particle–surface system yields

$$-\frac{dW}{dt} = \int \langle \mathbf{jE} \rangle d^3\mathbf{r}. \qquad (2)$$

Here, the left-hand part represents the rate of energy losses of the fluctuational electromagnetic field and the right-hand part is the averaged work performed (per unit time) by the field $\mathbf{E}$ upon the moving particle; the angle brackets denote full quantum-statistical averaging. Using relations (1) and (2), we obtain

$$\int \langle \mathbf{jE} \rangle d^3\mathbf{r} = V\left\langle \frac{\partial}{\partial x}(\mathbf{dE}) \right\rangle + \langle \mathbf{dE} \rangle. \qquad (3)$$

It should be emphasized that the first step in calculating (3) consists in taking the derivative $\partial/\partial x$, after which the Cartesian coordinates of the particle $\mathbf{r} = (Vt, 0, z_0)$ at the time instant t are substituted. Accomplishing some transformations with the first term in the right-hand part of (3) and taking into account that curl$\mathbf{E} = 0$ in the nonrelativistic case under consideration, we obtain

$$\frac{1}{V}\int \langle \mathbf{jE} \rangle d^3\mathbf{r} \equiv \langle (\mathbf{d}\nabla)E_x \rangle + \frac{1}{V}\langle \mathbf{dE} \rangle. \qquad (4)$$

The first term in this identity describes the tangential component of the "dipole" force acting upon the particle, while the second term reflects heating of the particle; the dissipation integral in the left-hand part of (4) is taken over the particle volume. For a neutral atom (considered as a system of bound charges), the rate of heating can be interpreted in terms of the Lamb shift of

levels under the action of the fluctuational electromagnetic field. According to Eq. (4), equality of the tangential force power and the fluctuational field energy dissipation rate is strictly obeyed only for a particle possessing a constant dipole moment. Unfortunately, insufficient attention has been paid to this circumstance so far [5, 10–13].

The tangential dipole force acting upon the particle will be calculated by the previously developed method [10]. The only difference is that we proceed from an expression for the dipole force as a sum of two terms describing interaction between spontaneous and induced components of the dipole moment and the electric field of the particle and the surface:

$$F_x = \langle (\mathbf{d}\nabla)E_x \rangle = \langle (\mathbf{d}^{sp}\nabla)E_x^{in} \rangle + \langle (\mathbf{d}^{in}\nabla)E_x^{sp} \rangle. \quad (5)$$

In the local approximation, the final formula for the dielectric response of the surface in the general case of unequal temperatures of the particle (T_1) and the surface (T_2) is as follows:

$$F_x = \langle (\mathbf{d}\nabla)E_x \rangle = -\frac{2\hbar}{\pi^2}\int\int\int d\omega dk_x dk_y k_x k \exp(-2kz_0)$$
$$\times \left\{ \coth\left(\frac{\omega\hbar}{2k_B T_1}\right)\alpha''(\omega)[\Delta''(\omega + k_x V) - \Delta''(\omega - k_x V)] \right. \quad (6)$$
$$\left. + \coth\left(\frac{\omega\hbar}{2k_B T_2}\right)\Delta''(\omega)[\alpha''(\omega + k_x V) - \alpha''(\omega - k_x V)] \right\}.$$

Here, $k = \sqrt{k_x^2 + k_y^2}$, $\Delta(\omega) = \dfrac{\varepsilon(\omega) - 1}{\varepsilon(\omega) + 1}$, $\alpha(\omega)$ is the particle polarizability (the double prime denotes imaginary components of the corresponding functions); the integration is performed over positive frequencies and wave vector projections. For $T_1 = T_2 = T$ and the linear approximation with respect to velocity, Eq. (6) reduces to

$$F_x = \langle (\mathbf{d}\nabla)E_x \rangle$$
$$= \frac{3\hbar V}{4\pi z_0^5}\int_0^\infty d\omega \alpha''(\omega)\Delta''(\omega)\frac{d}{d\omega}\coth\left(\frac{\omega\hbar}{2k_B T}\right). \quad (7)$$

This expression coincides with the formula derived in [8, 14] upon substituting $\coth(x/2)$ for $[\exp(x) - 1]^{-1}$. However, in our opinion, the methods employed in [8, 14] for deriving formula (7) are insufficiently correct. Indeed, the procedure used in [8] was based on the nonstationary perturbation theory, whereby the matrix element of the perturbation Hamiltonian ($\hat{V} = -\hat{\mathbf{d}}\hat{\mathbf{E}}$) was replaced (without clear physical justification) by a matrix element of the dipole force operator ($(\hat{\mathbf{d}}\nabla)\hat{E}_x$). Persson [14] (see also [3]) derived formula (7) using the Kubo formula for a friction coefficient tensor

$$\eta_{ij} = (k_B T)^{-1}\mathrm{Re}\int_0^\infty dt \langle \hat{\mathbf{F}}_i(t)\hat{\mathbf{F}}_j(0) \rangle, \quad (8)$$

where $\hat{\mathbf{F}}_i = (\hat{\mathbf{d}}\nabla)\hat{E}_i)$ is the random force operator. The correlator in the integral was separated as follows (see also [3, 8]):

$$\langle d_k(t)\nabla_k E_i(\mathbf{r}_0, t) d_l(0)\nabla_l E_j(\mathbf{r}_0, 0) \rangle$$
$$\approx \langle d_k(t)d_l(0) \rangle \langle \nabla_k E_i(\mathbf{r}_0, t)\nabla_l E_j(\mathbf{r}_0, 0) \rangle. \quad (9)$$

As can be readily seen, the approximation employed in (9) fully ignores the correlation between the fluctuating dipole moment of the particle and the electric field of the surface. However, this very factor accounts for the conservative van der Waals interaction between the particle and the surface ($U = -1/2\langle \mathbf{dE} \rangle \neq 0$!). Thus, the above considerations offer essentially the first consistent (free of additional limitations) derivation of formula (7), while expression (6) is the most general nonrelativistic formula for the tangential force between the particle and the surface with arbitrary temperatures.

The second term in (5) is calculated by analogy with the first term, and the final formula is

$$\langle \dot{\mathbf{d}}\mathbf{E} \rangle = \langle \dot{\mathbf{d}}^{sp}\mathbf{E}^{in} \rangle + \langle \dot{\mathbf{d}}^{in}\mathbf{E}^{sp} \rangle$$
$$= -\frac{2\hbar}{\pi^2}\int\int\int d\omega dk_x dk_y k \exp(-2kz_0)$$
$$\times \left\{ \coth\left(\frac{\omega\hbar}{2k_B T_1}\right)\alpha''(\omega)[\omega\Delta''(\omega + k_x V) \right. \quad (10)$$
$$+ \omega\Delta''(\omega - k_x V)] - \coth\left(\frac{\omega\hbar}{2k_B T_2}\right)\Delta''(\omega)$$
$$\left. \times [(\omega + k_x V)\alpha''(\omega + k_x V) + (\omega - k_x V)\alpha''(\omega - k_x V)] \right\}.$$

As can be readily shown, Eqs. (6), (7), and (10) yield a zero result at $T_1 = T_2 = 0$ in the linear approximation with respect to velocity. In [3, 6], the friction coefficient in this case was determined using the perturbation theory of a higher order, which led to a relationship of the type $\eta \sim z_0^{-10}$. In our opinion, this situation requires a more detailed analysis of the tangential forces with an allowance for the fluctuating multipoles of higher orders (not taken into account in [3, 6]), which are expected to obey the relationship $\eta \sim z_0^{-n}$ with $n < 10$. On the other hand, we have to take into account effects of the spatial dispersion and the surface structure, which lead to a tensor character of the dielectric function. It was recently demonstrated [15] that an allow-

ance for the spatial dispersion reduces to formally substituting $\Delta(\omega, \mathbf{k})$ for the local function $\Delta(\omega)$.

For $V = 0$, Eq. (10) describes the rate of heat exchange $\dot{Q}$ between the particle and the surface (the case of $\dot{Q} < 0$ corresponds to cooling of the particle and the heat transfer to the surface). For a material with high conductivities (σ_1 and σ_2) under the conditions $k_B T/\hbar \ll 2\pi \max(\sigma_1, \sigma_2)$ and a spherical particle of radius R, Eq. (10) yields

$$\dot{Q} = -\frac{\pi}{80}\frac{k_B^4}{\hbar^3}\frac{R^3}{z_0^3}\frac{(T_1^4 - T_2^4)}{\sigma_1\sigma_2}. \quad (11)$$

This formula agrees with the results obtained in [11, 13] to within a factor on the order of unity.

REFERENCES

1. E. V. Teodorovich, Proc. R. Soc. London, Ser. A **362**, 71 (1978).
2. J. Mahanty, J. Phys. B **13**, 4391 (1980).
3. W. L. Schaich and J. Harris, J. Phys. F **11**, 65 (1981).
4. J. A. Annett and P. M. Echenique, Phys. Rev. B **34**, 6853 (1986); **36**, 8986 (1987).
5. V. G. Polevoĭ, Zh. Éksp. Teor. Fiz. **98** (6), 1990 (1990) [Sov. Phys. JETP **71**, 1119 (1990)].
6. B. N. J. Persson and A. I. Volokitin, J. Chem. Phys. **103**, 8679 (1995).
7. J. B. Pendry, J. Phys.: Condens. Matter **9**, 10301 (1997).
8. M. S. Tomassone and A. Widom, Phys. Rev. B **56**, 4938 (1997).
9. A. I. Volokitin and B. N. J. Persson, Phys. Low-Dimens. Struct. **7** (8), 1 (1998); J. Phys.: Condens. Matter **11**, 34 (1999).
10. G. V. Dedkov and A. A. Kyasov, Phys. Lett. A **259**, 38 (1999); Pis'ma Zh. Tekh. Fiz. **25** (12), 11 (1999) [Tech. Phys. Lett. **25**, 466 (1999)]; Surf. Sci. **463** (1), 11 (2000); Fiz. Tverd. Tela (St. Petersburg) **43** (1), 169 (2001) [Phys. Solid State **43**, 176 (2001)].
11. J. B. Pendry, J. Phys.: Condens. Matter **11** (35), 6621 (1999).
12. I. Dorofeyev, H. Fuchs, G. Wenning, and B. Gotsmann, Phys. Rev. B **64**, 35403 (2001).
13. A. I. Volokitin and B. N. J. Persson, Phys. Rev. B **63**, 205404 (2001); J. Phys.: Condens. Matter **13** (5), 859 (2001).
14. B. N. J. Persson, private communication (2000).
15. G. V. Dedkov and A. A. Kyasov, Pis'ma Zh. Tekh. Fiz. **27** (8), 68 (2001) [Tech. Phys. Lett. **27**, 338 (2001)].

Translated by P. Pozdeev

Technical Physics Letters, Vol. 28, No. 4, 2002, pp. 349–350. Translated from Pis'ma v Zhurnal Tekhnicheskoĭ Fiziki, Vol. 28, No. 8, 2002, pp. 85–88.

Determining Charged Particle Energy Losses with the Aid of Transmutation Isotopes

V. A. Didik, R. Sh. Malkovich, E. A. Skoryatina, and V. V. Kozlovskiĭ

Ioffe Physicotechnical Institute, Russian Academy of Sciences, St. Petersburg, 194021 Russia

St. Petersburg State Technical University, St. Petersburg, Russia

Received December 20, 2001

Abstract—A new method is proposed for determining the energy losses of charged particles in solids, which is based on the comparison of profiles of the transmutation isotopes measured in the samples irradiated by particles of various energies. © *2002 MAIK "Nauka/Interperiodica".*

Methods traditionally used for determining the energy losses of charged particles are based on various schemes of particle energy measurement employing scintillators [1], electrostatic energy analyzers [2], mass analyzers [3], semiconductor detectors [4], calorimeters [5], etc. We suggest determining the energy losses using the phenomenon of transmutation isotope formation as a result of the nuclear reactions between charged particles and matrix nuclei. To our knowledge, this method has never been used before.

The proposed technique is based on an analysis of the depth–concentration profiles of transmutation isotopes formed in a solid irradiated by charged particles [6]. According to this, identical samples of the same material are irradiated by particles of various fixed energies (under otherwise equal conditions). The irradiation induces nuclear transformation (transmutation) reactions resulting in the formation of radioactive isotopes. The profiles of a given transmutation isotope are obtained by removing thin material layers from the samples and measuring the isotope activity in the removed substance (Fig. 1a). The next stage consists in comparing the profiles obtained at various irradiation energies (Fig. 1b). For this purpose, a profile measured at a lower energy E_1 is superimposed onto one measured at a higher energy E_2 and the coordinate difference corresponding to the E_1 value is determined on the abscissa axis. Repeating this procedure for the profiles measured at various energies, we obtain the $E(x)$ curve describing the particle energy variation in depth of the sample.

Using the method outlined above, we determined the energy losses of protons in copper. The samples were irradiated on an MGTs-20 cyclotron at a proton energy of 8, 10, 12.5, 15.25, and 18 MeV. The particle flux density was 1.2×10^{12} cm^{-2} s^{-1} and the irradiation time was 1 h. We then measured the γ-activity of ^{65}Zn transmutation isotopes formed via the reaction ^{65}Cu(p, n)^{65}Zn [7]. The activity was determined using a calibrated gamma-spectrometer with a Ge(Li) detector. In addition to bulk copper, we have also studied samples obtained by stacking 10-μm-thick foil sheets. As

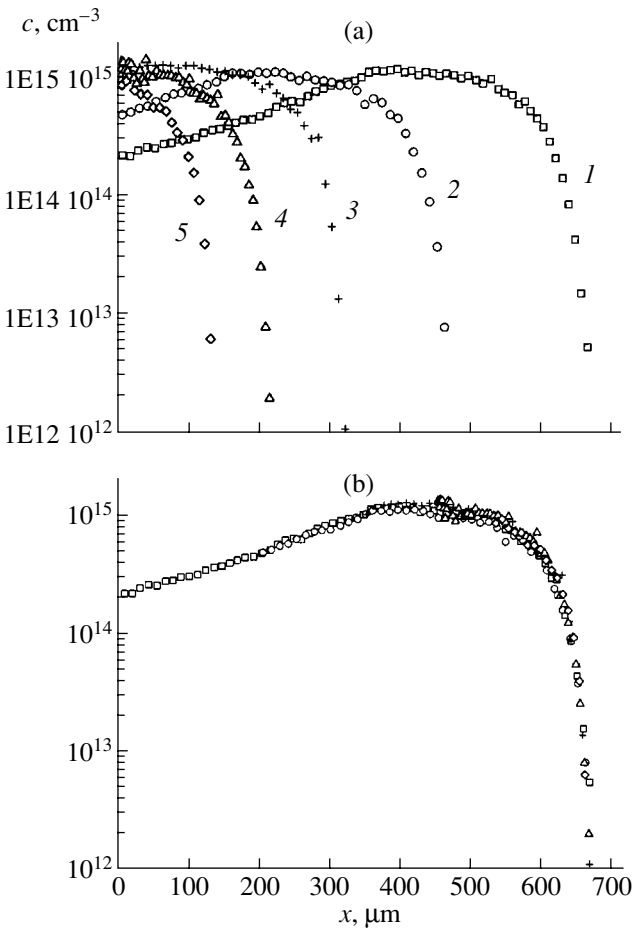

Fig. 1. Depth–concentration profiles of the ^{65}Zn transmutation isotope in copper (a) measured for various irradiating proton energies E = 18 (*1*), (*2*) 15.25, (*3*) 12.5, (*4*) 10, and 8 MeV (*5*) and (b) compared as described in the text. The isotope concentration c corresponds to the moment of termination of the irradiation process.

1063-7850/02/2804-0349$22.00 © 2002 MAIK "Nauka/Interperiodica"

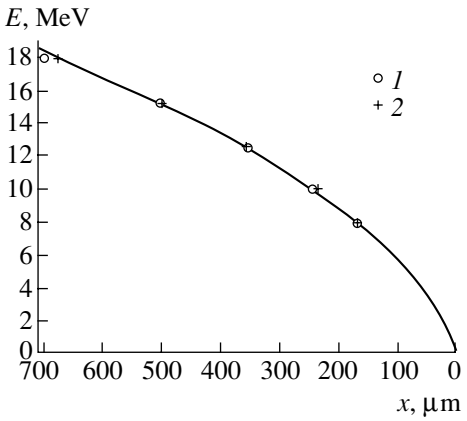

Fig. 2. The $E(x)$ plots for protons in copper, constructed using the proposed method in the (*1*) differential and (*2*) integral variant. The solid curve is plotted by the published data [8].

can be seen from Fig. 2, the results of our experiments agree satisfactorily with the published data [8].

The energy losses of charged particles were also determined using the proposed method in an integral variant. According to this, the integral γ-activity Q_1 of a given transmutation isotope is measured in the whole sample irradiated at a fixed energy E_1. Then, layers are removed from an identical sample irradiated at a higher energy E_2, unless the γ-activity of this sample becomes equal to Q_1. The total thickness of removed layers corresponds to the depth at which the initial particle energy (E_2) decreases to the E_1 value. The results obtained in this way also satisfactorily agree with the published data (Fig. 2).

REFERENCES

1. G. W. Gobeli, Phys. Rev. **103** (2), 275 (1956).
2. Yu. V. Gott and V. G. Tel'kovskiĭ, Fiz. Tverd. Tela (Leningrad) **9** (8), 2221 (1967) [Sov. Phys. Solid State **9,** 1741 (1967)].
3. E. M. Zarutskiĭ, Fiz. Tverd. Tela (Leningrad) **9** (5), 1501 (1967) [Sov. Phys. Solid State **9**, 1172 (1967)].
4. J. S.-Y. Feng, W. K. Chu, and M. A. Nicolet, Phys. Rev. B **10** (9), 3781 (1974).
5. H. H. Andersen, C. C. Hanke, H. Sorensen, and P. Vajda, Phys. Rev. **153** (2), 338 (1967).
6. V. A. Didik, R. Sh. Malkovich, E. A. Skoryatina, and V. V. Kozlovski, Nucl. Instrum. Methods Phys. Res. B **160**, 387 (2000).
7. C. Maples, G. Goth, and J. Cerny, Nucl. Data, Sect. A **2**, 429 (1967).
8. O. F. Nemets and Yu. V. Gofman, *Handbook of Nuclear Physics* (Kiev, 1975), p. 109.

Translated by P. Pozdeev

Technical Physics Letters, Vol. 28, No. 4, 2002, pp. 351–353. Translated from Pis'ma v Zhurnal Tekhnicheskoĭ Fiziki, Vol. 28, No. 8, 2002, pp. 89–94.

Effect of Centrifugation on the Crystal Structure of Barium Nitrate

V. A. Trounov, E. A. Tserkovnaya, V. N. Gurin, M. M. Korsukova, L. I. Derkachenko, and S. P. Nikanorov

Ioffe Physico-Technical Institute, Russian Academy of Sciences, St. Petersburg, 194021 Russia
e-mail: Maria.Korsukova@pop.ioffe.rssi.ru

Received December 13, 2001

Abstract—The structure of barium nitrate crystals grown from supersaturated aqueous solutions under normal conditions and during centrifugation at $11.8 \times 10^3 g$ is studied for the first time by a high-precision powder neutron diffraction method. It is established for the first time that centrifuging leads to displacement of the nitrate oxygen atoms in the *xy* plane (resulting in rotation of the NO_3 trigonal prism about the third-order axis) and to variation of the bond lengths and angles in the coordination polyhedron of Ba atoms. The latter changes result in the appearance of a torsional mode in the phonon spectrum of barium nitrate and in increasing stiffness of the crystal lattice, as evidenced by a significant increase in microhardness of the samples grown in the centrifuge. © *2002 MAIK "Nauka/Interperiodica".*

In previous investigations, we observed for the first time a significant change in stoichiometry, lattice period, and properties of a series of ionic crystals (including barium nitrate) grown from supersaturated aqueous solutions in a centrifuge accelerated to (1.3–11.8) $\times 10^3 g$ [1–3]. Below we report on the first comparative study of the structures of $Ba(NO_3)_2$ crystals grown under normal gravity conditions ($1g$) [3] and in a centrifuge ($11.8 \times 10^3 g$). The samples were characterized by the method of high-resolution powder neutron diffraction (PND).

The PND measurements were performed at room temperature in a time-of-flight Fourier diffractometer SPHYNX [4]. The crystals of barium nitrate were crushed and triturated in an agate mortar, after which the powdered samples (2.5 cm^3) were charged into cylindrical containers made of a titanium–zirconium alloy. The neutron diffraction patterns were obtained by data acquisition for 12 h and processed on a computer using the MRIA program package [5]. The amplitudes of elastic coherent neutron scattering from Ba, N, and O nuclei were taken from [6]. The experimental data were corrected for the absorption [7] and primary extinction [8]. The structures of both samples were refined in a $Pa\bar{3}$ space group (No. 205), with Ba, N, and O atoms in positions 4(a), 8(c), and 24(d), respectively [9].

Figure 1 shows the experimental neutron diffractograms. An analysis of these patterns reveals significant redistribution of the intensity of some peaks in the PND spectrum of the sample grown in the centrifuge in comparison with the spectrum of the sample grown under normal conditions ($1g$). Table 1 presents refined atomic

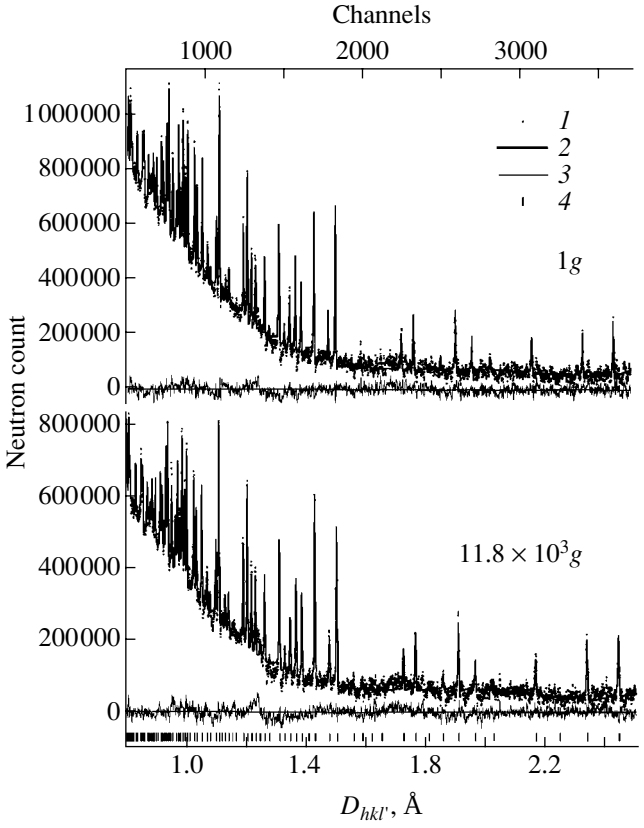

Fig. 1. Neutron diffractograms (neutron count versus interplanar spacing $D_{hkl'}$) of powdered $Ba(NO_3)_2$ crystals grown under normal conditions ($1g$) and in a centrifuge ($11.8 \times 10^3 g$): (*1*) experimental points; (*2*) theoretical model spectrum; (*3*) difference between experimental and theoretical spectra; (*4*) allowed reflections in the space group $Pa\bar{3}$ (No. 205).

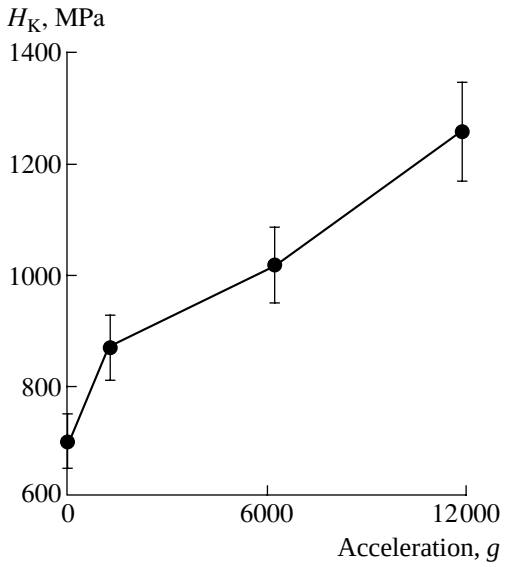

Fig. 2. The plot of microhardness H_K versus acceleration for $Ba(NO_3)_2$ crystals grown in a centrifuge (indentor load, P = 19.62 mN).

parameters; Table 2 summarizes data on the interatomic distances and bond angles in the structures of both samples (calculated using the program [10]).

According to the data in Table 1, the crystals grown in the centrifuge exhibit an 0.007 Å (10σ) increase in the lattice period as compared to that of the sample crystallized under normal conditions. While no changes are observed in the position of nitrogen atoms, the *x* and *y* parameters of oxygen atoms (indicated by bold) show a statistically significant variation by 6σ and 5σ, respectively. Since the *z* value remains virtually unchanged, we may conclude that oxygen atoms exhibit a static displacement in the *xy* plane; that is, the NO_3 groups are rotated about the $\bar{3}$ axis.

The data in Table 2 show that the nitrate group exhibits no structural changes as a result of centrifugation. However, significant modifications take place in the atomic environment of barium. In particular, Ba–O–N angles change by ≈1° (30σ). Interatomic distances in the coordination polyhedron of Ba are also significantly varied: the "short" Ba–O bond lengths decrease by 0.016 Å (7.5σ), while the "long" Ba–O distances increase by 0.021 Å (9σ); the O–O distance also grows by 0.021 Å (6σ), this leading to a still greater distortion of the cuboctahedron of oxygen atoms [9] under the action of centrifuging.

Thus, the experimental data are indicative of the possible appearance of a stiff torsional mode in the phonon spectrum and of the hardening of $Ba(NO_3)_2$ crystals grown in the centrifuge. This conclusion is confirmed by the results of microhardness measurements performed by a standard technique (a PMT-3 device with a Knoop pyramid indentor) on the barium nitrate crystals grown under normal conditions and under centrifugation with various accelerations [3]. The results of these measurements are presented in Fig. 2. As can be seen, the microhardness exhibits a significant growth with increasing acceleration, reaching a maximum level for the sample showing the most significant changes in the crystal structure.

Table 1. The results of crystal structure refinement for the $Ba(NO_3)_2$ crystals grown under normal conditions (1*g*) and in a centrifuge ($11.8 \times 10^3 g$) (figures in parentheses indicate standard deviations σ; bold figures indicate values differing by more than 5σ)

Parameters	1*g*	$11.8 \times 10^3 g$
Lattice period *a*, Å	**8.11021(7)**	**8.11698(7)**
Atomic positions (*x*/*a*, *y*/*b*, *z*/*c*):		
Ba: $x = y = z$	0	0
N: $x = y = z$	0.3519(2)	0.3520(2)
O: *x*	**0.2856(3)**	**0.2838(3)**
y	**0.2888(3)**	**0.2903(3)**
z	0.4776(3)	0.4772(3)
Profile fitting quality factor $R_w(F^2)$, %	6.59	7.46

Table 2. Interatomic distances and bond angles in the structure of barium nitrate crystals grown under normal conditions (1*g*) and in a centrifuge ($11.8 \times 10^3 g$) (figures in parentheses indicate standard deviations σ; bold figures indicate values differing by more than 5σ)

Interatomic distances, Å	1*g*	$11.8 \times 10^3 g$
Nitrate group: N–O	1.2611(29)	1.2610(29)
O–O	2.1840(34)	2.1837(34)
Short N–N distances	4.1608(23)	4.1615(23)
	4.3790(23)	4.3833(23)
Interatomic distances in Ba coordination polyhedron: Ba–O	**2.8865(24)**	**3.8702(24)**
Ba–O	**2.9928(24)**	**2.9439(24)**
O–O	**3.0264(34)**	**3.0471(34)**
Bond angles, deg		
Nitrate group: O–N–O	119.98(6)	119.97(6)
O–O–O	60.00(2)	60.00(2)
Ba–O–N	**96.99(3)**	**96.13(3)**
Ba–O–N	**98.76(3)**	**99.72(3)**
Ba–O–Ba	161.63(7)	161.64(7)

Acknowledgments. The authors are grateful to A.L. Malyshev for his help in conducting the neutron diffraction measurements.

This study was supported by the Russian Foundation for Basic Research, project no. 01-03-32822.

REFERENCES

1. V. N. Gurin, S. P. Nikanorov, M. Korsukova, *et al.*, Fiz. Tverd. Tela (St. Petersburg) **39** (10), 1792 (1997) [Phys. Solid State **39**, 1599 (1997)].
2. V. N. Gurin, S. P. Nikanorov, A. P. Nechitailov, *et al.*, in *Processing by Centrifugation*, Ed. by L. L. Regel and W. R. Wilcox (Kluwer, New York, 2001), p. 77.
3. V. N. Gurin, S. P. Nikanorov, A. P. Nechitailov, *et al.*, Fiz. Tverd. Tela (St. Petersburg) **43** (7), 1196 (2001) [Phys. Solid State **43**, 1241 (2001)].
4. V. A. Trunov, V. A. Kudryashev, A. P. Bulkin, *et al.*, Solid State Commun. **59**, 95 (1986).
5. E. Zlokazov and V. V. Chernyshov, J. Appl. Crystallogr. **25,** 447 (1992).
6. V. F. Sears, Neutron News **3**, 26 (1992).
7. K. D. Rouse, M. J. Cooper, E. J. York, *et al.*, Acta Crystallogr. A **26**, 682 (1970).
8. T. M. Sabine, R. B. von Dreele, and J.-E. Jörgensen, Acta Crystallogr. A **44**, 374 (1988).
9. H. Nowotny and G. Heger, Acta Crystallogr. C **39**, 952 (1983).
10. N. Nardelli, J. Appl. Crystallogr. **28**, 659 (1995).

Translated by P. Pozdeev